PARAMETRIC ANALYSIS OF TWO-LAYER SHALLOW FLOW MODELLING FOR LANDSLIDE AND WATER WAVES IN DAM RESERVOIRS

A THESIS SUBMITTED TO
THE GRADUATE SCHOOL OF NATURAL AND APPLIED SCIENCES
OF
MIDDLE EAST TECHNICAL UNIVERSITY

BY

MUSTAFA MERİÇ AKSEN

IN PARTIAL FULFILLMENT OF THE REQUIREMENTS
FOR
THE DEGREE OF MASTER OF SCIENCE
IN
CIVIL ENGINEERING

JANUARY 2022

Approval of the thesis:

PARAMETRIC ANALYSIS OF TWO-LAYER SHALLOW FLOW MODELLING FOR LANDSLIDE AND WATER WAVES IN DAM RESERVOIRS

submitted by **MUSTAFA MERİÇ AKSEN** in partial fulfillment of the requirements for the degree of **Master of Science in Civil Engineering Department, Middle East Technical University** by,

Prof. Dr. Halil Kalıpçılar _______________
Dean, Graduate School of **Natural and Applied Sciences**

Prof. Dr. Erdem Canbay _______________
Head of the Department, **Civil Engineering**

Prof. Dr. İsmail Aydın _______________
Supervisor, **Civil Engineering Department, METU**

Examining Committee Members:

Prof. Dr. Ahmet Cevdet Yalçıner _______________
Civil Engineering Dept., METU

Prof. Dr. İsmail Aydın _______________
Civil Engineering Dept., METU

Prof. Dr. Ender Demirel _______________
Civil Engineering Dept., Eskişehir Osmangazi University

Assoc. Prof. Dr. Onur Pekcan _______________
Civil Engineering Dept., METU

Assoc. Prof. Dr. Ali Ersin Dinçer _______________
Civil Engineering Dept., Abdullah Gül University

Date: ...

I hereby declare that all information in this document has been obtained and presented in accordance with academic rules and ethical conduct. I also declare that, as required by these rules and conduct, I have fully cited and referenced all material and results that are not original to this work.

Name Last name: **Mustafa Meriç AKSEN**

Signature:

ABSTRACT

PARAMETRIC ANALYSIS OF TWO-LAYER SHALLOW FLOW MODELLING FOR LANDSLIDE AND WATER WAVES IN DAM RESERVOIRS

Aksen, Mustafa Meriç

Master of Science, Department of Civil Engineering
Supervisor: Prof. Dr. İsmail Aydın

January 2022, 144 pages

Landslides into dam reservoirs can create large water waves which may cause overtopping of the dam body or even dam breaking in extreme cases. Numerical simulations of water surface deformation in the complete dam reservoir after the impact of sliding mass is necessary to predict potential risks of landslide generated waves. Depth integrated shallow flow equations may be useful to model the generation and propagation of water waves in the reservoir after landslides. Coulomb model for the slide material is combined to 1D shallow flow equations to form a two-layer model for the slide material and water in the reservoir. Finite volume method is used in numerical solution of the model equations. Weighted average flux method is employed to calculate fluxes based on an approximate Riemann solver. First-order well-balanced discretization scheme is implemented as a cure for numerical fluctuations due to rapid bed elevation changes. Several landslide geometries are studied to investigate the energy transfer rate from the sliding material to water in the reservoir and the maximum wave rise in the domain. It is observed that a general formulation between slide characteristics and waves is not feasible due to case dependent relations between the variables.

Keywords: Landslide, Earthquake, Water waves, Shallow flows

ÖZ

BARAJ REZERVUARLARINDA OLUŞAN HEYELAN VE SU DALGALARI İÇİN İKİ KATMANLI SIĞ AKIŞ MODELLEMESİNİN PARAMETRİK ANALİZİ

Aksen, Mustafa Meriç

Yüksek Lisans, İnşaat Mühendisliği
Tez Yöneticisi: Prof. Dr. İsmail Aydın

Ocak 2022, 144 sayfa

Baraj reservuarları içinde oluşan toprak kaymaları, suyun baraj gövdesini aşmasına ve bazı tehlikeli durumlarda barajın yıkılmasına neden olabilecek büyük dalgalanmalar yaratabilir. Kayan kütlenin etkisi ile tüm baraj rezervuarında oluşan su yüzeyi deformasyonunun sayısal simülasyonları, heyelanın sebep olduğu dalgalanmanın olası risklerini tahmin etmek için gereklidir. Sığ su akım denklemleri, dalgaların oluşumu ve yayılmasını modellemek için kullanışlı olabilir. Heyelan için Coulomb modeli, heyelanın ve baraj rezervuarında bulunan su için iki katmanlı matematiksel model oluşturmak üzere 1 boyutlu sığ su akım denklemine birleştirilir. Modelde kullanılan denklemlerin nümerik olarak çözümünde sonlu hacim yöntemi kullanılmıştır. Yaklaşık bir Riemann çözücüsüne dayanan akıların hesaplanması için Ağırlıklı Ortalama Akı (WAF) yöntemi kullanılmıştır. Heyalan kaynaklı hızlı yatak değişiminden dolayı oluşan nümerik dalgalanmaları gidermek için birinci dereceden iyi dengelenmiş ayrıştırma şeması uygulanmıştır. Heyelanın rezervuardaki suya aktardığı enerjinin oranını ve çalışma alanı içerinde gözlemlenen maksimum dalga

yükselişini incelemek için çeşitli heyelan geometrileri çalışılmıştır. Değişkenler arasındaki ilişkilerin durumdan duruma değişmesi sebebiyle, heyelanın karakteristiği ve oluşan dalga arasında kurulacak genel bir formülasyonun mümkün olmayacağı kanısına varılmıştır.

Anahtar Kelimeler: Heyelan, Deprem, Su Dalgaları, Sığ akımlar

To my beloved family

ACKNOWLEDGMENTS

Foremost, I would like to express my greatest appreciation to my supervisor *Prof. Dr İsmail Aydın* for his endless guidance, support and encouragement. I could not have completed this thesis without his patience and help especially during the pandemic. I feel lucky and honored to have a chance to work with him.

This work is funded by Scientific and Technological Research Council of Turkey (TUBİTAK) under grant number 119M595. Therefore, special thanks should be given to Scientific and Technological Research Council of Turkey.

Special thanks should be given to my colleagues and researchers of Hydromechanics Laboratory. Their advice and suggestions have been very helpful in my thesis and career.

I thank with love to the most excellent girlfriend *Özge Bozoğlu*. The burden of this thesis process was lessened significantly by her support. Every time I stumbled, she raised me with love throughout the years I have spent with him. I am truly grateful to her.

I am forever indebted to my father *Sabri Aksen,* and my mother *Tülin Aksen* and my brother *Fırat Aksen* for their unconditional trust and endless support. It was their generously given love and encouragement that made me who I am now. I am honored to dedicate this thesis in their name.

TABLE OF CONTENTS

LIST OF TABLES

TABLES

LIST OF FIGURES

FIGURES

CHAPTER 1

INTRODUCTION

1.1 Landslide Related Risk

Potential hazardous physical phenomena can have detrimental consequences, such as the loss of lives of humans and animals, or destruction of goods and commodities. Generally, natural hazards can be seen in either the geophysical class (Earthquake, Flood etc.) or the biological class (the viral disease etc.)(Burton et al., 1993). For instance, impulsive waves are one of these natural disasters. The formation of the impulsive waves is because of the sudden displacement of the seabed or high force transmission into the water. Here, earthquakes, landslides, volcanic eruptions or ice calves can give rise to the abrupt changes in the seabed (Yavari-Ramshe & Ataie-Ashtiani, 2016).

Figure 1.1, which is published by the NOAA (USA National Geophysical Data Center) and taken from Harbitz et al., 2014, indicates the probabilities of the reasons for several well-known historical tsunamis. More specifically, while the earthquake-generated waves have the dominant occurrence with 81% of the tsunamis, the total occurrence of the tsunamis due to the landslides is about 7%. Moreover, it should be noted that these historical tsunamis may be triggered by the earthquake and the landslide simultaneously with the probability of 5%. Briefly, landslide and earthquake events are responsible for almost 93% of the historical tsunamis; therefore, the behavior of these hazards on the waves are being tried to put greater emphasis.

Furthermore, Harbitz et al., 2014 highlights that whereas the larger reservoirs like the ocean, may be more affected by the earthquake-induced waves, the landslide may form bigger wave run-up height in the relatively shorter reservoir. Therefore, the dam reservoirs could become more vulnerable to the landslide. Besides, more frequent and intense rainfall due to the climate chance could cause more landslides.

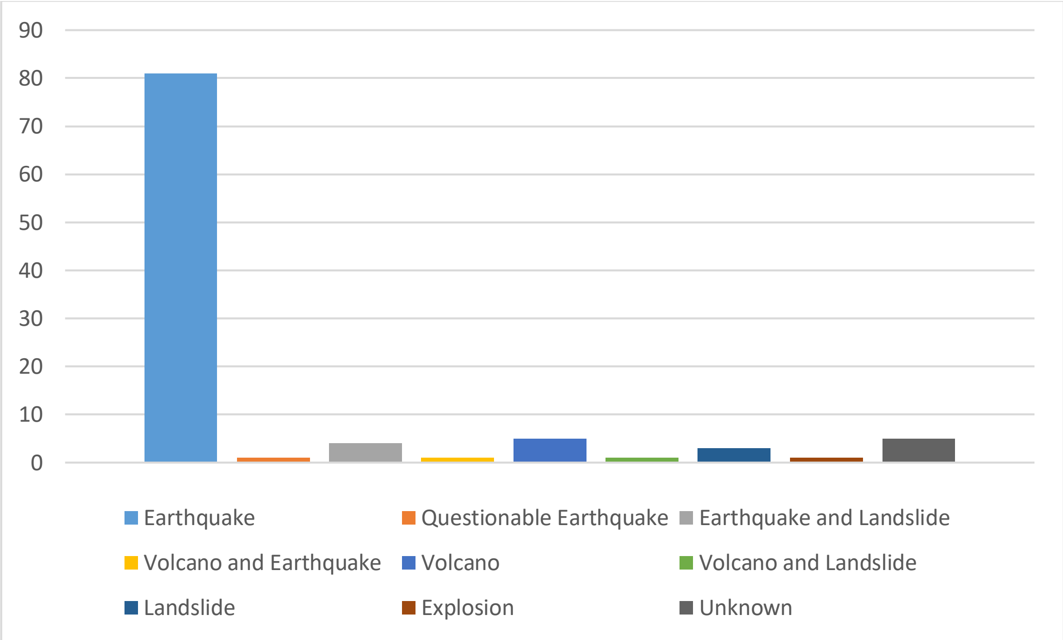

Figure 1.1. Relative Occurrence of Various Historical Tsunami Sources Based on the NOAA/NGDC tsunami database (NGDC 2013)

Considering the enormous volume of water in dam reservoirs, it is important to evaluate the risks arising from unexpected water evacuation. Because the flooding events in the urban areas and even demolishing of the dam may come to the surface. In fact, the evacuation due to the impulsive waves may significantly reduce by lowering the water level in dam reservoirs. However, if the reservoir level was being lowered in the case of hydroelectric power plants, the capacity of electricity productions would dramatically be affected. Therefore, optimization of the dam reservoirs is required by prioritizing the risk analysis of the impulsive waves. The result of landslide-generated waves at Vajont dam reservoir, in Italy in 1963, causing about 2000 people deaths, well-demonstrates the risk potential (Kilburn & Petley, 2003).

In that manner, the explanation of the landslide-generated waves with the mathematical models is essential. Many researchers have been striving to understand the physical behavior of the landslide-generated waves. So far, promising analytical and numerical solutions have been proposed. Substantially, being non-linear behavior of the landslide-generated waves and abundant parameters in the risk analysis have oriented this thesis to consider the numerical solutions as more suitable tools. Recent studies show that the deformable landslide-water wave models are more appropriate and practical to get fast and accurate results.

1.2 Scope of This Study

In the light of observations from the literature, aim of this study is designated as to investigate the capabilities, performance and limitations of a two-layer slide mass-water reservoir modeling based on shallow flow theory through 1D numerical experiments. The SELBIL code developed in Hydraulics Laboratory will be modified to include deformations of the sliding mass as a 1D non-Newtonian shallow flow that attacks hydrostatic water reservoir. The two flow layers, the sliding mass and the water reservoir over the slide will be allowed to interact through the common interface between them. Two parameters, the energy transfer ratio from the sliding mass to the water volume in the reservoir and the maximum water wave height produced in the water reservoir will be investigated as function of all the other slide related parameters.

Organization of this thesis is stated as follows: Chapter 2 explains comprehensive studies related to thesis scope in the literature, Chapter 3 defines the mathematical background of the granular slide material and water flows also it defines the energy transfer ratios, Chapter 4 mainly describes the Finite Volume Method adopted to the one-dimensional shallow water theory with implementation of well-balanced method and in Chapter 5, the results of the one-dimensional numerical model presented by considering several dimensionless parameters for the energy transfer and maximum wave rise graph. Here, several conceptual models are introduced. Finally, the thesis is completed with the important remarks and the recommendations for further studies.

CHAPTER 2

LITERATURE REVIEW

In general, modeling of the landslide is based on the assumption that the landslide material behaves more like a fluid. In the literature, this type of landslides is called fluid-like landslides. The material is assumed to be highly deformable and therefore can reach high velocities. The article by Savage & Hutter (Savage & Hutter, 1989) was a milestone with the newly developed mathematical model for a fluid-like landslide. Basically, the mathematical model utilized modified Shallow Water Equations (SWE) in which the landslide obeys the Coulomb Failure theory as a rheological model. It is supposed that the landslide is a mixture of fluid and solid constituents. In 1991, the same theory (Savage & Hutter, 1991) is applied and improved by simulating the inclined chute flows. In another article by Iverson (Iverson, 1997) the physics of debris flows is explicitly defined for the type of fluid-like landslides. In this work the mathematical model is developed by considering the fluid and solid constituents of the landslide separately but supposed the landslide as a mixture in motion. Later, (Iverson & Denlinger, 2001) Finite Volume Method is applied to these mathematical models. Also, in a companion paper, (Denlinger & Iverson, 2001) the numerical method is verified with the experimental results.

In fact, these mathematical models have constraints when applied on irregular topography. Denlinger & Iverson, 2004 addressed this point by altering the numerical model with the usability of DEM (Digital Elevation Model) and addressed the solutions of this model in its companion paper (Iverson et al., 2004). There have been other promising works such as Iverson & George, 2014 and George & Iverson, 2014. Also, Pudasaini et al. 2003 illustrates how to use the depth averaged granular flow model with gently curved and twisted topography based on the earth-centered coordinates.

Besides, there are several rheological models available in the literature. Specifically, rheological models are used to determine the landslide characteristics. For example, Bingham (Bingham, 1916) and Herschel-Bulkley (Coussot, 1994) can be more appropriate for the mud flow or saturated clay. According to Midi, 2004, dry granular flow can be described with μ(I)-rheology model. Additionally, Voellmy model which stands for the velocity-dependent definitions and Coulomb model can be utilized in case of the granular mixture of the solid and fluid (Yavari-Ramshe & Ataie-Ashtiani, 2016).

Thereafter, Ma et al., 2015 brought a new concept into the literature by integrating the landslide model (Denlinger & Iverson, 2001) with the water body where water is modeled with NHWAVE model (Ma et al., 2012). The non-hydrostatic pressure term for the landslide is introduced, and the interaction between landslide and water body was tackled by arranging the geometrical properties. Nevertheless, it should be noted that the articles by Zhang (Zhang et al., 2021a) and (Zhang et al., 2021b) solved the issues about the irregular bathymetry in the simulation of the landslide-generated waves.

Shallow Water Equations (SWEs) are a set of partial differential equations obtained from the Navier-Stokes's equations by integration over the vertical assuming that the vertical extent is relatively smaller than lateral extent. Although the SWEs are more preferable in respect to advantages of reasonable numerical solution time and easiness to implement, it brings the accuracy of the solution into the discussion, due to neglecting the vertical acceleration of the flows. Full Navier Stokes's equations can be used in small domains for investigation of wave characteristics, such as wave breaking or wave run-up in detail. Therefore, the appropriate mathematical models should be chosen wisely based on aim of the study.

CHAPTER 3

MATHEMATICAL BACKGROUND

Shallow water equations are utilized to simulate the free surface deformations of water and granular flow. Computations of the free surface elevation of water can be easily performed with shallow water equations. However, to simulate the free surface of the granular flow, shallow water equations are required to be modified by implementing the Coulomb model.

Moreover, neglecting the vertical acceleration of these flows is an important simplification and it may make the simulation of the landslide-generated waves restrictive. Because the vertical acceleration becomes dominant while the mass movement occurs at a steep slope. Here, using the concept for the landslide introduced in Iverson et al. 2001 is advantageous in order to enhance the accuracy of the granular flow model. Particularly, when the landslide moves on an inclined ramp, the horizontal acceleration of the granular flow becomes parallel to the local bed coordinate. Therefore, it is advantageous because the bed aligned acceleration on an inclined bed becomes a combination of the vertical and horizontal accelerations with respect to the earth-centered coordinates and it decreases the effects of the assumption that neglects the vertical acceleration of the landslide.

This chapter is organized as follows that: Section 3.1 demonstrates the 2-dimensional shallow water equations for water. Derivation of shallow water equations is provided in Appendix A. In section 3.2, two-dimensional shallow water equations for the granular flow are described. The derivation of the granular flow model is outlined in Appendix B. One-dimensional forms of both water and granular flow are described in Section 3.3. Lastly, the energy transfer ratio is described in Section 3.4.

3.1 2D Shallow Water Equations

The depth integrated continuity equation is:

$$\frac{dh}{dt}+\frac{d(h\,\bar{u})}{dx}+\frac{d(h\,\bar{v})}{dy}=0 \tag{3.1}$$

where, $\bar{u}$ and $\bar{v}$ are the averaged velocity components in x and y directions respectively, h is the depth of the water. Momentum equations in x and y directions are written as:

$$\frac{d}{dt}(h\bar{u}\,)+\frac{d}{dx}\left(h\bar{u}^2+\frac{1}{2}gh^2\,\right)+\frac{d}{dy}(h\bar{u}\bar{v}\,)=-gh\frac{dz_{bed}}{dx}-\frac{1}{\rho}\tau_{zx,z_{bed}}+ha_x \tag{3.2}$$

$$\frac{d}{dt}(h\bar{v}\,)+\frac{d}{dx}(h\bar{u}\bar{v})+\frac{d}{dy}\left(h\bar{v}^2+\frac{1}{2}gh^2\,\right)=-gh\frac{dz_{bed}}{dy}-\frac{1}{\rho}\tau_{zy,z_{bed}}+ha_y \tag{3.3}$$

where g is the gravitational acceleration in negative z direction and z_{bed} is the bottom elevation. $\tau_{zx,z_{bed}}$ and $\tau_{zy,z_{bed}}$ are the bed shear stresses in x and y directions respectively. a_x and a_y are the earthquake accelerations in x and y directions, respectively. Actually, the granular flow has an impact on the shear stresses, but it is generally so small. The manning equation is adopted for the shear stresses between the water and the granular flow at both directions, x and y without considering the granular flow effects.

$$\tau_{zx,z_{bed}}=\rho g n^2\bar{u}h^{-1/3}\sqrt{\bar{u}^2+\bar{v}^2} \tag{3.4}$$

$$\tau_{zy,z_{bed}}=\rho g n^2\bar{v}h^{-1/3}\sqrt{\bar{u}^2+\bar{v}^2} \tag{3.5}$$

where, ρ_g is the density of the granular flow and g_n is the gravity component in n direction which is the normal direction with respect to the slide bottom and n is the Manning coefficient. The coordinates and variables used in the equations are described in Figure 3.1

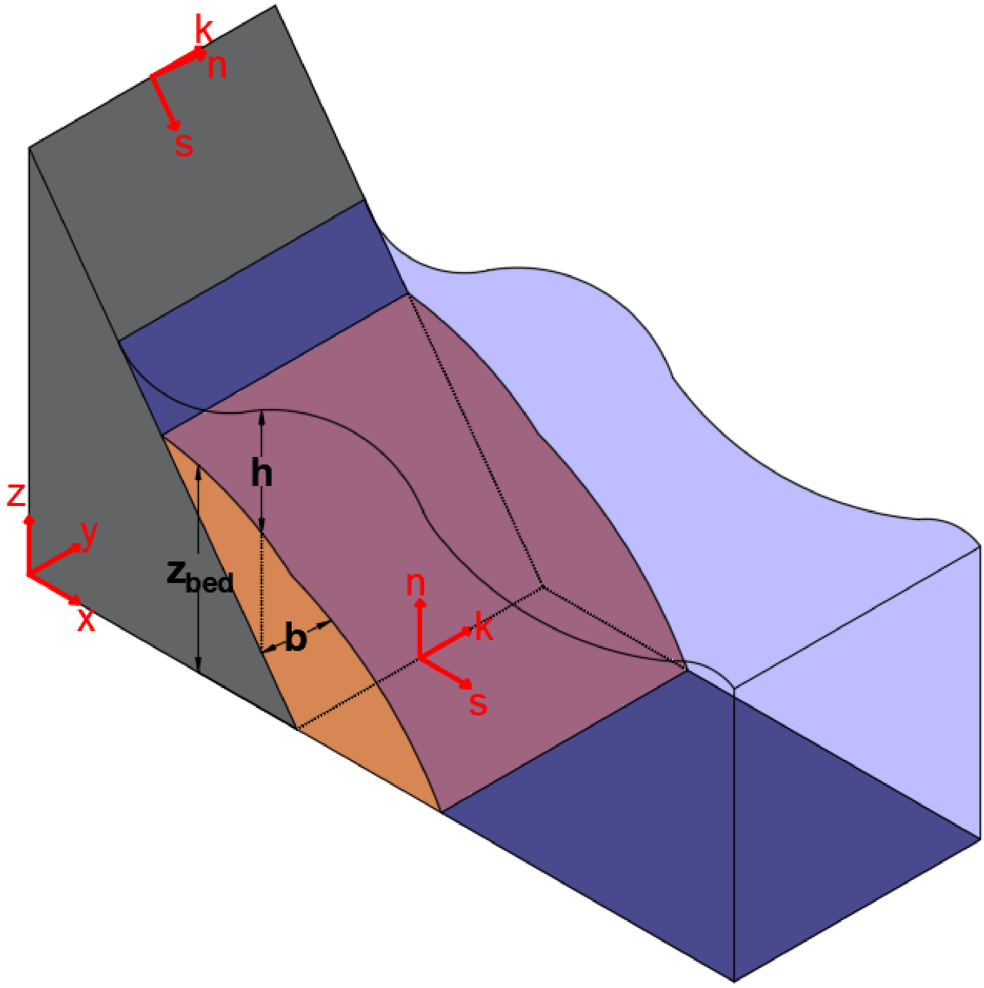

Figure 3.1. Coordinates and geometric description of landslide parameters

3.2 2D Granular Flow Equations

The derivation of the granular flow model is analogous to the derivation of the shallow water equations and it is is provided in Appendix B. The granular flow is supposed to be the grain-fluid mixtures therefore the landslide is fully-saturated.

Continuity equation of the granular flow model can be written as;

$$\frac{db}{dt} + \frac{d\left(b\,\overline{u_g}\right)}{ds} + \frac{d\left(b\,\overline{v_g}\right)}{dk} = 0 \tag{3.6}$$

where, b is the depth of the granular flow. Momentum equations in s and k directions are written as;

$$\frac{d}{dt}\left(b\,\overline{u_g}\,\right)+\frac{d}{ds}\left(b\,\overline{u_g}^2\,\right)+\frac{d}{dk}\left(b\,\overline{u_g}\,\overline{v_g}\right)=\left(g_s+a_s\right)b+\frac{1}{\rho_g}T_{solid,s}+\frac{1}{\rho_g}T_{fluid,s} \quad (3.7)$$

$$\frac{d}{dt}\left(b\,\overline{v_g}\,\right)+\frac{d}{ds}\left(b\,\overline{u_g}\,\overline{v_g}\right)+\frac{d}{dk}\left(b\,\overline{v_g}^2\right)=\left(g_k+a_k\right)b+\frac{1}{\rho_g}T_{solid,k}+\frac{1}{\rho_g}T_{fluid,k} \quad (3.8)$$

where, g_s and g_k are the gravity acceleration components of the s and k directions respectively. $T_{solid,s}$ and $T_{fluid,s}$ are the solid stresses and fluid stresses that are applied in the s direction respectively. They are defined as follows;

$$T_{solid,s}=-\frac{d\left(\frac{1}{2}k_{act/pass}\rho_g g_n b^2(1-\psi)\right)}{ds}-\frac{d}{dk}\left(b\,\overline{\tau_{ks}^{solid}}\right)-\left(\tau_{ns,f}^{solid}-\tau_{ns,0}^{solid}\right) \quad (3.9)$$

When the free surface of the granular flow is exposed to hydrostatic pressure of the water, $T_{fluid,s}$ becomes;

$$T_{fluid,s}=-\frac{d\left(\frac{1}{2}\psi\rho_g g_n b^2\right)}{ds}-\rho g b\frac{d(h)}{ds} \quad (3.10)$$

When the free surface of the granular flow is exposed to atmosphere, $T_{fluid,s}$ becomes;

$$T_{fluid,s}=-\frac{d\left(\frac{1}{2}\psi\rho_g g_n b^2\right)}{ds} \quad (3.11)$$

$T_{solid,k}$ and $T_{fluid,k}$ are the solid stresses and fluid stresses that are applied in the k direction respectively. They are defined as follows;

$$T_{solid,k}=-\frac{d}{ds}\left(b\,\overline{\tau_{sk}^{solid}}\right)-\frac{d\left(\frac{1}{2}k_{act/pass}\rho_g g_n b^2(1-\psi)\right)}{dk}-\left(\tau_{nk,f}^{solid}-\tau_{nk,0}^{solid}\right) \quad (3.12)$$

When the free surface of the granular flow is exposed to hydrostatic pressure of the water, $T_{fluid,k}$ becomes;

$$T_{fluid,k} = -\frac{d\left(\frac{1}{2}\psi\rho_g g_n b^2\right)}{dk} - \rho g b\frac{dh}{dk} \tag{3.13}$$

When the free surface of the granular flow is exposed to atmosphere, $T_{fluid,k}$ becomes;

$$T_{fluid,k} = -\frac{d\left(\frac{1}{2}\psi\rho_g g_n b^2\right)}{dk} \tag{3.14}$$

ψ is the parameter to define the effects of the solid constituent on the hydrostatic pressure inside the water. $\overline{\tau_{ks}^{solid}}$ and $\overline{\tau_{sk}^{solid}}$ are the averaged shear stresses between the s and k directions. They can be defined by;

$$\overline{\tau_{sk}^{solid}} = \overline{\tau_{ks}^{solid}} = -sign(S_{sk})\left(\frac{1}{2}k_{act/pass}(1-\psi)\rho_g g_n b\right)\sin\emptyset \tag{3.15}$$

S_{sk} refers to the rate of strain in s-k plane. $\tau_{ns,f}^{solid}$ and $\tau_{nk,f}^{solid}$ are the shear stresses between the water and the granular flow. It is not considered in the landslide because it is negligibly small.

$\tau_{ns,0}^{solid}$ and $\tau_{nk,0}^{solid}$ are the basal shear stresses in the s and k directions respectively. The Coulomb term is applied as a rheological model.

$$\tau_{ns,0}^{solid} = -sign(u_g)\left(\rho_g g_n b(1-\psi)\left(1+\frac{{u_g}^2}{r_s g_n}\right)\right)\tan\phi_{bed} \tag{3.16}$$

$$\tau_{nk,0}^{solid} = -sign(v_g)\left(\rho_g g_n b(1-\psi)\left(1+\frac{{v_g}^2}{r_k g_n}\right)\right)\tan\phi_{bed} \tag{3.17}$$

where;

r_s is the curvature of the bottom surface in the s direction,

r_k is the curvature of the bottom surface in the k direction.

$k_{act/pass}$ is the coefficient of the lateral earth pressure. It is basically proportion of the averaged bed-lateral solid stress and the averaged bed-normal solid stress.

If $\frac{du_g}{ds} + \frac{dv_g}{dk} > 0$ (Active motion state),

$$k_{act/pass} = 2\frac{1 - \sqrt{[1 - \cos^2\phi\,(1 + \tan^2\phi_{bed})]}}{\cos^2\phi} - 1 \tag{3.18}$$

If $\frac{du_g}{ds} + \frac{dv_g}{dk} < 0$ (Passive motion state),

$$k_{act/pass} = 2\frac{1 + \sqrt{[1 - \cos^2\phi\,(1 + \tan^2\phi_{bed})]}}{\cos^2\phi} - 1 \tag{3.19}$$

When the internal friction angle of the bottom surface is equal or greater than the internal friction angle of the granular material, the coefficient of the lateral earth pressure can be written as follows;

$$k_{act/pass} = \frac{1 + \sin^2\phi}{1 - \sin^2\phi} \tag{3.20}$$

ϕ is the internal friction angle of the granular flow, ϕ_{bed} is the internal friction angle of the bottom surface of the granular flow. Effects of parameters in the coefficient of the lateral pressure is illustrated in Figure 3.2.

Horizontal and vertical axes show the internal friction angle of the bottom surface of the granular flow and the coefficient of the lateral earth pressure respectively. $20^\circ, 30^\circ$ and 40° stand for the investigation of the internal friction angle of the granular flow. Passive motion states are remarked by dashed-dot line. Solid line indicates the active motion states of the granular flow. When the internal friction angle of the bottom surface is increased, the coefficient of the lateral earth pressure decreases in the passive motion state, whereas, the coefficient of the lateral earth pressure increases in the active motion state of the granular flow.

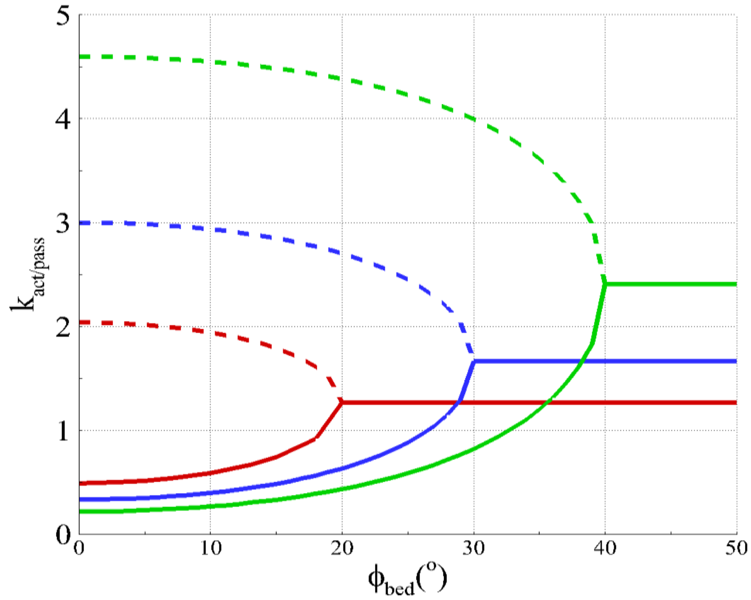

Figure 3.2. Motion states of the Granular Flow

Besides, with constant internal friction angle of the bottom surface of the granular flow, the coefficient of the lateral earth pressure at the passive motion state is higher than the coefficient of the lateral earth pressure at the active motion state. Another consideration is about the internal friction angle of the granular flow. Internal friction angle of the granular flow is briefly the angle between horizontal axis and soil line angle when soil is accumulated on the straight bed. When the internal friction angle of the granular flow increases, the coefficient of the lateral earth pressure increases in both motion states. Changing in the coefficient of the lateral earth pressure has an influence on the motion of the granular flow. When the coefficient of the lateral earth pressure is increased, in case of the constant average bed-normal solid stress, average bed-lateral solid stress increases.

This leads to more resistance in the lateral direction and consequently, more accumulation. In addition, when internal bed friction angle is more than internal friction angle, it violates the Mohr-Coulomb Failure line.

3.3 1D Models

Two-dimensional models for shallow water equations and the granular flow model were introduced in section 3.1 and 3.2 respectively. However, only one-dimensional systems will be studied in this thesis. From now on, averaged granular flow velocities in s and k directions are defined as u_g and v_g. Additionally, the averaged water velocities in x and y directions are defined as u and v respectively. Because the equations only use the averaged form. The vector forms of these equations are demonstrated in the next section.

3.3.1 The Set of Equations for Water

Continuity and momentum equations can be demonstrated in the vector form.

$$U_t + F(U)_x = S(U) \tag{3.21}$$

U refers to the vector of conserved variables, F(U) defines the flux vector in the x direction. $S(U)$ is the source term of the governing equations.

$$U = \begin{bmatrix} h \\ hu \end{bmatrix} \tag{3.22}$$

$$F(U) = \begin{bmatrix} hu \\ hu^2 + \frac{1}{2}gh^2 \end{bmatrix} \tag{3.23}$$

$$S(U) = \begin{bmatrix} 0 \\ -gh\frac{dz_{bed}}{dx} + ha_x - gn^2\bar{u}h^{-1/3}\sqrt{\bar{u}^2 + \bar{v}^2} \end{bmatrix} \tag{3.24}$$

When the earthquake triggered landslide and waves are the subject, the earthquake effects on the water can be implemented into this mathematical model. The earthquake is defined as sinusoidal wave formulating $a_x = a_{max,x} \sin\left(\frac{2\pi}{T}t\right)$ where T is the wave period and $a_{max,x}$ is the amplitude of earthquake.

3.3.2 The Set of Equations for Granular Flow

Continuity and momentum equations can be transformed into the vector form.

$$V_t + H(U)_s = S_1(V) + S_2(V) \tag{3.25}$$

V refers to the vector of conserved variables, H(V) defines the flux vector in the s direction. $S_1(V)$ and $S_2(V)$ are the source terms of the governing equations. $S_2(V)$ is the source term that indicates the interaction between water and granular flow. $S_1(V)$ stands for the effects of gravity and the basal shear stress.

$$V = \begin{bmatrix} b \\ bu_g \end{bmatrix} \tag{3.26}$$

$$H(V) = \begin{bmatrix} bu_g \\ bu_g{}^2 + \frac{1}{2} g_n b^2 \left(\psi + k_{act/pass}(1-\psi)\right) \end{bmatrix} \tag{3.27}$$

$$S_1(V) = \begin{bmatrix} 0 \\ (g_s + a_s)b - \frac{u_g}{\sqrt{u_g{}^2}} \left(g_n b(1-\psi)\left(1 + \frac{u_g{}^2}{r_s g_n}\right)\right) \tan \phi_{bed} \end{bmatrix} \tag{3.28}$$

$$S_2(V) = \begin{bmatrix} 0 \\ -\frac{\rho}{\rho_g} g b \frac{d(h)}{ds} \end{bmatrix} \tag{3.29}$$

When the free surface of the granular flow is exposed to the atmosphere, $S_2(V)$ vanishes. The earthquake acceleration is defined as $a_s = a_{max,s} \sin\left(\frac{2\pi}{T} t\right)$.

3.4 Energy Transfer Ratios

Mathematical formulation for landslide-generated wave motion was given in Section 3.3 for the one-dimensional systems. Stages of these hazards are sortable as follows: splash zone, near and far fields of the wave propagation, then overtopping the dam

(Yavari-Ramshe & Ataie-Ashtiani, 2016). The splash zone implies the area that the landslide hits the water and this area creates a complex flow. The article (Yavari-Ramshe & Ataie-Ashtiani, 2016) conveys the near-field as that “Within the near-field area, the displaced water forms a well-defined wave due to the transferred energy from the landslide to the water”. After the well-defined waves are formed, these waves propagate toward the dam and this area is called the far-field. Eventually, the waves are ended up either overtopped the dam or reflecting back to the dam reservoirs depending on the dam height. Substantially, this paper analyzes the wave generation and propagation; therefore, it focuses on near-field and far-field characteristics with various variables. To be able to comment on them, two dimensionless quantities are proposed, kinetic energy transfer ratio (KETR) and potential energy transfer ratio (PETR).

Landslide energy transfer to the wave kinetic energy:

$$KETR = \frac{\begin{array}{c} Wave\ Kinetic\ Energy\ with\ respect\ to\ time \\ in\ Near-Field\ and\ in\ Far-Field \end{array}}{Maximum\ Kinetic\ Energy\ of\ Landslide} = \frac{KE_w(t)}{\max(KE_l)} \quad (3.30)$$

Landslide energy transfer to the wave potential energy:

$$PETR = \frac{\begin{array}{c} Wave\ Potential\ Energy\ with\ respect\ to\ time \\ in\ Near-Field\ and\ in\ Far-Field \end{array}}{Maximum\ Kinetic\ Energy\ of\ Landslide} = \frac{PE_w(t)}{\max(KE_l)} \quad (3.31)$$

3.4.1 Maximum Kinetic Energy of the Landslide

Initial potential energy of the landslide or maximum kinetic energy of the landslide can be considered to express the physical characteristics of the landslides. The initial potential energy of the landslide is an inappropriate parameter when the submarine or partially subaerial landslides are the subject. The maximum kinetic energy of the landslide can be applied to every scenario. However, it is not appropriate for the one-layer landslide models.

Moreover, when and where the maximum kinetic energy of landslide occurs is ambiguous. Because this parameter only points out the maximum energy transferred into the water, not the slide impact energy. The paper (Fritz et al., 2004) proposed similar dimensionless parameters that indicate the kinetic energy of the slide impact as a parameter.

The kinetic energy of the landslide can be calculated as follows;

$$KE_l = \sum_{i=1}^{M} \frac{1}{2} \frac{W_{g,e}^i}{g} \left(u_g^i\right)^2 \tag{3.32}$$

M is the number of computational mesh in the reservoir. $W_{g,e}^i$ is the effective weight of the landslide at the i-th cell. The reason to use the effective weight of the landslide is that the landslide can be located inside the water.

When the granular flow surface is exposed to atmosphere, the effective weight of the granular flow for the i^{th} cell can be written as follows;

$$W_{g,e}^i = \rho_g \left(\Delta x\, b_{v,i}\right) g \tag{3.33}$$

where, $b_{v,i}$ is the vertical depth of the granular flow. When the surface of the granular flow is exposed to the water, the effective weight of the granular flow for the i-th cell is given as.

$$W_{g,e}^i = \left(\rho_g - \rho\right)\left(\Delta x\, b_{v,i}\right) g \tag{3.34}$$

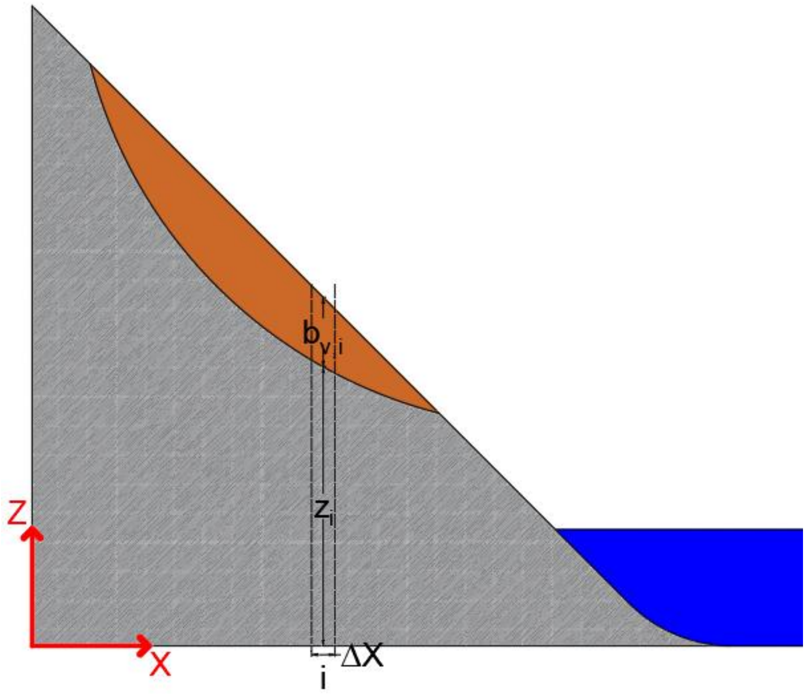

Figure 3.3. Initial position of the landslide-generated waves

3.4.2 Wave Energy of Water in the Reservoir

In literature, there are various definitions of area of splash zone, but determining the splash zone is still an arguable phenomenon. Alternate estimates of the starting points of near-field and far-field areas are possible. It is simplified by considering that these zones are supposed to commence where the landslide front appears.

Starting point of the landslide head is marked as i* in Figure 3.4 and the kinetic and potential energy of the water in the reservoir is computed for that instant of time:

$$KE_w(t) = \sum_{i=1}^{M} \frac{1}{2} \frac{W_e^i}{g} (u_i)^2 \tag{3.35}$$

where, W_e^i is the effective weight of the water at the i-th cell.

$$W_e^i = \rho(h_i \Delta x) g \tag{3.36}$$

Also, the potential wave energy of the water is defined as:

$$PE_w(t) = \sum_{i=1}^{M} \frac{1}{2} \rho g \left(z_{bed,i} + h_i - h_0\right)^2 \Delta x \tag{3.37}$$

where h_0 refers to the initial water level in the reservoir.

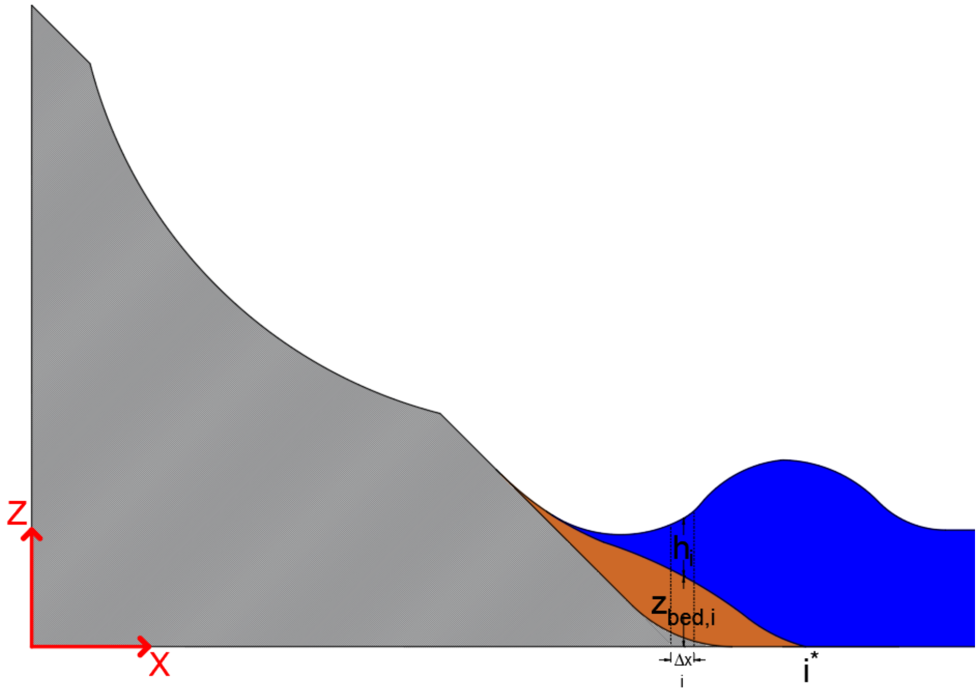

Figure 3.4. Snapshot of the landslide-generated waves at time t

Furthermore, it must be noted that the kinetic and potential energy transfer ratios are not appropriate for the one-layer landslide models. One-layer landslide model means that the landslide material is also water and it mixes with the water when the landslide hits the water. It creates a problem about finding the maximum kinetic energy of the landslide. Therefore, another parameter is applied by considering the initial potential energy of the landslide.

$$ETR = \frac{\begin{array}{c} Wave\ Kinetic\ Energy\ with\ respect\ to\ time \\ in\ Near-Field\ and\ in\ Far-Field \end{array}}{Intial\ Potential\ Energy\ of\ the\ Landslide} = \frac{KE_w(t)}{PE_l(t=0)} \tag{3.38}$$

$KE_w(t)$ is already defined in equation 3.35. Initial potential energy of the landslide is defined as;

$$PE_l(t=0) = \sum_{i=1}^{M} \rho b_{v,i} \Delta x g \left(z_i + \frac{b_{v,i}}{2} - h_0 \right) \tag{3.39}$$

In this equation the density of the landslide is the density of water. Because in the one-layer landslide-generated waves, the landslide is defined by the water volumes.

CHAPTER 4

NUMERICAL SOLUTION METHODS

The depth integrated form of water and granular flows were described in equations 3.21~3.29. Different coordinates are used for water (x-y) and granular slide material (s-n). Besides, the stress definitions are slightly different for each medium. However, both set of SWEs can numerically be solved using the same scheme. Therefore, the numerical solution procedures described in this chapter will be used for both SWE systems.

4.1 Finite Volume Method

Finite Volume Method (FVM) is a discretization technique of the partial differential equations by integrating the conservation equations of the fluid flow. The discretization of the equations uses computational nodes at the centroid of the finite volumes of non-overlapping cells which are called the control volume. The FVM is preferred due to its acquisition of being more conservative for the fluid flow, especially considering the multiphase flows such as the landslide-generated waves.

System of one-dimensional conservation laws (3.21), neglecting the source terms can be written as

$$\frac{d}{dt}u + \frac{d}{dx}f(u) = 0 \tag{4.1}$$

Integrating over cell i, with $\Delta x = \left[x_{i-1/2}, x_{i+1/2}\right]$ and $\Delta t = [t^n, t^{n+1}]$, we get

$$U_i^{n+1} = U_i^n - \frac{\Delta t}{\Delta x}\left[F_{i+1/2} - F_{i-1/2}\right] \tag{4.2}$$

where, U_i^{n+1} and U_i^n are the cell averaged values of the conserved variables of u_i over Δx.

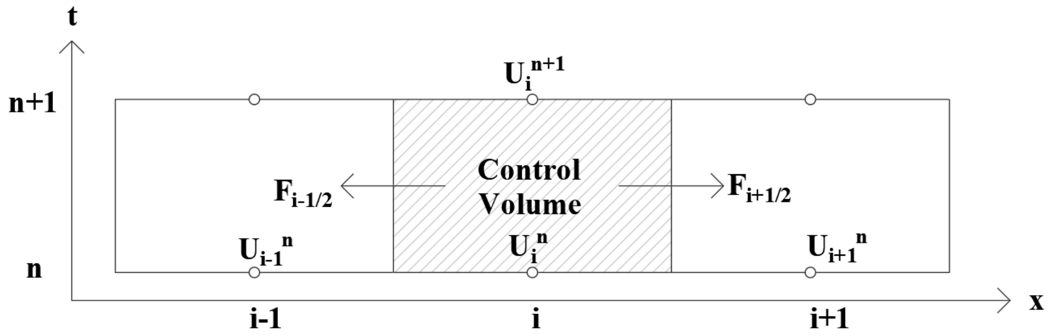

Figure 4.1: Discretization of i[th] cell

It is assumed that U_i are piecewise constant distribution of data in each cell over Δx.

$$U_i = \frac{1}{\Delta x_i} \int_{x_{i-1/2}}^{x_{i+1/2}} u_i dx \tag{4.3}$$

Additionally, $F_{i\pm1/2}$ represents the time average interface fluxes of $f_{i\pm1/2}$ over Δt.

$$F_{i\pm1/2} = \frac{1}{\Delta t} \int_{t^n}^{t^{n+1}} f_{i\pm1/2} \, dt \tag{4.4}$$

The cell averaged values of conserved variables of u_i and the time average interface fluxes $f_{i\pm1/2}$ are illustrated in Figure 4.1.

4.2 Riemann Problem and Godunov's Method

Riemann problem is set to specify the Equation 4.2 with the initial conditions as stated in equation 4.5. The Riemann problem is a type of initial condition problem that consists of a conserved equation and piecewise constant initial data which has a single discontinuity in the domain of interest. Mainly, it defines the problem locally to solve the interface fluxes of the cells.

$$U_t + F_x(U) = 0$$
$$U(x,0) = \begin{cases} U_L & if\ x < 0 \\ U_R & if\ x > 0 \end{cases} \tag{4.5}$$

Here, when referencing the interface surface location as x = 0, the constant cell-averaged data on the left and right sides of the interface surface, U_L (U_i^n) and U_R (U_{i+1}^n) in case of $F_{i+1/2}$ respectively, represent the conditions at time t = 0 s.

The solution of the Riemann problem is tackled by Godunov-type methods. In detail, Godunov's Method is the first-order shock-capturing upwind method that uses the exact or approximate Riemann solvers locally. In fact, Godunov's type method can also be extended into higher order of accuracy in both time and space. More specifically, Weighted Averaged Flux (WAF) and MUSCL-Hancock schemes can be listed as the second order of accuracy extension of the Godunov's method in both time and space.

Besides, left and right initial conditions may be associated by either shock waves or rarefaction waves (Toro 2001). In detail, the shock wave refers to an abrupt transition in the fluid properties, especially transition in wave velocity and a rarefaction wave is relatively a smooth transition in the fluid features. The solution of Riemann problem can be structured based on the combination of wave formations of left and right sides of the interface surface.

4.3 The Riemann Solvers

Exact or approximate Riemann solvers can be used to compute the numerical scheme derived by Godunov's methods. Decision of which solver is more suitable can be made by their own characteristics. Particularly, acquisition of exact Riemann solvers is to compute more accurate results, but they are not easy to implement. On the other hand, approximate Riemann solvers are more straightforward to implement and bring less computational cost. In this thesis, the HLL Riemann solver is preferred.

4.3.1 The HLL Approximate Riemann Solver

HLL Riemann solver is suitable for one-dimensional systems. In case of two-dimensional systems, HLL can be modified into HLLC Riemann solver form. However, scope of this thesis covers only the one-dimensional systems. The detailed explanation of the HLLC method can be found in Toro, 2001.

In HLL Riemann solver, left and right wave speeds, S_L and S_R, are assumed from the solution of Riemann problem with data at U_L and U_R and corresponding interface fluxes $F_L(U_L)$ and $F_R(U_R)$ respectively.

The interface flux at $i + 1/2$ can be estimated as follows;

$$F_{i+\frac{1}{2}} = \begin{cases} F_L & if\ S_L > 0 \\ F_{HLL} = \dfrac{S_R F_L - S_L F_R + S_R S_L (U_R - U_L)}{S_R - S_L} & if\ S_L \le 0 \le S_R \\ F_R & if\ S_R < 0 \end{cases} \tag{4.6}$$

Main consideration, here, is the estimation of the wave speeds. This can be achieved by checking the wetness of left and right beds. More specifically, there are 3 combinations.

i) When both left and right bed are wet, the wave speeds can be estimated as follows;

$$\begin{cases} S_L = u_L - c_L & if\ h^* \le h_L \\ S_L = u_L - c_L \sqrt{\dfrac{1}{2}\left(\dfrac{h^*(h^* + h_L)}{h_L^2}\right)} & if\ h^* > h_L \end{cases} \tag{4.7}$$

The conditions for the left wave speed assume the wave as whether they are rarefaction waves or shock waves. If $h^* \leq h_L$, it means that the left wave is a rarefaction.

$$\begin{cases} S_R = u_R + c_R & if\ h^* \leq h_R \\ S_R = u_R + c_R\sqrt{\dfrac{1}{2}\left(\dfrac{h^*(h^*+h_R)}{h_R^2}\right)} & if\ h^* > h_R \end{cases} \tag{4.8}$$

Same conditions are valid for the right wave speed. Here, $if\ h^* > h_R$, the right wave is a shock wave. Here, whether wave is the rarefaction wave or shock wave is determined with a value of depth at star region, h^*. Toro, 2001 recommends the following formula;

$$h^* = \frac{1}{g}\left[\frac{1}{2}(c_L + c_R) + \frac{1}{4}(u_L - u_R)\right]^2 \tag{4.9}$$

ii) When the left bed is dry and the right bed is wet, the wave speeds are written as;

$$\begin{cases} S_L = u_R - c_R \\ S_R = u_R + 2c_R \end{cases} \tag{4.10}$$

iii) When the left bed is wet and the right bed is dry, the wave speeds are;

$$\begin{cases} S_L = u_L - c_L \\ S_R = u_L + 2c_L \end{cases} \tag{4.11}$$

Between Equations 4.7 and 4.11, u_L and h_L are the velocity and depth of the left cell, u_R and h_R are the velocity and depth of the right cell, and also c_L and c_R are the wave celerity for the left and right cells respectively, and formulated as follows;

$$c_L = \sqrt{gh_L} \tag{4.12}$$

$$c_R = \sqrt{gh_R} \tag{4.13}$$

4.4 Weighted Average Flux (WAF) Scheme

As aforementioned in section 4.2, although Godunov's scheme is the first-order upwind method, the order of the method can be upgraded into second-order upwind method in both time and space for the accuracy purposes. For that purpose, WAF or MUSCL methods can be integrated for the solution of Riemann problem. In this thesis, WAF method is utilized to improve the accuracy of the Godunov's scheme to second order. However, one drawback of the WAF method is the oscillatory features. It is unpractical due to the numerical oscillations. Therefore, the WAF method is adjusted with total variation diminishing (TVD) version to get rid of the oscillations in the computed values. In the WAF method, the interface fluxes are formulated as;

$$F_{i+\frac{1}{2}}^{waf} = \frac{1}{t_2 - t_1} \frac{1}{x_2 - x_1} \int_{t_1}^{t_2} \int_{x_1}^{x_2} F\big(U(x,t)\big) dx\, dt \tag{4.14}$$

where t_1 and t_2 are time range of integration and x_1 and x_2 are the location of left and right cells of the interface.

The solution of the integral of the WAF version of the interface flux in equation 4.14 is tackled by computing the mid-point values:

$$F_{i+\frac{1}{2}}^{waf} = \frac{1}{\Delta x} \int_{-\Delta x/2}^{\Delta x/2} F\left(U_{i+1/2}\left(x, \Delta t/2\right)\right) dx \tag{4.15}$$

Then, the integral in Equation 4.15 can be evaluated by the sum of the weighted averaged variables;

$$F_{i+\frac{1}{2}}^{waf} = \sum_{m=1}^{N+1} w_m\, F_{i+1/2}^{m} \tag{4.16}$$

where; w_m is the weighted averaged of the flux, $F^m_{i+1/2}$ is the flux value in the interval and N is the number of the waves in the Riemann solution. Here, w_m can be formulated as;

$$w_m = \frac{1}{2}(c_m - c_{m-1}) \tag{4.17}$$

c_m indicates Courant number for mth wave and it is given by

$$c_m = \frac{\Delta t}{\Delta x} S_m \tag{4.18}$$

Conditions for the Courant number of 0th and N+1th are; $c_0 = -1$ and $c_{N+1} = 1$. Then, inserting the Equation 4.17 and the initial conditions for the Courant number, Equation 4.16 becomes;

$$F^{waf}_{i+\frac{1}{2}} = \frac{1}{2}(F_i + F_{i-1}) - \frac{1}{2}\sum_{m=1}^{N} c_m \, \Delta F^m_{i+1/2} \tag{4.19}$$

where;

$$\Delta F^m_{i+1/2} = F^{m+1}_{i+1/2} - F^m_{i+1/2} \tag{4.20}$$

4.4.1 Total Variation Diminishing (TVD) Modification of the WAF Method

Applying the higher-order methods are responsible not only to an increase in the accuracy but also increased oscillations of the computed values. To make the higher-order methods oscillation free, Total Variation Diminishing (TVD) modification is required. TVD modification of the WAF method of the interface flux is given as Toro, 2001.

$$F^{tvd-waf}_{i+\frac{1}{2}} = \frac{1}{2}(F_i + F_{i-1}) - \frac{1}{2}\sum_{m=1}^{N} sign(c_m)\, A_m \Delta F^m_{i+1/2} \tag{4.21}$$

where, c_m is the Courant number and A_m is the WAF limiter function.

$$A_m = 1 - (1 - |c_m|)\varphi(r) \tag{4.22}$$

Here, r is the ratio of the upwind-side gradient to the downward-side gradient.

$$r = \begin{cases} \dfrac{q_i^m - q_{i-1}^m}{q_{i+1}^m - q_i^m} & if \;\; c_m > 0 \\ \dfrac{q_{i+2}^m - q_{i+1}^m}{q_{i+1}^m - q_i^m} & if \;\; c_m > 0 \end{cases} \tag{4.23}$$

$\varphi(r)$ is a limiter function and can be defined by several methods, such as super-bee, van Leer's limiter, van Albada's limiter and min-bee.

$$\varphi_{superbee}(r) = max[0, \min(1,2r), \min(2,r)] \tag{4.24}$$

$$\varphi_{Van\ Leer}(r) = \frac{r + |r|}{1 + r} \tag{4.25}$$

$$\varphi_{Van\ Albada}(r) = \frac{r + r^2}{1 + r^2} \tag{4.26}$$

$$\varphi_{Min-Mod}(r) = \min(1, r) \tag{4.27}$$

4.5 Well-Balanced Hydrostatic Reconstruction for the Water

When two conditions; zero velocity of the water and hydrostatic water level observed, the momentum equation of water (Eqn. 3.21) reduces to;

$$u = 0 \tag{4.28}$$

$$h + z_{bed} = constant \tag{4.29}$$

$$\left(\frac{1}{2}gh^2\right)_x = -gh\frac{dz_{bed}}{dx} \tag{4.30}$$

Equation 4.30 should be in a balance to avoid numerical oscillations. To achieve this property, several well-balanced approaches are introduced. Among them, first-order hydrostatic reconstruction scheme which is proposed by (Audusse et al., 2004) is adopted here. The second order version is available in the article (Audusse et al., 2004). Although the second order version promises more accurate results, it requires more complex works. Additionally, the second order version of this method is vulnerable when the transition from wet to dry mesh is occurred. Therefore, the first order method seems enough to implement.

4.5.1 Discretization of Source Term

Semi discrete finite volume form of the discretized equations can be written as

$$\Delta x_i \frac{d}{dt} U_i(t) + \left(F_{i+\frac{1}{2}} - F_{i-\frac{1}{2}}\right) = S_i \tag{4.31}$$

$F_{i+\frac{1}{2}}$ are the flux functions calculated from solving the Riemann problem according to the Riemann states at left and right of the cell interfaces as

$$\begin{aligned} F_{i+\frac{1}{2}} &= F\left(U_{i+\frac{1}{2}}{}^{l}, U_{i+\frac{1}{2}}{}^{r}\right) \\ F_{i-\frac{1}{2}} &= F\left(U_{i-\frac{1}{2}}{}^{l}, U_{i-\frac{1}{2}}{}^{r}\right) \end{aligned} \tag{4.32}$$

According to the paper (Audusse et al., 2004), to ensure that the balance is satisfied between the hydrostatic pressure term and the bed slope source term for the numerical scheme, Equation 4.30 should be satisfied. Therefore, if the hydrostatic momentum flux $\left(\frac{1}{2}gh^2\right)_x$ is replaced with the bed slope term in the Equation 3.21 and still the discretization of the numerical scheme preserves its balance, then it is validated that the Equation 4.30 is satisfied.

$$S_i = ghz_x = \left(\frac{1}{2}gh^2\right)_x \tag{4.33}$$

By integrating of equation 4.33 over cell i from $x_{i+\frac{1}{2}^l}$ to $x_{i-\frac{1}{2}^r}$, the cell-averaged source term S_i can be obtained as follows

$$S_i = -\int_{x_{i-\frac{1}{2}^r}}^{x_{i+\frac{1}{2}^l}} ghz_x\,dx = \int_{x_{i-\frac{1}{2}^r}}^{x_{i+\frac{1}{2}^l}} \frac{d}{dx}\left(\frac{1}{2}gh^2\right)\,dx \tag{4.34}$$

Then, the cell-averaged source term becomes;

$$S_i = \frac{g}{2}\left(h^2_{i+\frac{1}{2}^l} + h^2_{i-\frac{1}{2}^r}\right) \tag{4.35}$$

Besides, (Audusse et al., 2004) introduced the following reconstructed values for h and z_{bed} at the cell interfaces and it is stated with the star symbol.

$$z^*_{bed,i+1/2} = \max\left(z^r_{bed,i}, z^l_{bed,i+1}\right) \tag{4.36}$$

$$h^*_{i+\frac{1}{2}^-} = \max\left(0, z^r_{bed,i} + h^r_i - z^*_{bed,i+1/2}\right) \tag{4.37}$$

$$h^*_{i+\frac{1}{2}^+} = \max\left(0, z^l_{bed,i+1} + h^l_{i+1} - z^*_{bed,i+1/2}\right) \tag{4.38}$$

Where $z_{i,r}$ and $z_{bed,i+1,l}$ are the bed elevation at the right of the cell i and the left of the cell i+1, respectively. $h_{i,r}$ and $h_{i+1,l}$ are defined in the same manner.

4.5.2 First Order Well-Balanced Scheme Based on Hydrostatic Reconstruction

The reconstructed variables for the first-order well-balanced method are illustrated in Figure 4.2.

So far, the general discretization of the reconstructed values is defined in Eqns.4.36~4.38. For the first order well-balanced scheme, the reconstructed values can be written as;

$$z^*_{bed,i+1/2} = \max\left(z_{bed,i}, z_{bed,i+1}\right) \tag{4.39}$$

$$h^*_{i+\frac{1}{2}^-} = \max\left(0, z_{bed,i} + h_i - z^*_{bed,i+1/2}\right) \tag{4.40}$$

$$h^*_{i+\frac{1}{2}^+} = \max\left(0, z_{bed,i+1} + h_{i+1} - z^*_{bed,i+1/2}\right) \tag{4.41}$$

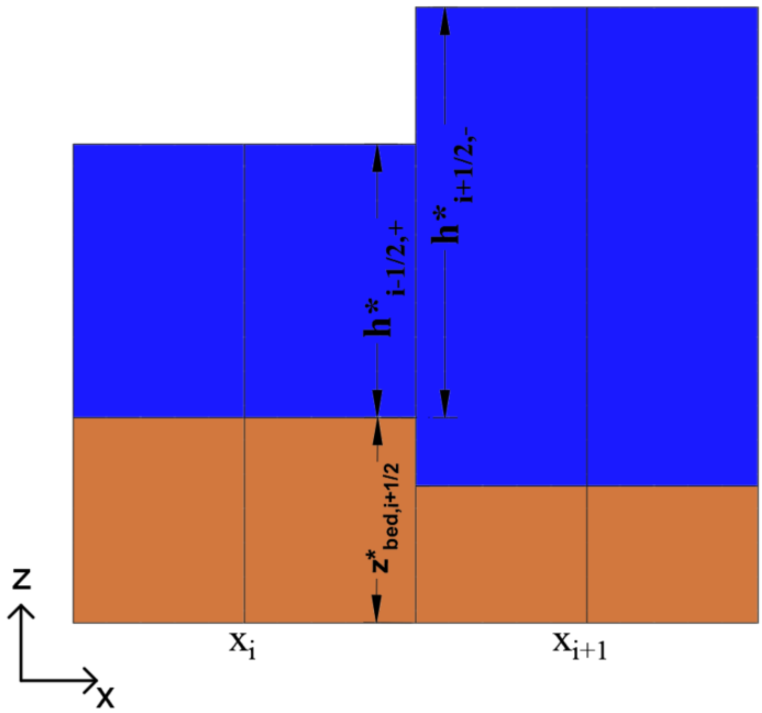

Figure 4.2: Hydrostatic Reconstructed Variables

The source term written in 4.35 can be separated as follows;

$$S_i = \frac{g}{2}\left[\begin{pmatrix} 0 \\ {h^*_{i+\frac{1}{2}^-}}^2 - {h_i}^2 \end{pmatrix} + \begin{pmatrix} 0 \\ {h_i}^2 - {h^*_{i-\frac{1}{2}^+}}^2 \end{pmatrix}\right] \tag{4.42}$$

Eventually, integrating the equation 4.42 into the equation 4.31.

$$\Delta x_i \frac{d}{dt} U_i(t) + F^{left}_{i+\frac{1}{2}}\left(U_i, U_{i+1}, z_{bed,i}, z_{bed,i+1}\right)$$
$$-F^{right}_{i-\frac{1}{2}}\left(U_{i-1}, U_i, z_{bed,i-1}, z_{bed,i}\right) = 0 \qquad (4.43)$$

Where;

$$F^{left}_{i+\frac{1}{2}}\left(U_i, U_{i+1}, z_{bed,i}, z_{bed,i+1},\right) = F_{i+\frac{1}{2}}\left(U_{i+\frac{1}{2}}{}^{l}, U_{i+\frac{1}{2}}{}^{r}\right) + \frac{g}{2}\begin{pmatrix} 0 \\ {h_i}^2 - {h^*_{i-\frac{1}{2}}{}^{r}}^2 \end{pmatrix} \quad (4.44)$$

$$F^{right}_{i-\frac{1}{2}}\left(U_{i-1}, U_i, z_{bed,i-1}, z_{bed,i},\right) = F_{i+\frac{1}{2}}\left(U_{i+\frac{1}{2}}{}^{l}, U_{i+\frac{1}{2}}{}^{r}\right) + \frac{g}{2}\begin{pmatrix} 0 \\ {h_i}^2 - {h^*_{i-\frac{1}{2}}{}^{r}}^2 \end{pmatrix} \quad (4.45)$$

4.6 Validation of Numerical Model

The numerical model for the granular flow is validated based on the laboratory experiments carried out in Heller & Hager, 2010. Prismatic channel with horizontal bed and rectangular slide are set up as shown in Figure 4.3. The granular flow begins sliding over the inclined bed with non-zero initial velocity when the front face holding the slide was removed (Heller & Hager, 2010). Table 4.1 shows the parameters in the experiment setup.

Numerical parameters employed in Ma et al., 2015 for the validation of this experiment are utilized in this thesis. Internal friction angle of the soil ($\emptyset_{int}$) and friction angle of the bed ($\emptyset_{bed}$) are 34° and 24°, respectively. Density of the granular flow is $1678\ kg/m^3$. Degree of fluidization is designated as zero when the landslide is in touch with the atmosphere and 0.25 when the landslide is entirely inside the water.

Two Laser Distance Sensors (LDS_{-1} and LDS_0) are used to record the deformations of the granular flow on certain points and the depth of the granular flow for both laboratory and numerical experiments is demonstrated in Figure 4.4.

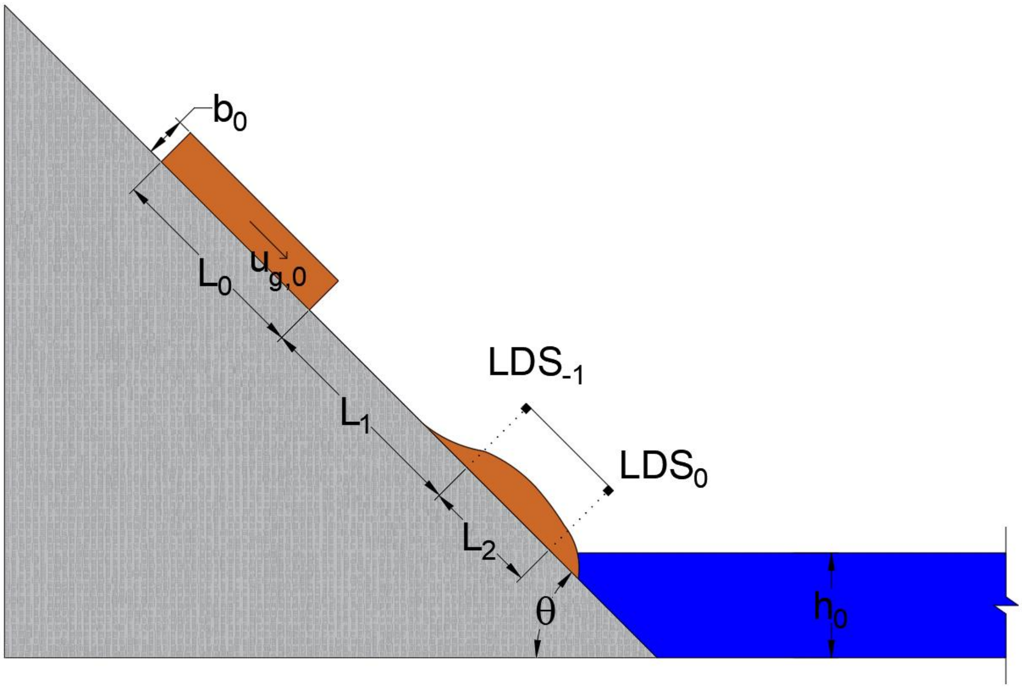

Figure 4.3: Experimental Geometry Conducted in Heller & Hager, 2010

Table 4.1: Variables in Experimental Setup

b_0 (m)	L_0 (m)	L_1 (m)	L_2 (m)	θ (º)	h_0 (m)	$u_{g,0}$ (m/s)
0.118	0.6	0.639	0.333	45	0.3	3.25

The time is set as zero when the landslide begins to interact with the water. The granular flow in the numerical model lasted shorter compared to the laboratory experiment. This difference may be because the code is one-dimensional. However, the numerical model for the granular flow is sufficient for further investigation.

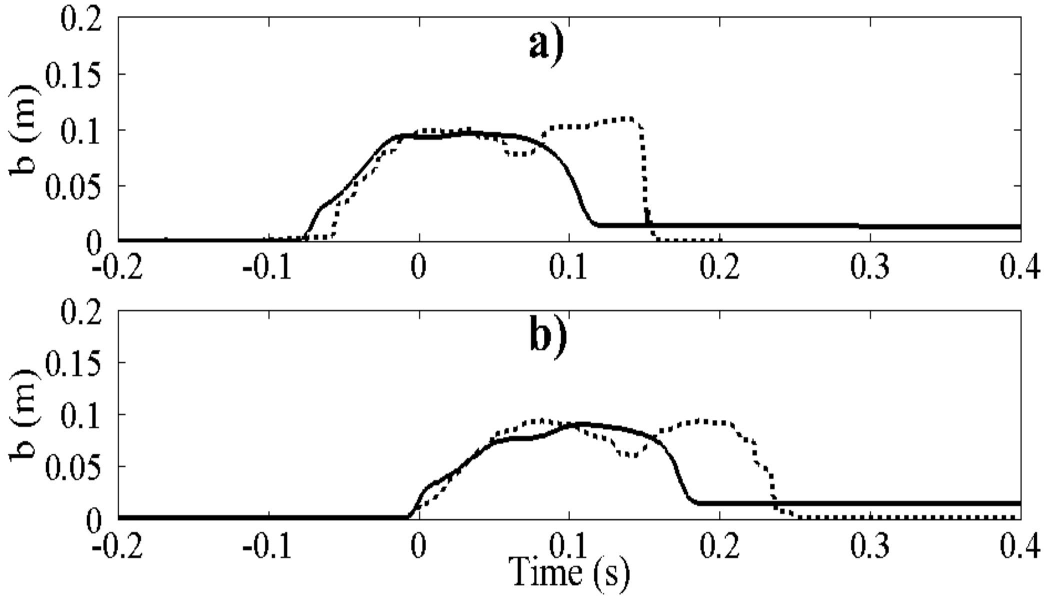

Figure 4.4: Laboratory (dashed line) and Numerical (Solid line) Experiments measured at a) LDS-1 and b) LDS0

CHAPTER 5

NUMERICAL RESULTS & DISCUSSIONS

Numerical simulations performed in this study may be divided into two groups, as one-layer and two-layer modeling. It is classified as one-layer when the sliding mass is represented by water volumes outside of the reservoir. In two-layer modeling the sliding soil mass and the deforming water volume in the reservoir are computed by two separate sets of depth integrated Shallow Flow Equations. However, when the sliding mass moves into the water reservoir, the water volume above the soil volume with a moving interface in between allows interaction of the two layers while they are in contact with each other. Besides, the two-layer landslide-generated waves are studied by branching more out based on the deformation type, observed failure plan and location of the landslide mass.

Similar featured numerical simulations are gathered around test groups which are shown in Table 5.1. Here, Test Cases B, C, D and E are the two-layer landslide modelling with specific landslide characteristics. Apart from the other test cases, Test Cases E also consider the earthquake.

Table 5.1: Model Description of Test Cases

Test Cases	Model Description
A	One-Layer Modelling
B	Rigid Block Modelling
C	Two-Layer Translational Modelling
D	Two-Layer Circular Modelling
E	Two-Layer Circular Landslide and Earthquake Modelling

Landslide generated waves, their propagation and maximum wave rises are investigated through a one-dimensional shallow flow model. Energy transfer from the slide mass to water volume in the reservoir is evaluated in terms of dimensionless quantities.

5.1 Test Cases A

One-layer model is formed by replacing the slide mass with equivalent volume of water. The numerical test domain is shown in Figure 5.1. A triangular prism of water volume is placed on the inclined slide surface to represent the slide mass. Prismatic channel with horizontal bed is set up and the slide is left free to move down from the inclined ramp.

In fact, since the slide material is assumed to be water, there are no parameters that imitate the inherent behavior of the actual landslide material, such as the internal friction angle of the soil. Therefore, only volume of the slide (V_0) and initial potential energy ($E_{pot,0}$) of the slide water are assumed to represent the actual landslide material characteristics. The slide angle (θ), initial water depth (h_0) and runaway distance (L_s) are the other variables of this test case.

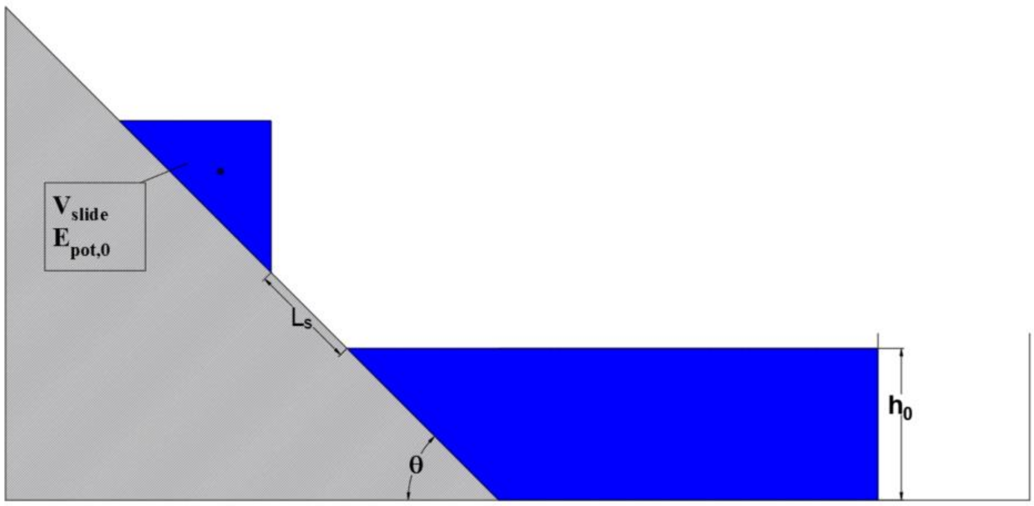

Figure 5.1: Assumed Test Geometry for the One-Layer Model

The range of variables considered in each test case, to understand the effects of the variables into the wave propagations, are shown in Table 5.2.

Table 5.2: Definition of Variables Range for Test Cases A

	Case-A1	**Case-A2**	**Case-A3**	**Case-A4**
Volume of Slide (m^3)	21.65	21.65	21.65	21.65 - 24.99 30.03 - 35.03 39.96 - 45.03 50.00
Initial Potential Energy of Slide (MJ)	3065.80	482.05 - 636.98 - 778.52 - 931.59 - 1115.71 1226.90	931.59	931.59 - 1155.60 1522.13 - 1917.45 2336.47 - 2794.78 3270
Runaway Distance (m)	46.99 - 27.07 18.76 - 14.21 11.23 - 10.00	0	0	0
Slide Angle (^{o})	15 - 25 35 - 45 55 - 60	15 - 25 35 - 45 55 - 60	45	45
Initial Water Depth (m)	5	5	5 - 8 10 - 15 25 - 40	5

The parameters of numerical solution are set as follows; simulation time is 20 seconds, computational cell size is 0.01 meter, the Courant-Friedrichs-Lewy (CFL) number for stability is 0.9 and the manning coefficient, n is 0.03. Appropriate time step is computed from the CFL number for every time step. In the first 5 seconds of the simulation smaller time steps are used to observe the slide mass deformation in detail.

The results of 4 cases are illustrated in Figures 5.2 and 5.3. As mentioned in section 3.4.2, for the one-layer landslide generated waves, energy transfer ratio uses only the initial potential energy of the slide in Equation 3.38.

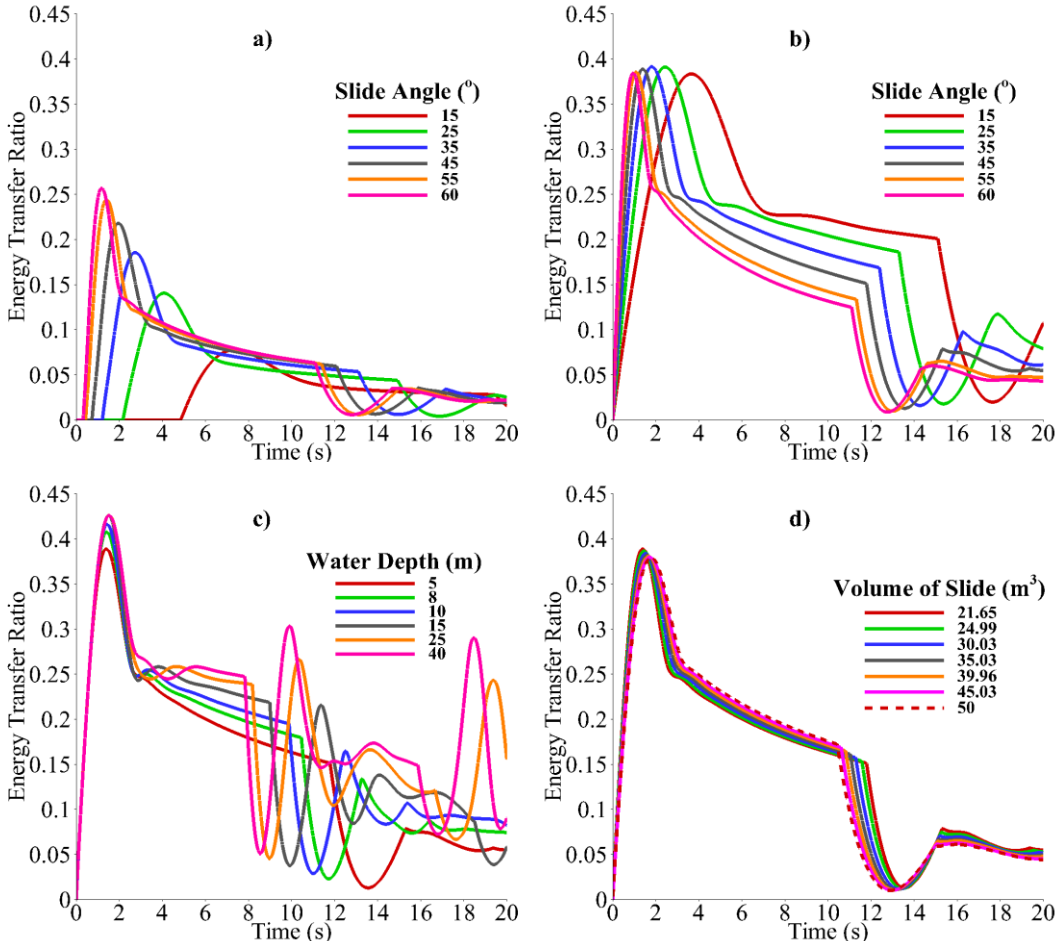

Figure 5.2: Energy Transfer Ratio vs. Time a) for Case-A1; b) for Case-A2; c) for Case-A3; d) for Case-A4

Cases-A1 & A2 consider the slide angles, from 15° to 60°. However, observing the energy transfer ratios related to the slide angle for identical volumes of the slide may be misleading because, the slide angle can change the initial potential energy of the slide. This problem is tackled by considering two cases. In Case-A1, the runaway distances are set properly to equalize the initial potential energy of the slide.

When the slide angle gets milder, runaway distance becomes longer. Besides, to satisfy the same water depth level for the different slide angles, sub-water ramp distance, which is the distance of the ramp inside the water body, needs to be arranged too. Sub-water ramp distance increases, if slide angle gets milder. Variables of runaway distance and sub-water ramp distance for Case-A1 are illustrated in Table 5-3.

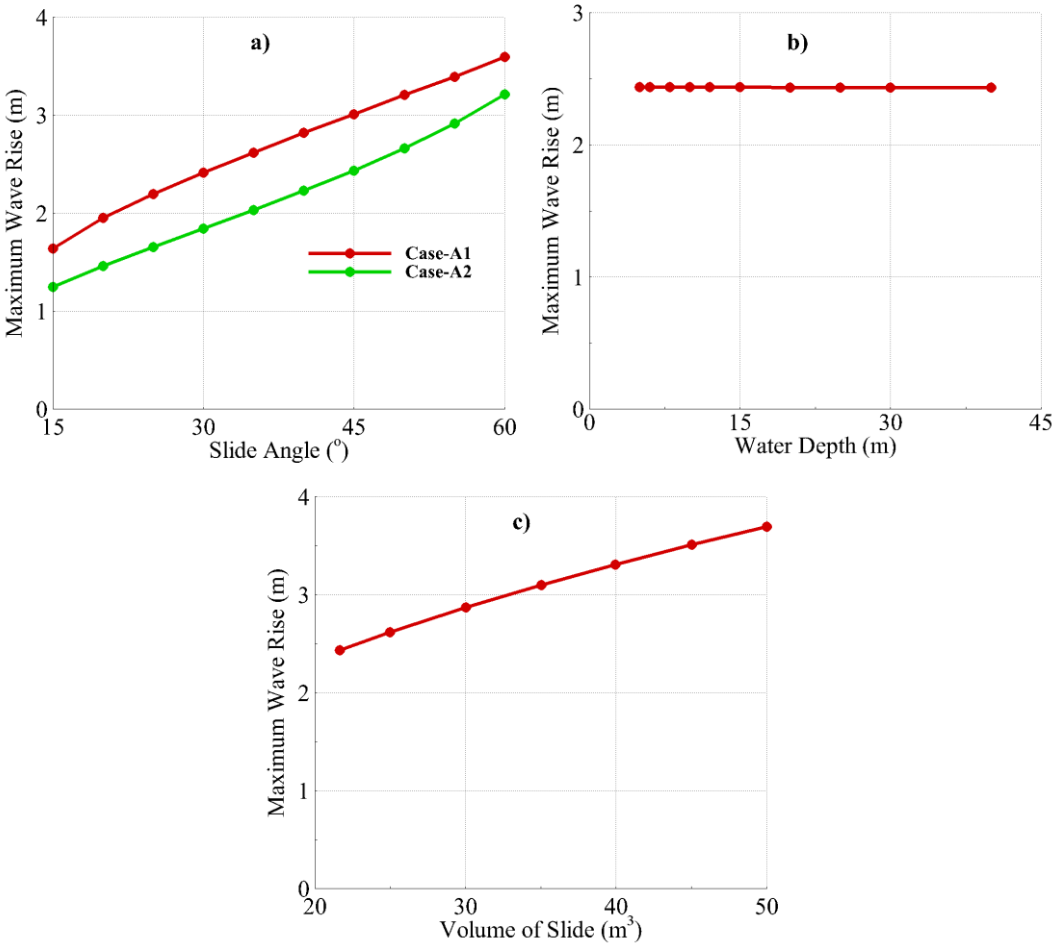

Figure 5.3: a) Maximum Wave Rise vs. Slide Angle for Cases-A1 & A2; b) Maximum Wave Rise vs. Water Depth for Case-A3 and c) Maximum Wave Rise vs. Volume of Slide for Case-A4

Energy Transfer Ratio (ETR) of Case-A1 is demonstrated in Figure 5.2/a. When the slide angle gets steeper, the peak ETR increases and the time required for reaching the peak ETR decreases.

However, an important fact is that the longer runaway distance leads the slide to move like an open channel because of the water as the material. In real cases, expecting the landslide like an open channel may not be common. Therefore, these results may not be accurate results. Furthermore, the first reaching time of waves into the spillway may be estimated by the ETR variations in time. When the waves are reached to the dam, the ETR decreases because significant portion of the energies contained by the water is transferred into spillway pool.

Table 5.3: Variables for Cases-A1 & A2

Slide Angle (°)	Sub-water Ramp Distance (m)	Runaway Distance for Case-A1 (m)	Initial Potential Energy of Slide for Case-A2 (kJ)
15	19.32	46.99	482.05
25	11.83	27.07	636.98
35	8.72	18.76	778.52
45	7.07	14.21	931.59
55	6.10	11.23	1115.71
60	5.78	10.00	1226.90

Figure 5.2/a also reveals that the steeper angle reaches the spillway with lesser time. An explanation is that the stepper angle slides transfer more energy to the reservoir and it results in fast wave velocities with the lesser required time to pour the water into the pool. On other hand, another explanation may be about sub-water ramp distance. The sub-water ramp distance increases when the slope decreases. This leads to enlarge in dam reservoir. Therefore, wave propagation for milder slopes needs to pass longer path to pour into the pool.

Consequently, it is understood that due to longer runaway distance, the slide tends to behave like an open channel flow and it may mislead the results. Therefore, in Case-A2, the runaway distance is set as zero to prevent the landslide from forming open channel characteristics. However, this time, it is not possible to set the initial potential energy of the slide constant due to the slide angle. Last column of Table 5.3 depicts the variation of the initial potential energy for Case-A2.

Figure 5.2/b shows the energy transfer ratio for Case-A2 and this result contradicts with Case-A1. More specifically, on contrary to Case-A1, the peak ETR does not change with the slide angle. However, there are similarities between Cases-A1 & A2. For instance, in the steeper angle ramp for Case-A2, the ETR reaches the peak faster. Besides, not only the required time to reach the peak ETR, but also the required time to spill decreases when the slide angle increases.

Moreover, the maximum wave rises of Cases-A1 & A2 are compared in Figure 5.3/a. It is observed that the maximum wave crest occurs when the slide angle gets steeper as in both cases. In addition, observing higher maximum wave rise may be explained by the initial potential energy and the peak ETR. For example, as depicted in Table 5.3, when the numerical experiment with the slide angle of 60^o is considered, the initial potential energy of the slide is 3065.80 kJ and 1226.90 kJ for Cases-A1 & A2, respectively. In certain situation, as illustrated in Figure 5.2/a & b, the peak ETRs are 0.26 and 0.38 for Cases-A1 & A2 respectively. Then, the maximum kinetic energy of the wave can be computed as 796.90 kJ and 466.22 kJ for Cases-A1 & A2. Having higher maximum kinetic energy of the wave may be the reason for the higher wave crests as in Case-A1 compared to Case-A2.

Case-A3 compares the initial water depths with the series of the numerical simulations to analyze the wave propagations. Here, arranging the initial water depth brings a technical problem. Specifically, if the initial water depth is increased by taking the bed elevation constant, the water surface of the certain initial water depth differs notably. Hence, the initial potential energy of the slide would differ considerably. Therefore, the water surface is taken as a reference to increase the depth and the depths are satisfied by lowering the bed. When constant initial potential energy of the slide is satisfied, it results in variations of sub-water ramp distance. When the initial water depth gets deeper, sub-water ramp distance increases.

The ETRs are shown in Figure 5.2/c. The peak ETR is almost identical for the different initial water depths. There are only small variations in the peak ETRs. This may be explained with the variation of the sub-water ramp distance. Furthermore, a decrease in the ETR occurs when the water waves reach into the dam body and some of the water volume pours into the downstream. Here, the required time for reaching the spillway decreases while increasing the initial water depth. Actually, it is expected, because the wave celerity increases when initial water depth is increased. An increase in the wave celerity results in more fast waves and lesser required time to reach the spillway.

Figure 5.3/b indicates that the maximum wave rise is almost the same for different initial water depths. Therefore, it can be concluded that the initial water depths are not one of the major parameters that affects the energy transfer ratio and the maximum wave crest.

Case-A4 is introduced to observe the effect of slide volume changes. Changing the slide volume is responsible from variation of the initial potential energy of the slide, because the landslide mass changes with the slide volume. Therefore, outcomes are required to be considered not only for volume of slide but also initial potential energy of the slide.

Figure 5.2/d indicates that the slide volume has a slight impact on the energy transfer ratio. It may be explained in a such way that variation of the kinetic energy of the wave with respect to time is higher in equation 3.38. Therefore, the wave kinetic energy becomes essential rather than the initial potential energy of the slide.

Figure 5.3/c demonstrates maximum wave rise for different slide volumes. The maximum wave crest increases when the volume of the slide is enlarged. In fact, an increase in the slide volume of the initial potential energy of the slide creating large potential impacts and disturbance on the water reservoir can be expected for real events.

Summary of observations for Test Case A:

a) Energy transfer ratio increases with runaway distance increased by the slide angle.
b) Energy transfer ratio is independent of initial potential energy increased by slide angle.

c) Energy transfer ratio is independent of initial water depth and volume of slide.
d) Maximum wave rise increases with slide angle.
e) Maximum wave rise is independent of initial water depth.
f) Maximum wave rise increases with volume of slide.

5.2 Test Cases B

The rigid landslide means that the landslide does not deform while moving. It is one of the common methods in simulating the landslide generated waves in laboratory experiments. Rigid models may differ depending on the velocity definition of the sliding block and slide path-line. In this study, the rigid slide is assumed to move at constant velocity along a straight path at a constant slope (Figure 5.4). The reservoir length is assumed long enough so that the generated waves cannot reach the dam body and overflow is not considered. The parameters of this setup are the initial water depth (h_0), slide angle (θ), slide height (b_0), slide length (L_0), front face angle (β) and velocity of slide (U_{rigid}).

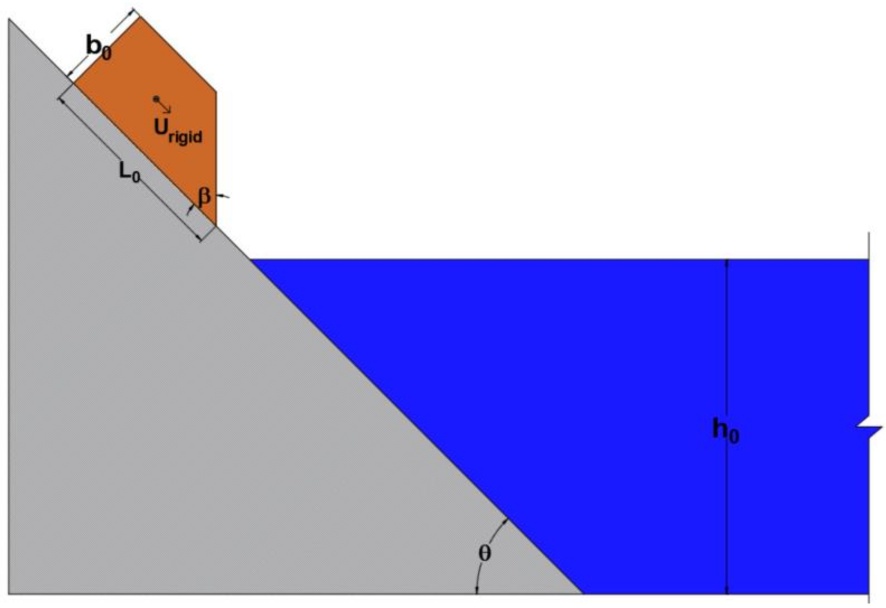

Figure 5.4: Assumed Test Geometry for the Rigid Block Model

A total of 6 test cases are considered with rigid block slide. Range of variables for all cases are shown in Table 5.4. Total simulations time is 20 seconds with 0.1 seconds time step size. Computational cell size is 0.5 meter, the CFL number for stability is 0.9 and the Manning coefficient is 0.03.

Table 5.4: Definition of Variables Range for Test Cases B

Case	Volume of Slide (m^3)	Rigid Slide Height (m)	Length of Slide (m)	Front Face Angle of Slide (°)	Velocity of Slide (m/s)	Initial Water Depth (m)	Slide Angle (°)
B1	20.31 47.03 62.35 81.57	1.41- 3.54- 4.95- 7.07	15.07	45	5	25	45
B2	20.35 47.03 62.35 81.57	3.54	7.51- 15.07- 19.40- 24.84	45	5	25	45
B3	47.03	3.54	19.90- 17.09- 15.83- 15.07	15-25- 35-45	5	25	45
B4	47.03	3.54	15.07	45	3-5-8	25	45
B5	47.03	3.54	15.07	45	5	25-30 40-50	45
B6	47.03	3.54	15.07	75-65 55-45 35-30	5	25	15-25 35-45 55-60

Cases-B1 & B2

In the first two cases, slide volume is the variable. For a one-dimensional test case slide volume can be affected by a change in slide height as in Case-B1 or by a change in slide length as in Case-B2.

The results of Case-B1 and Case-B2 are shown in Figure 5.5. Kinetic and Potential Energy Transfer Ratios are indicated for Cases-B1 & B2 in Figures 5.5/a, b, c & d. It is observed that Kinetic Energy Transfer Ratio (KETR) is almost identical with

Potential Energy Transfer Ratio (PETR) for both cases. Besides, KETR and PETR can be explained with a relation, b_0/L_0, because thickening as in Case-B1 or shortening as in Case-B2 of the rigid slide led to increasing this relation and the energy transfer ratios. However, unlike the energy transfer ratios, the maximum kinetic energy of the landslide increases for both cases when the slide volume is increased as shown in Figure 5.5/e. In fact, it is expected to observe a decrease in the energy transfer ratios with an increment of the maximum kinetic energy of the landslide in Case-B1, considering equations 3.30 and 3.31. Despite this situation, an increase in the energy transfer ratios can be related to the energies contained by the waves.

Figure 5.5/f compares the maximum wave rises of Cases-B1 & B2 with respects to volume of the rigid slide. Here, it is understood from a comparison of the slide volume that whereas the slide length does not affect the maximum wave crest, the slide height is a parameter on which the maximum wave rise depends. Additionally, Table 5.5 shows where and when the maximum wave crest is occurred. For rigid slide modelling, the point of the maximum wave rise is the distance between toe of the inclined ramp and the point of maximum wave rise. It is observed that the maximum wave crests occur almost at similar place and time.

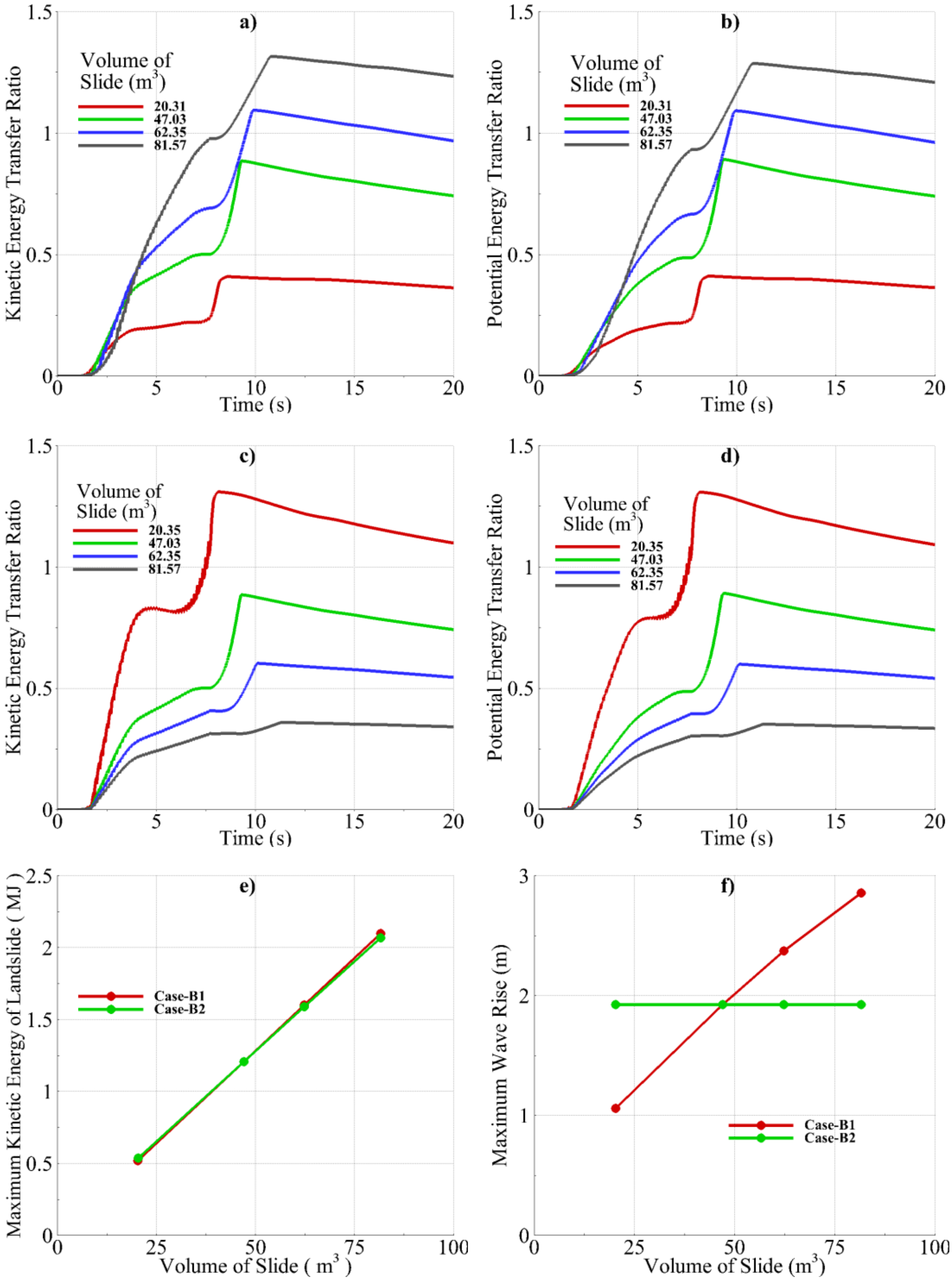

Figure 5.5: a) KETR vs. Time for Case-B1; b) PETR vs. Time for Case-B1; c) KETR vs. Time for Case-B2; d) PETR vs. Time for Case-B2; f) Maximum Kinetic Energy of the Landslide vs. Volume of Slide for Cases-B1 & B2 e) Maximum Wave Rise vs. Volume of Slide for Cases-B1 & B2

Table 5.5: Point and Time of Maximum Wave Rise for Cases-B1&B2

Volume of Slide (m^3)	**Point of Maximum Wave Rise for Case-B1 (m)**	**Time Required for Maximum Wave Rise for Case-B1 (s)**	**Point of Maximum Wave Rise for Case-B2 (m)**	**Time Required for Maximum Wave Rise for Case-B2 (s)**
20.31	0.5	3.57	0.5	3.54
47.03	0.5	3.54	0.5	3.54
62.35	0.5	3.67	0.5	3.54
81.57	0.5	4.14	0.5	3.54

Case-B3 is presented to understand the effects of front face angle of slide to the wave generation. Previously, it is pointed out that the slide height is an important parameter for rigid slide modelling. However, structure of the rigid slide may put the results of slide height into discussion. More specifically, if the slide geometry has a shape with narrower front face, splash behavior of the rigid slide can particularly differ so that the wave propagations through the dam reservoir can be affected. Additionally, when front face of the slide is varied, slide volume changes. Since slide length has relatively small effects on the results, slide volume is arranged with modification of slide length rather than the slide height in order to focus more on the front face angle of the slide. Figure 5.6/a & b demonstrate KETR and PETR for different front face angle of slide, respectively. As the front face angle of slide is increased, the energy transfer ratios increase up to certain point.

Moreover, as shown in Figure 5.6/c, maximum wave rise occurs when the front face angle of slide is maximum. However, it causes a small increment in the maximum wave crest.

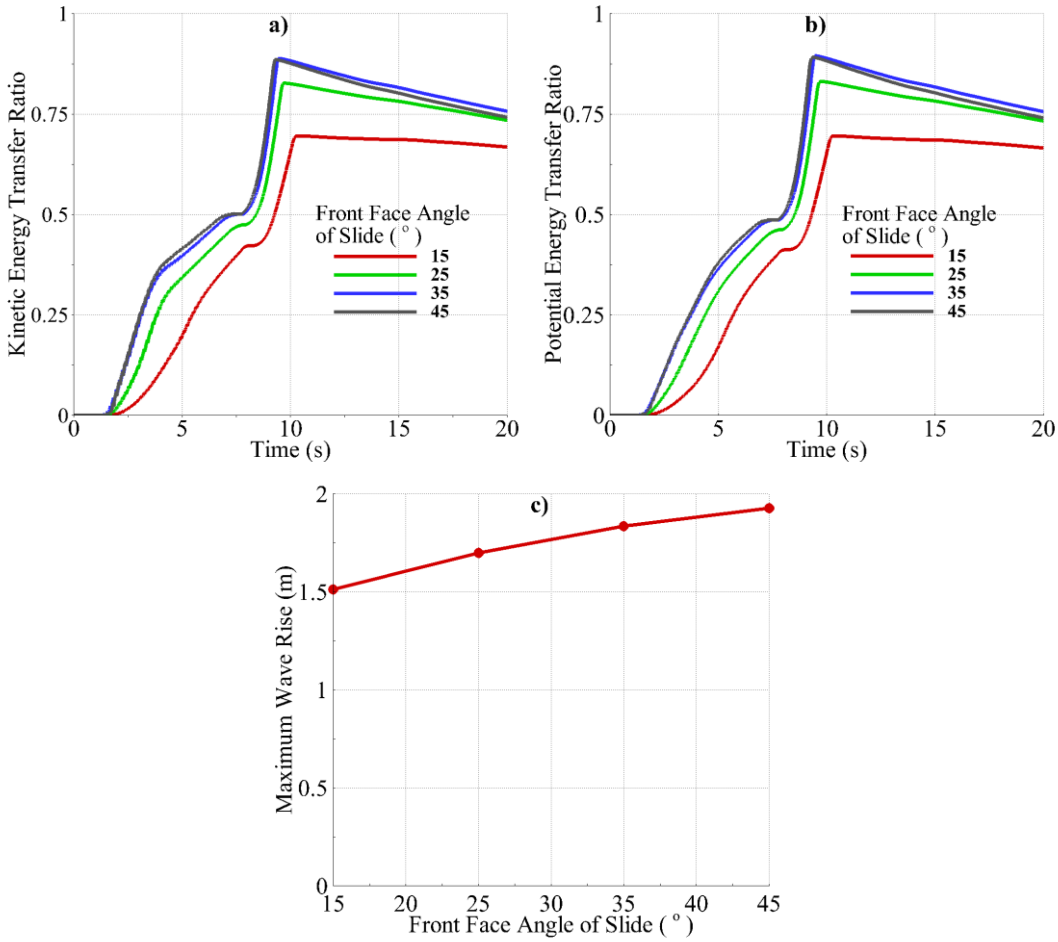

Figure 5.6: For Case-B3; a) KETR vs. Time, b) PETR vs. Time, c) Maximum Wave Rise vs. Front Face Angle of Slide

Table 5.6: Point and Time of Maximum Wave Rise for Case-B3

Front Face Angle of Slide (°)	Point of Maximum Wave Rise (m)	Time Required for Maximum Wave Rise (s)
15	0.5	5.86
25	0.5	4.54
35	0.5	3.55
45	0.5	3.54

Based on Table 5.6, the maximum wave crest occurs at the toe of inclined ramp for every front face angle of slide. However, sharper front face takes more time to reach the maximum wave crest. The reason is that the slide height horizontally moves away from toe of the inclined ramp when the front face angle of the slide gets sharpened.

Case-B4 investigates velocity of slide with the series of the numerical simulations. Figure 5.7/a & b point out that when the velocity of slide is increased, KETR and PETR tend to decrease and also, the time required to observe peak energy transfer ratios decreases. A decrease in time makes sense, because slide moves faster.

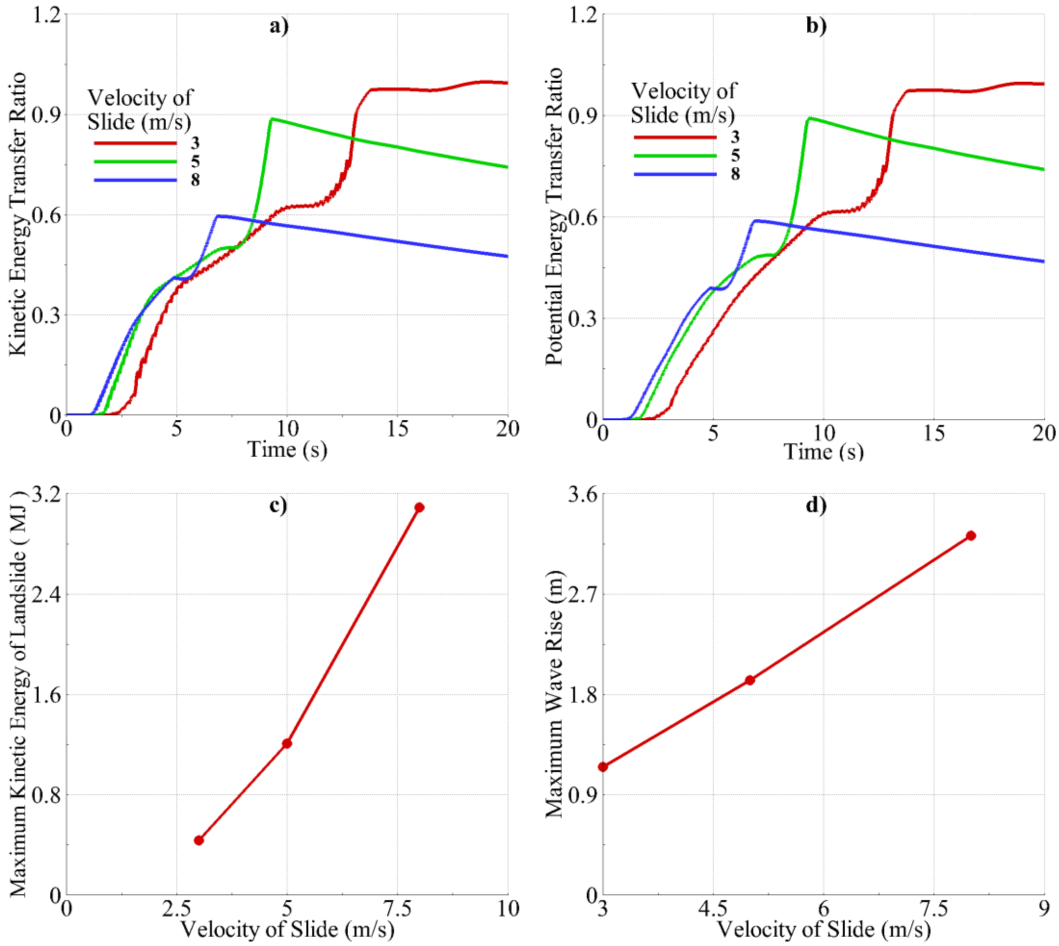

Figure 5.7: For Case-B4; a) KETR vs. Time, b) PETR vs. Time, c) Maximum Kinetic Energy of Landslide vs. Velocity of Slide and d) Maximum Wave Rise vs. Velocity of Slide

The relationship with the energy transfer ratios and velocity of slide can be explained with Figure 5.7/c. Particularly, square of the slide velocity is directly proportional with the maximum kinetic energy of slide (equation 3.32). Then, as stated in equations 30 and 31, the energy transfer ratios decrease when maximum kinetic energy of landslide increases.

Table 5.7: Point and Time of Maximum Wave Rise for Case-B4

Velocity of Slide (m/s)	Point of Maximum Wave Rise (m)	Time Required for Maximum Wave Rise (s)
3	0.5	4.85
5	0.5	3.54
8	0.5	2.85

Furthermore, landslide velocity causes a linear increase in the maximum wave crest height (Figure 5.7/d). Similar to the required time for reaching the peak energy transfer ratios, reaching the maximum wave crest takes time when the landslide moves slower as shown in Table 5.7.

In **Case-B5**, the series of the numerical experiments are performed to investigate the impacts of initial water depth to the wave generation and the results are presented in Figure 5.8.

KETR and PETR are shown in Figures 5.8/a & b and these results are almost similar. Only difference observed is at abrupt jump. Here, as the abrupt jump refers to the second or third waves, these variations are generally complex but they are generally small.

Figure 5.8/c shows that when water depth gets deeper, maximum wave rise tends to decrease. A decrease in wave crest due to variation of initial water depth may be explained by stating that deeper depth causes an increase in wave celerity causing less maximum wave rise. However, this logic is contradicted with the time required for maximum wave rise. Because, according to Table 5.8, when the initial water depth is increased, it takes more time to reach the maximum wave crest. Here, sub-water ramp distance may be significant for Case-B5. The free surface of the water is taken as a reference; therefore, depths are arranged by lowering the bed. When the initial water depth gets deeper, sub-water ramp distance increases. Eventually, although wave celerity increases with deeper waves, it also elongates the distance in which the landslide moves too.

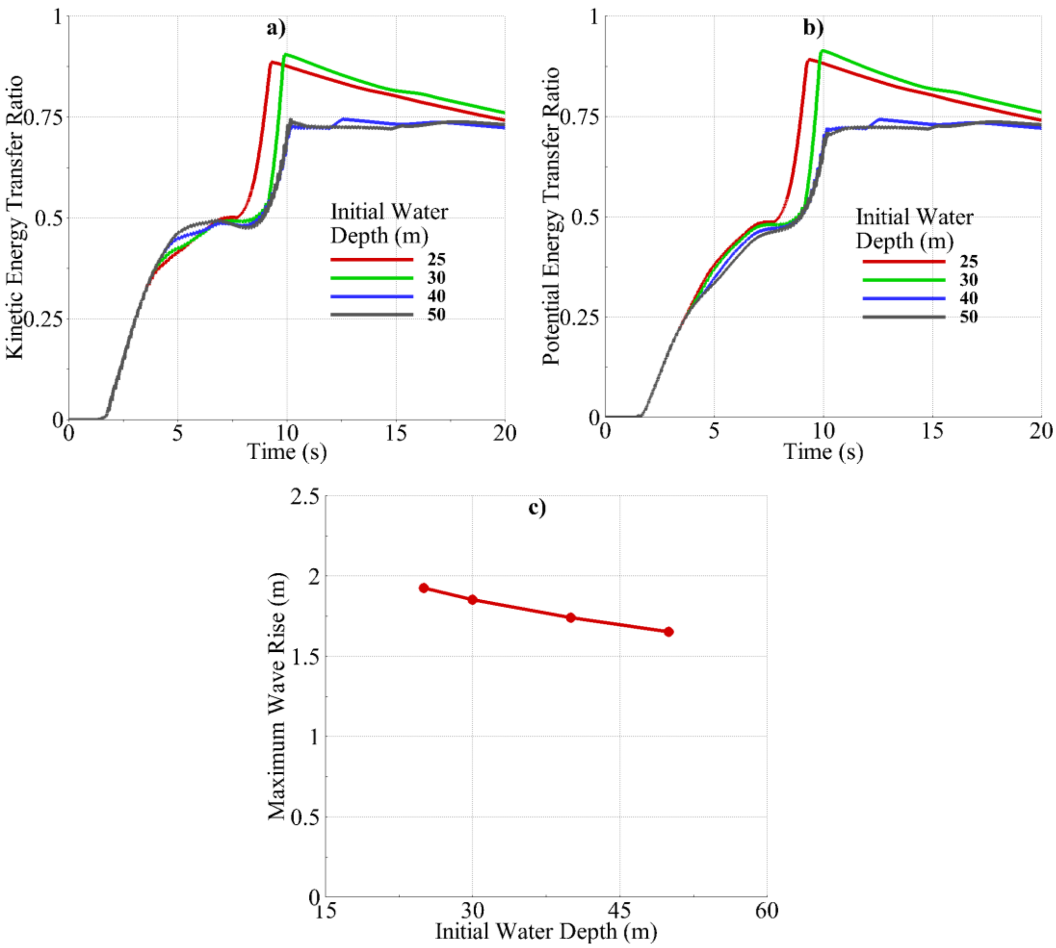

Figure 5.8: For Case-B5; a) KETR vs. Time, b) PETR vs. Time, c) Maximum Wave Rise vs. Initial Water Depth

Table 5.8: Point and Time of Maximum Wave Rise for Case-B5

Initial Water Depth (m)	**Point of Maximum Wave Rise (m)**	**Time Required for Maximum Wave Rise (s)**
25	0.5	3.54
30	0.5	3.83
40	0.5	4.35
50	0.5	4.81

Case-B6 performs the numerical simulations varying the slide angle from 15° to 60°. As illustrated in Table 5.4, the front face angle of the slide is also arranged based on the slide angle, because to reduce other impacts on the wave propagations, the front faces are defined similarly by arranging the normal direction. Additionally, the slide length is set accordingly too as listed in Table 5.4.

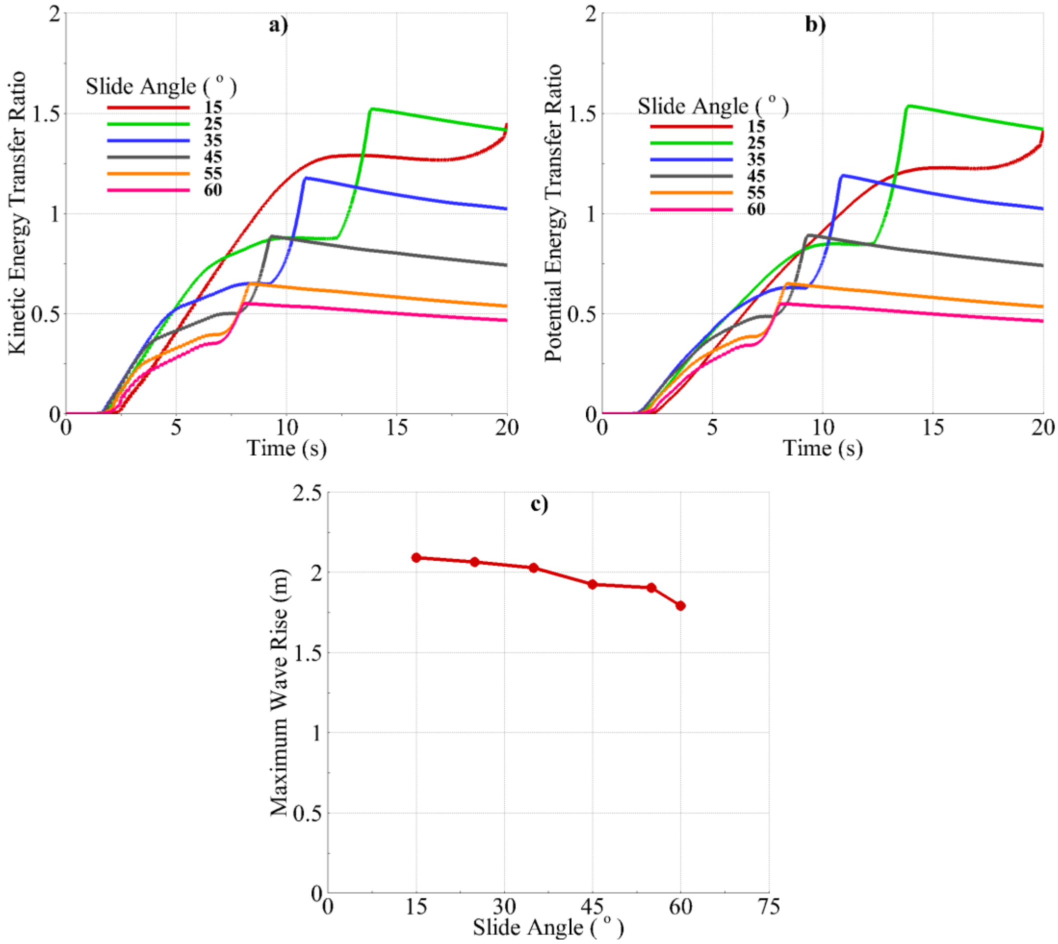

Figure 5.9: For Case-B6; a) KETR vs. Time, b) PETR vs. Time, c) Maximum Wave Rise vs. Slide Angle

Figures 5.9/a & b consider KETR and PETR, respectively. It is revealed that when slide angle is decreased, the energy transfer ratios tend to increase. Besides, the numerical simulation with 15° of slide angle is still affected by landslide, because wave propagation process, near- and far- fields, can be understood by observing continuous decrease in the energy transfer ratios with respect to time. Another fact is that time required for peak KETR and PETR decreases with steeper slide angle. It is because submarine ramp distance requires to be increased with the milder slide angle.

Table 5.9: Point and Time of Maximum Wave Rise for Case-B6

Slide Angle (°)	**Point of Maximum Wave Rise (m)**	**Time Required for Maximum Wave Rise (s)**
15	0.5	9.57
25	0.5	5.82
35	0.5	4.28
45	0.5	3.54
55	0.5	3.24
60	0.5	3.31

Figure 5.9/c states that a decrease in wave crest occurs when the slide angle becomes steeper. However, range of maximum wave rise is relatively small. Besides, Table 5.9 demonstrates that due to submarine ramp distance, the milder slopes take more time to produce the maximum wave rise.

Summary of observations for Test Case B:

a) Maximum kinetic energy of the slide can be affected either by increasing the length or height of the block. However, the energy transfer rate is proportional to thickness of the block rather than the volume.
b) Maximum wave rise increases with the block height being insensitive to volume increased by block length.
c) Maximum wave rise increases with the front face angle of the block.
d) Maximum wave rise increases with velocity of the block.
e) Maximum wave rise decreases with initial water depth in the reservoir.
f) Maximum wave rise decreases with slide angle.

5.3 Test Cases C

The translational failure plane occurs when the surface of the landslide is parallel to the failure surface. These landslides are relatively longer mass failure with shallow thickness. This is called an infinite slope. Numerical solutions for the translational landslide are also performed as partially subaerial which is the situation in which a part of the sliding mass is already inside the water reservoir.

Figure 5.10 indicates the geometric setup and the variables of the translational landslide model. Far-field condition is applied on the dam side. Initial dam reservoir bathymetry is assumed to be horizontal plane surface.

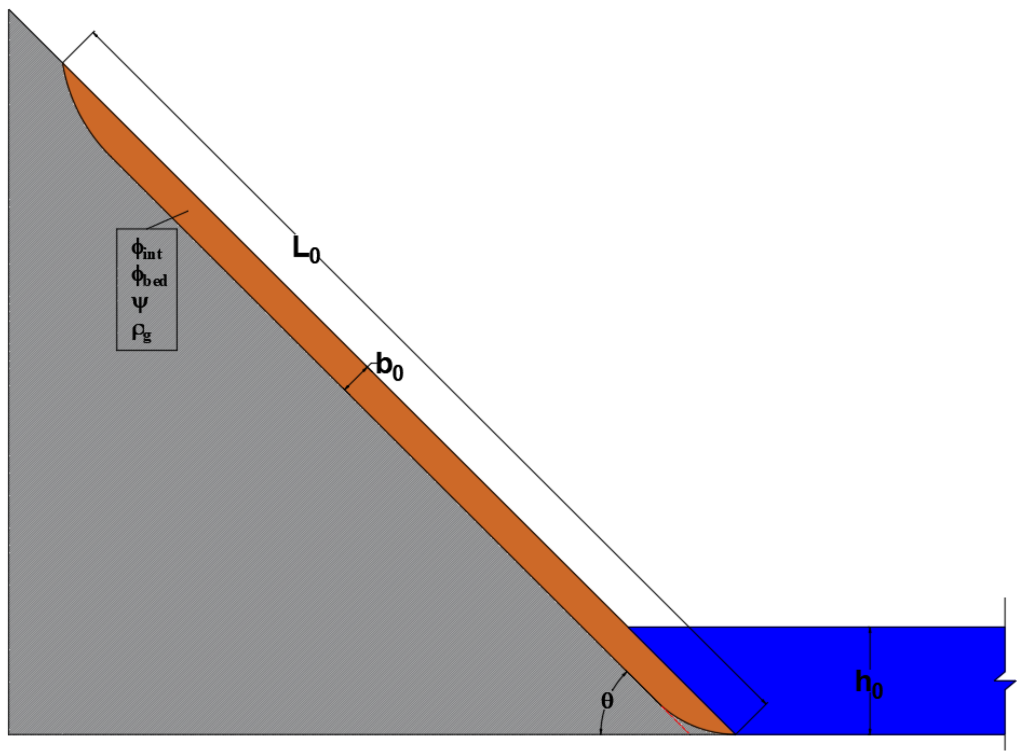

Figure 5.10: Assumed Test Geometry for the Two-Layer Translational Landslide Model

Initial water depth (h_0) and the slide angle (θ) are considered for the environmental constraints of this case. Slide thickness (b_0), slide length (L_0), internal friction angle of soil ($\emptyset_{int}$), friction angle of the bed ($\emptyset_{bed}$), degree of fluidization (ψ), density of the landslide (ρ_g) and the Manning's roughness are the parameters involved in the investigation.

For the translational model, numerical tests are performed for various values of the 9 parameters involved in this model as shown in Table 5.10.

Table 5.10: Definition of Variables Range for Test Cases

Cases	Volume of Slide (m^3)	Thickness of Slide (m)	Length of Slide (m)	Slide Angle (º)	Initial Water Depth (m)	Internal Friction Angle of Soil (º)	Friction Angle of Bed (º)	Degree of Fluidization	Density of Granular Flow (kg/m^3)	Manning Coefficient
C1	86.38-170.03-251.13-330.10-406.49-739.02	1-2-3-4-5-10	88.39	45	10	40	40	0.3	2000	0.03
C2	85.66-172.64-251.13-329.62-405.98-739.03	3	33.23-62.23-88.39-114.55-140.01-251.02	45	10	40	40	0.3	2000	0.03
C3	240.70-247.25-251.42-251.13-248.16-246.61	3	88.39	15-25-35-45-55-60	10	40	40	0.3	2000	0.03
C4	251.13-261.74-272.34-282.95-293.56-314.77	3	88.39	45	10-15-20-25-30-40	40	40	0.3	2000	0.03
C5	251.13	3	88.39	45	10	25-30-35-40-45	25-30-35-40-45	0.3	2000	0.03
C6	251.13	3	88.39	45	10	45	25-30-35-40-45	0.3	2000	0.03
C7	251.13	3	88.39	45	10	40	40	0.1-0.3-0.5-0.7-0.8	2000	0.03
C8	251.13	3	88.39	45	10	40	40	0.3	1500-1700-1850-2000-2200	0.03
C9	251.13	3	88.39	45	10	40	40	0.3	2000	0.03-0.07-0.11-0.15

Cases-C1 & C2 are introduced to study slide volume effects on the wave generation. Volume of the slide can be changed by varying thickness (Case-C1) or length (Case-C2) of the slide. Figure 5.11/a & b indicate KETR and PETR of Case-1. Additionally, Figure 5.11/c &d show KETR and PETR of Case-C2. Surprisingly, whereas KETR and PETR values tend to increase when the slide volume increases in Case-C1, KETR and PETR values behave differently in Case-C2. In fact, similar relation was observed in Test Cases B, b_0/L_0, can explain the slide volume comparisons of Translational Landslide Model. When this relation increases by thickening in Case-C1 or shortening in Case-C2 of the landslide, peak KETR and PETR prone to increase.

In fact, Figure 5.11/e, that shows the maximum kinetic energy of the landslide for Cases-C1 & C2, validates the relationship between b_0/L_0 and the energy transfer ratios. Especially, lengthening the slide results in more space for the acceleration of the landslide, thus the maximum kinetic energy of the landslide of Case-C2 exponentially increases. Because, considering equation 3.32, the maximum kinetic energy of the landslide is proportional to the square of the velocity of the landslide. However, in Case-C1, thickening does not affect the velocity significantly; hence, the maximum kinetic energy of the landslide of Case-C1 depends only on the mass of the landslide. Therefore, based on equations 3.30 and 3.31, slide length changes KETR and PETR more compared to slide thickness. Moreover, maximum wave rises for Cases-C1 & C2 are displayed in Figure 5.11/f. Regardless of lengthening and thickening of the landslide, maximum wave crest increases when the slide volume is increased. Table 5.11 demonstrates position and time required for maximum wave rise for Cases-C1 & C2. The point of the maximum wave rise is the distance between toe of the inclined ramp and the maximum wave crest and generally, it is observed where landslide run-out is finished. Due to an increase in slide volume, the landslide moves forward for both cases; however, the slide length is a dominant parameter after certain point, 250 m^3. Maximum kinetic energy of the landslide determines the point and time for the landslide runout inside the reservoir.

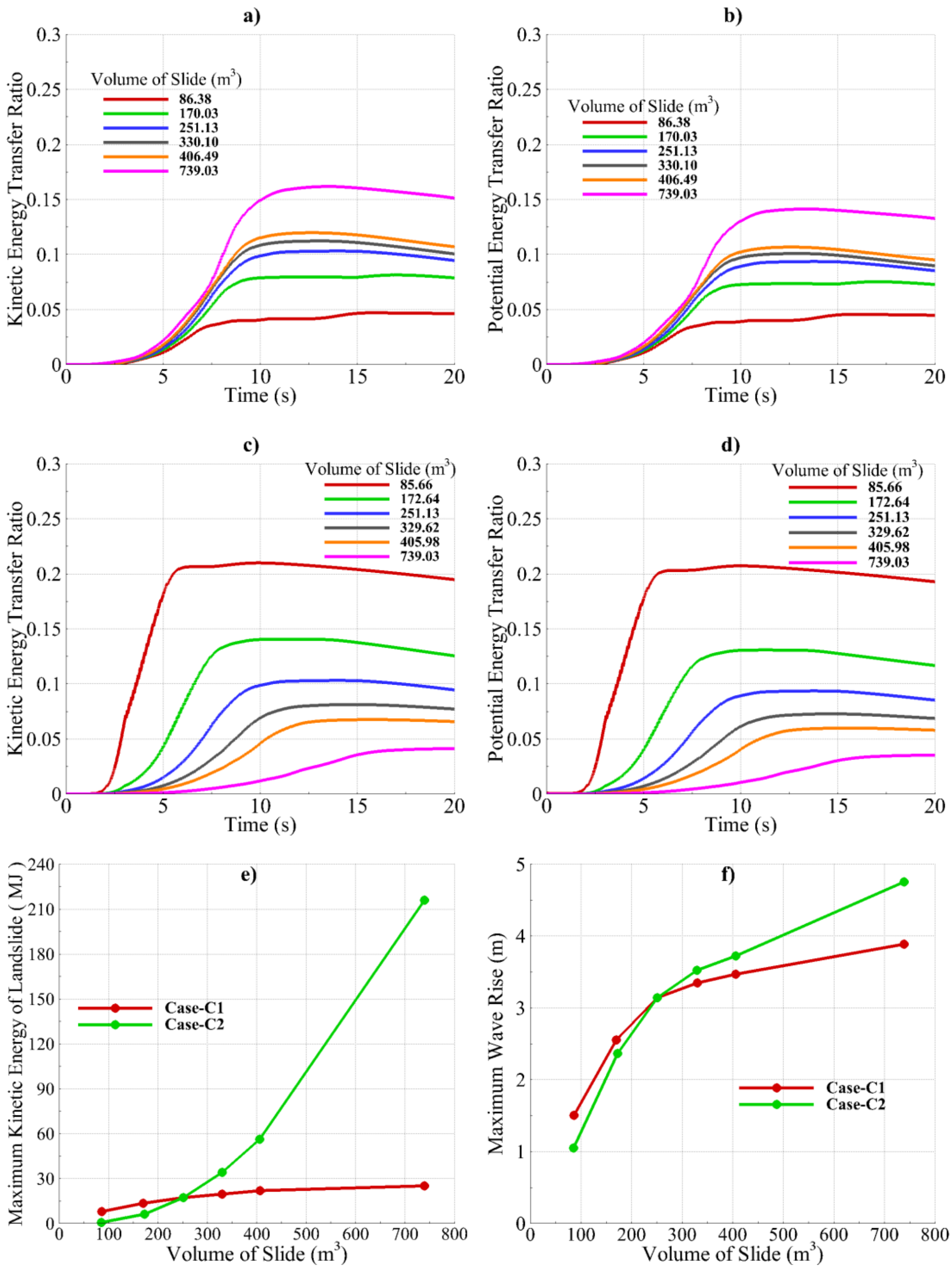

Figure 5.11: a) KETR vs. Time for Case-C1; b) PETR vs. Time for Case-C1; c) KETR vs. Time for Case-C2; d) PETR vs. Time for Case-C2; e) Maximum Kinetic

Energy of Landslide vs. Volume of Slide for Cases-C1 & C2 and f) Maximum Wave Rise vs. Volume of Slide for Cases-C1 & C2

Table 5.11: Point and Time of Maximum Wave Rise for Cases- C1 & C2 of Test Cases C

Volume of Slide (m^3)	Point of Maximum Wave Rise for Case-C1 (m)	Time Required for Maximum Wave Rise for Case-C1 (s)	Point of Maximum Wave Rise for Case-C2 (m)	Time Required for Maximum Wave Rise for Case-C2 (s)
86.38	14	6.51	9.5	3.93
170.03	23	7.35	19	5.83
251.13	27	7.45	27	7.45
330.10	28	7.32	31	8.35
406.49	29.5	7.03	37.5	10.04
739.02	39	8.09	58	14.26

Case-C3 considers slide angle from 15^o to 60^o. Here, slide volume varies with the slide angle due to geometric variation of inclined bed, but it is generally negligible.

Figure 5.12/ a & b show KETR and PETR with respect to time. Unlike the energy transfer ratios in other cases, PETR chart differs from the KETR chart. With this difference, an important capability of numerical code may be adverted.

It is analyzed that two numerical simulations with the slide angles of 15^o and 25^o bring an interesting fact into the discussion. The KETRs of them are small in the first ten seconds and an increase is observed later. However, the PETRs seem that they are starting to transfer energy to the water volume from the beginning. Actually, when these numerical simulations are observed from with the video animations, their landslides are stationary or negligibly small movements. Therefore, the wave kinetic energy becomes almost zero because there is no energy transfer to the water volume. However, due in part to numerical oscillations and very small effects of the landslides small wave potential energies are produced. Therefore, PETR curves can be misleading. Besides, it is revealed that the peak KETR and PETR increase when the slide angles are increased up to a certain point and after the slide angle of 45^o, KETR and PETR are prone to decrease. Therefore, the maximum energy transfer ratios cannot be obtained with steeper slide angle simulations. However, maximum kinetic energy of the landslide can be obtained as illustrated in Figure 5.12/c. When the slide angle is increased, maximum kinetic energy of the landslide increases. Previously, an inverse relationship between the energy transfer rates and the maximum kinetic energy of the landslide was observed. However, these results contradict with this relationship, because although the maximum kinetic energy of the landslide increases with the steeper slide angle, the energy transfer ratios do not decrease. Here, based on equations 3.30 and 3.31, to have maximum peak energy transfer ratios, the wave energies have to be more.

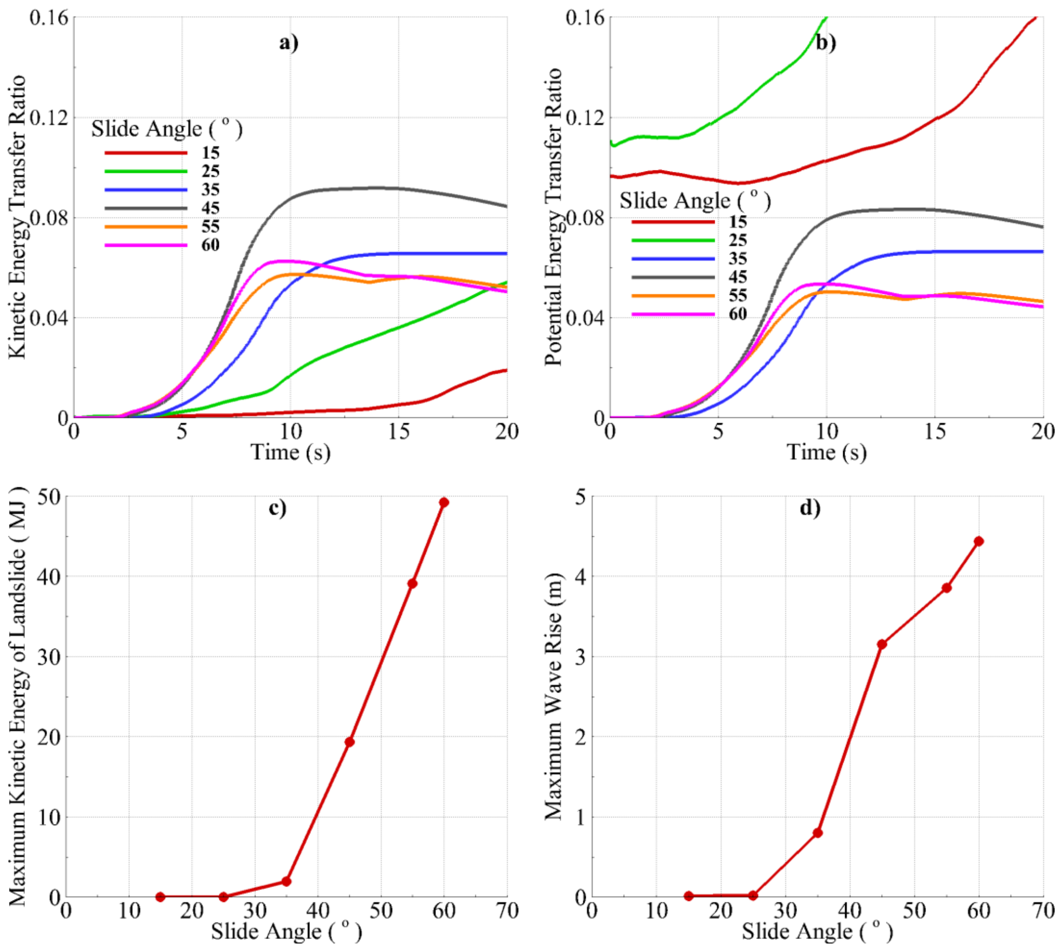

Figure 5.12: For Case-C3; a) KETR vs. Time, b) PETR vs. Time, c) Maximum Kinetic Energy of Landslide vs. Slide Angle and d) Maximum Wave Rise vs. Slide Angle

Moreover, the stability of the landslide in the numerical simulations with the slide angles of 15º and 25º can be understood from Figures 5.12/c & d, because there are no changes in maximum kinetic energy of the landslide and maximum wave rise. Figure 5.12/d points out that the maximum wave rise increases with a steeper angle. Furthermore, KETR and PETR can have an influence on the maximum wave rise, because when the numerical simulation with a slide angle of 45º is not considered, the maximum wave rise graph behaves like a straight line. However, the numerical simulation with a slide angle of 45º exceeds the linear behavior of the graph. It may be assumed that the higher energy transfer ratios can be an indication of the maximum wave rise. It is probably because of a sign of containing great energy capacity of waves. In addition, Table 5.12 indicates that due to an increase in the maximum kinetic energy of the landslide, the landslide runout goes further with lesser time.

Table 5.12: Point and Time of Maximum Wave Rise for Case-C3 of Test Cases C

Slide Angle (º)	Point of Maximum Wave Rise (m)	Time Required for Maximum Wave Rise (s)
15	3	16.5
25	3.5	10.93
35	9	8.78
45	28	7.5
55	40	7.1
60	44.5	6.88

Thus, it may be concluded that although the energy transfer rates may be considered to analyze the potential of the landslide, however, they cannot always reflect the risk investigation of these landslide.

In **Case-C4**, effects of reservoir water depth on wave formation are investigated. If the initial water depth was increased by keeping the bed elevation constant, the water surface elevations would differ for each case; hence, it would be misleading for comparisons. Therefore, initial water depth is set by moving the channel bed down for a fixed water surface elevation.

Kinetic and Potential Energy Transfer Ratios with respect to the time are illustrated in Figures 5.13/a and 5.13/b. The numerical simulations with 25, 30 and 40 meters of the initial water depths do not show any decline in the energy transfer ratios within 20 seconds. It may be due that the landslide still affects the wave propagations, such as by forming the second or third waves. For example, an abrupt jump of the numerical simulation with 40 meters of the initial water depth on 15th seconds states that the second wave is created. However, the first wave with the biggest damage potential threatens the dam body. Therefore, whether they demonstrate the decline in graphs or not have no significant contributions on general comparison of the initial water depths when the first wave is in consideration.

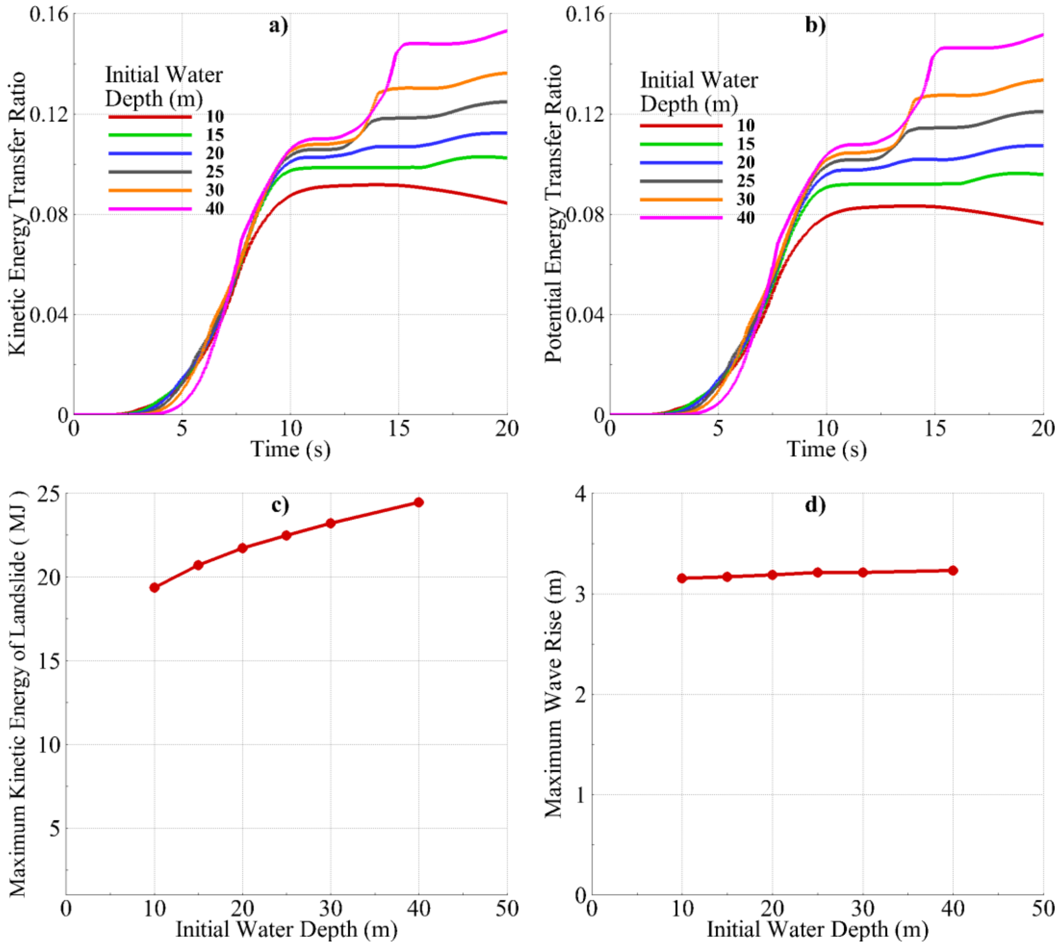

Figure 5.13: For Case-C4; a) KETR vs. Time, b) PETR vs. Time, c) Maximum Kinetic Energy of Landslide vs. Initial Water Depth and d) Maximum Wave Rise vs. Initial Water Depth

When the initial water depth is increased, the energy transfer ratios increase. However, the range of peak energy transfer ratios is considerably small and it may be concluded that the effects of the initial water depth can be neglected. Here, the peak energy transfer ratios refer to the energy transfer ratios in which the first wave is observed. As it is mentioned before, the abrupt jumps determine the second or multiple waves; therefore, they cannot be specifically considered as the peak energy transfer ratios. Insomuch that, the reason to observe the range of the peak energy transfer ratios may be the slide volume variations too. Particularly, as shown in Figure 5.13/c, while the volume of the slide is increased, the maximum kinetic energy of the landslide increases due to an increment in the landslide mass. This result may vary the energy transfer ratios. Lastly, as illustrated in Figure 5.13/d, the initial water depth has no significant impacts on the maximum wave rise and the maximum wave rise is around 3.2 meters.

In **Case-C5 & Case-C6**, the two series of the numerical experiments are performed to consider the effects of internal friction angle of soil and friction angle of bed to the waves, respectively. In Case-C5, maximum roughness is achieved. The maximum roughness occurs when the internal friction angle of the soil equals to the friction angle of the bed. It means that the bed material is the same as the slide material.

The internal friction angle of soil in Case-C5 is varied as 25^o, 30^o, 35^o, 40^o and 45^o. This range is appropriate to simulate the materials of the landslide from loose to dense. KETR and PETR for Case-C5 are shown in Figure 5.14/a and 5.14/b. It is revealed that decrease in the internal friction angle of the soil causes rising in the energy transfer ratios. Thus, more fluidic landslide results in more energy transfer to the dam reservoir.

Furthermore, Figure 5.14/c & d demonstrate KETR and PETR for Case-C6. Actually, Case-C6 is much related to the bed friction. The roughness of the bed is affected by varying the friction angle of bed.

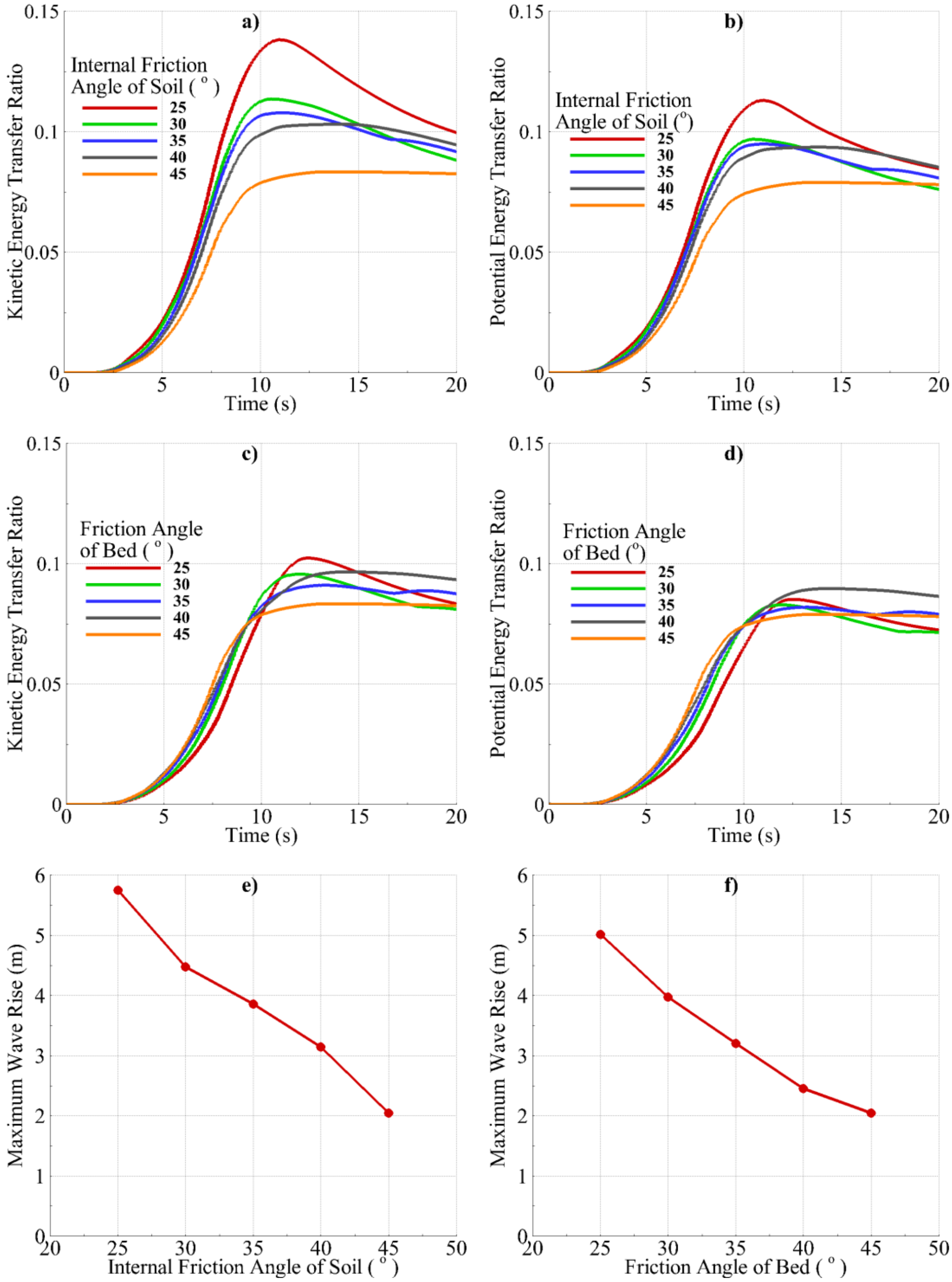

Figure 5.14: a) KETR vs. Time for Case-C5, b) PETR vs. Time for Case-C5, c) KETR vs. Time for Case-C6, d) PETR vs. Time for Case-C6, e) Maximum Wave Rise vs. Internal Friction Angle of Soil for Case-C5 and f) Maximum Wave Rise vs. Friction Angle of Bed for Case-C6

As was shown in equation 3.28, the bed shear stress is related to tangent of the friction angle of the bed affecting the source term. In the case of the energy transfer ratios, there are no significant changes. When the bed gets smoother, the energy transfer ratios increase slightly.

Finally, maximum wave rises for Cases-C5 & C6 are shown in Figure 5.14/e and 5.14/f, respectively and also, Table 5.13 addresses the point of maximum wave crest and required time for them. It is proved with Case-C5 that when the fluidic characteristic of the landslide is increased, the landslide forms higher wave around longer area. Besides, when the bed gets smoother as in Case-C6, it allows to the landslide moving fast and forming higher maximum wave crest with longer span.

Table 5.13: Point and Time of Maximum Wave Rise for Cases-C5 & C6 of Test Case C

Point of Maximum Wave Rise (m) for Case-C5	**Time Required for Maximum Wave Rise (s) for Case-C5**	**Point of Maximum Wave Rise (m) for Case-C6**	**Time Required for Maximum Wave Rise (s) for Case-C6**
46	7.54	66	8.11
38	7.34	51	7.73
30	6.88	39.5	7.65
27	7.45	24.5	6.64
20	7.53	20	7.53

Case-C7

In this series of numerical experiments, the effects of fluidization parameter are investigated and the results for the energy transfer ratios and maximum wave rise are presented in Figure 5.15. The fluidization parameters are set to values of 0.1, 0.3, 0.5, 0.7 and 0.8. When the fluidization parameter approaches to 1, the slide material exhibits more fluidic characteristics. Similar to Case-C5, fluidization of the landslide has considerable effects on the increase of both KETR and PETR as shown in Figure 5.15/a & b. As it was observed before, the potential energy transfer ratio is similar to kinetic energy transfer ratio.

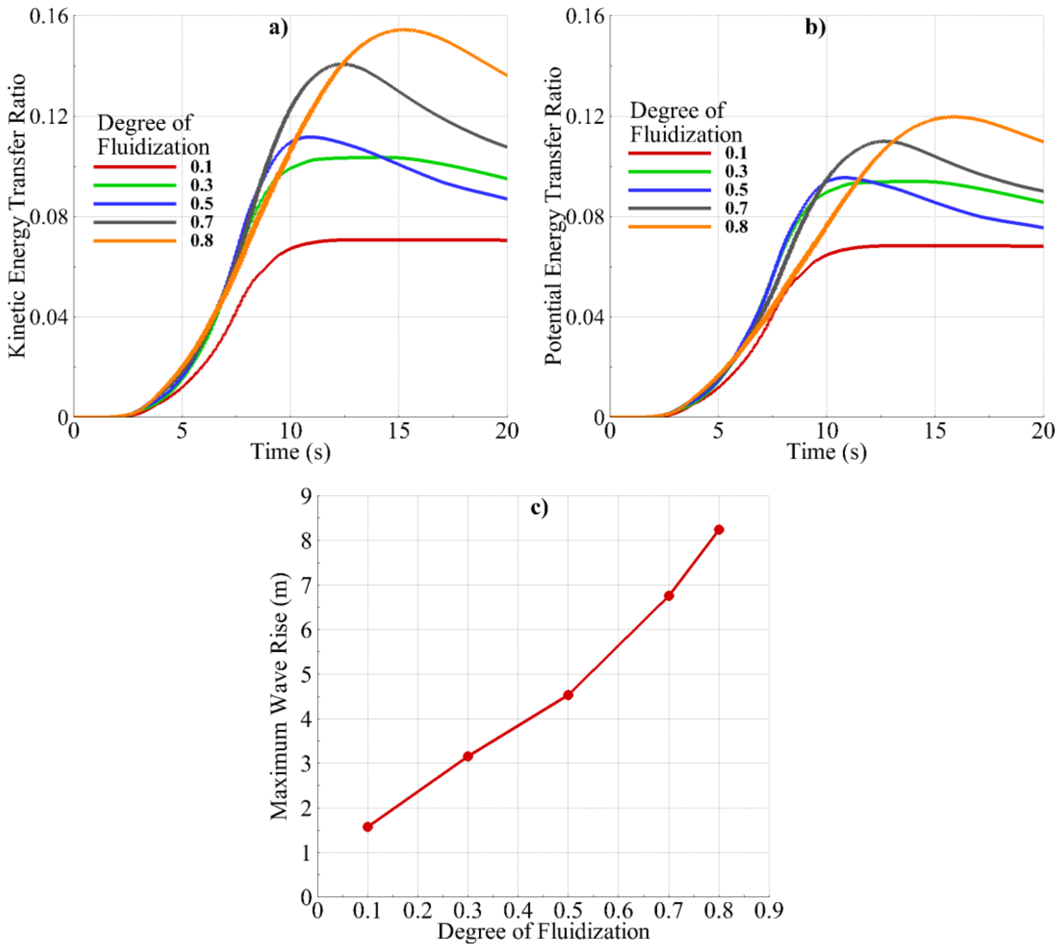

Figure 5.15: For Case-C7; a) KETR vs. Time, b) PETR vs. Time and c) Maximum Wave Rise vs. Degree of Fluidization

Besides, maximum wave rise increases almost linearly with fluidization as depicted in Figure 5.15/c. As can be seen in Table 5.14, the increase in degree of fluidization results in the landslide to penetrate longer distances in the reservoir. As the landslide moves in longer distance with the degree of fluidization, it takes more time to accumulate.

Table 5.14: Point and Time of Maximum Wave Rise for Case-C7 of Test Case C

Degree of Fluidization	Point of Maximum Wave Rise (m)	Time Required for Maximum Wave Rise (s)
0.1	19	7.6
0.3	32	7.46
0.5	46.5	7.54
0.7	68.5	7.97
0.8	75	8.02

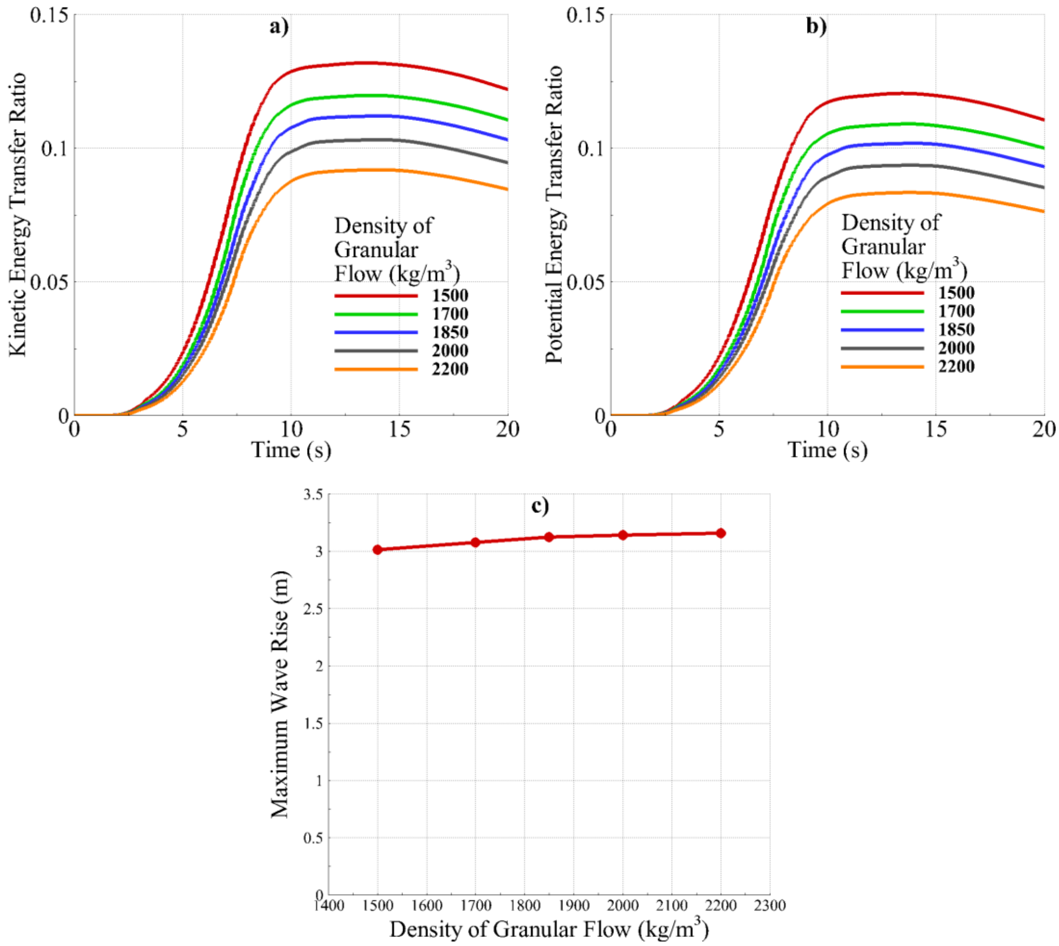

Figure 5.16: For Case-C8; a) KETR vs. Time, b) PETR vs. Time and c) Maximum Wave Rise vs. Density of Granular Flow

In **Case-C8**, effect of density of the granular flow on wave generation are investigated. Density is varied as 1500, 1700, 1850, 2000 and 2200 kg/m^3. As shown in Figure 5.16/a & b, the energy transfer ratios decrease as the density of the granular flow is increased. One way to explain this mathematically is the coefficient of the pressure force term due to the water, ρ/ρ_g, in Equation 3.29. This is the only term that the density can have an impact on the granular flow. A decrease in this coefficient means that the pressure exerted on the landslide by water decreases; hence, the landslide moves faster. Therefore, rising in the divisor of Equation 3.30 and 3.31, due to the increase in the velocity of the landslide, leads to the decrease in the KETR and PETR. However, this may not affect the maximum wave crest significantly as shown in Figure 5.16/c where the maximum wave rise for all densities are almost the same, around 3 meters.

In **Case-C9**, effect of Manning's roughness for the reservoir bed on wave generation is investigated with the series of the numerical experiments. Results of energy transfer ratios and maximum wave rise are for the Manning's n values of 0.03, 0.07, 0.11 and 0.15 are shown in Figure 5.17. The Manning's roughness parameter may be more effective when waves propagate over long distances. When the Manning's parameter is increased, the energy transfer ratios decrease because waves lose their energy more due to bed dissipation. This expectation is supported by Figure 5.17/a & b. Significant changes in energy transfer occurred depending on the Manning's parameter when the waves propagate towards the dam face. There is no effect of Manning's n on the maximum wave crest (Figure 5.17/c).

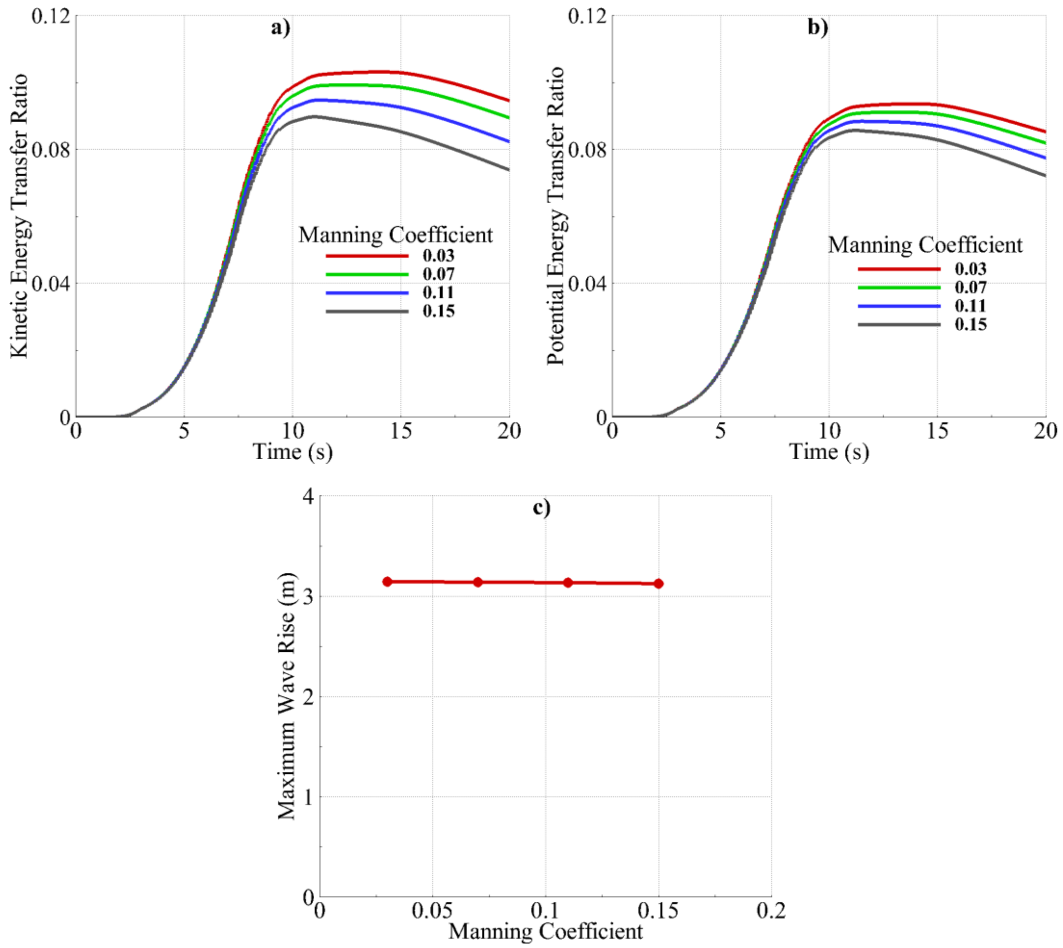

Figure 5.17: For Case-C9; a) KETR vs. Time, b) PETR vs. Time and c) Maximum Wave Rise vs. Manning Coefficient

Summary of observations for Test Case C:

a) Energy transfer rate increases with increasing slide thickness.

b) Energy transfer rate decreases with increasing slide length.

c) Maximum wave rise increases with both slide thickness and length, slide length causes slightly higher wave rise.

d) Energy transfer rate increase with slide angle up to 45^0, then decrease for higher slide angles.

e) Wave rise continually increases with slide angle.

f) Wave rise is independent of water depth in the reservoir.

g) Energy transfer rate increases with water depth as simulation time increases.

h) Increasing internal friction angle of the slide decreases the energy transfer rate while friction angle of the bed has negligible effect on energy transfer.
i) Maximum wave rise decreases with increasing internal friction angle of the slide and bed friction angle.
j) Energy transfer ratio increases with degree of fluidization.
k) Maximum wave rise increases with degree of fluidization.
l) Increasing density of the slide material decreases energy transfer ratio.
m) Maximum wave rise is independent of density of the slide.
n) Increasing Manning parameter decreases energy transfer ratio.
o) Maximum wave rise is independent of Manning parameter.

5.4 Test Cases D

So far, partially subaerial translational landslides were tested. This section is devoted to circular landslides under subaerial and submarine conditions. Basically, if the entire landslide material is exposed to atmosphere, it is called the subaerial landslide. Otherwise, when the landslide material is entirely contained in hydrostatic water, it is called as submarine landslide.

For both subaerial and submarine conditions, the numerical simulation parameters are set as: 20 s run time, 0.01 seconds time step, 0.5 m the mesh size and 0.9 for the CFL number. The far-field condition is applied on the dam side. However, the numerical stability problems observed when the slide radius is increased in Cases-D11 & D12. Therefore, only for these cases, the mesh size is refined to 0.25 meters.

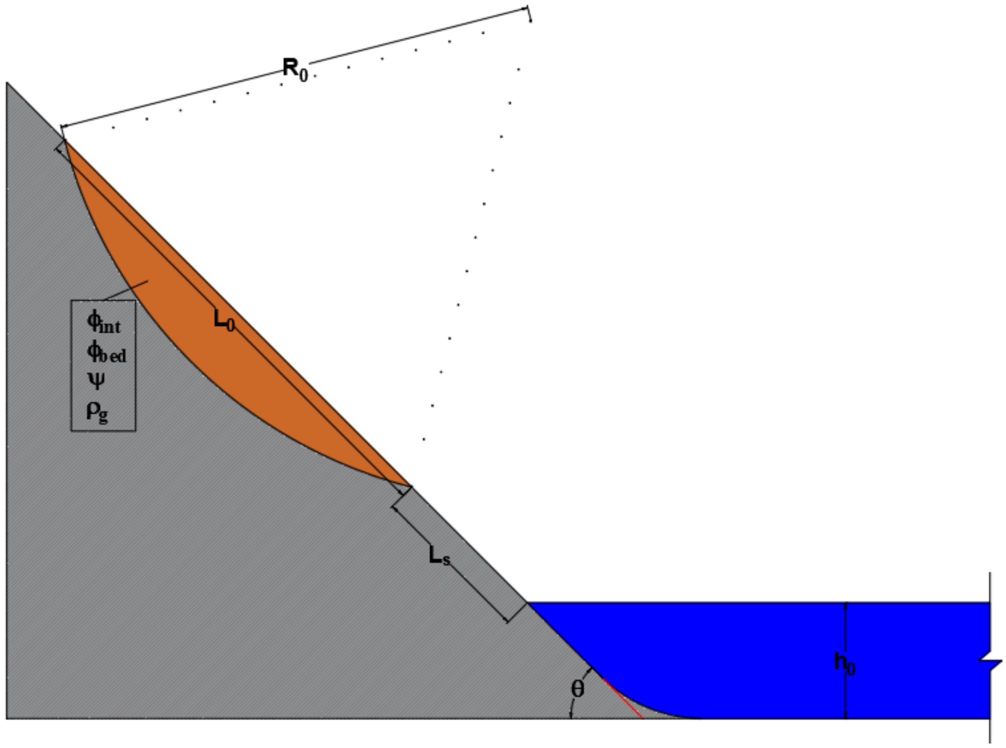

Figure 5.18: Assumed Test Geometry for the Two-Layer Subaerial Circular Landslide Model

Description of landslide geometry and related parameters to be studied are shown in Figure 5.18. Slide material properties are internal friction angle of the soil ($\emptyset_{int}$), friction angle of the bed ($\emptyset_{bed}$), degree of fluidization (ψ) and density of the landslide (ρ_g). Environmental variables are initial water depth (h_0), the Manning's roughness (n), the slide angle (θ), the radius of curvature of the failure plane (R_0), the slide length (L_0) and the runaway distance of the slide (L_s). The runaway distance is the distance between the toe of the slide mass and water level. The range of variables tested in this group of numerical experiments for the subaerial conditions are given in Table 5.15.

Table 5.15: Definition of Variables Range for Subaerial Part of Test Cases D

Cases	Volume of Slide (m^3)	Radius of Curvature (m)	Length of Slide (m)	Runaway Distance (m)	Slide Angle (º)	Initial Water Depth (m)	Internal Friction Angle of Soil (º)	Friction Angle of Bed (º)	Degree of Fluidization	Density of Granular Flow (kg/m^3)	Manning Coefficient
D1	125.52-166.83-208.99-252.18	53.34-41.62-34.76-30.37	42.43	0	45	10	40	40	0.3	2000	0.03
D2	125.84-166.83-207.88-251.54	41.82-41.62-41.20-41.42	38.89-42.43-45.25-48.08	0	45	10	40	40	0.3	2000	0.03
D3	166.83	41.62	42.43	0-14.14-35.36-70.71-141.42	45	10	40	40	0.3	2000	0.03
D4	165.87-165.91-165.66-166.83-164.68-166.29	122.81-58.61-41.05-41.62-40.55-43.36	62.12-48-42.12-42.43-41.84.43	0	15-25-35-45-55-60	10	40	40	0.3	2000	0.03
D5	166.83	41.62	42.43	0	45	10-15-20-25-30-40	40	40	0.3	2000	0.03
D6	166.83	41.62	42.43	0	45	10	25-30-35-40-45	25-30-35-40-45	0.3	2000	0.03
D7	166.83	41.62	42.43	0	45	10	45	25-30-35-40-45	0.3	2000	0.03
D8	166.83	41.62	42.43	0	45	10	40	40	0.1-0.3-0.5-0.7	2000	0.03
D9	166.83	41.62	42.43	0	45	10	40	40	0.3	1500-1700-1850-2000-2200	0.03
D10	166.83	41.62	42.43	0	45	10	40	40	0.3	2000	0.03-0.07-0.11-0.15

Moreover, as illustrated in Figure 5.19, the initial water depth (h_0), the slide angle (θ), the radius of curvature of the failure plane (R_0) and the slide length (L_0) are investigated in proposed geometry for submarine conditions of Circular Landslide Modelling.

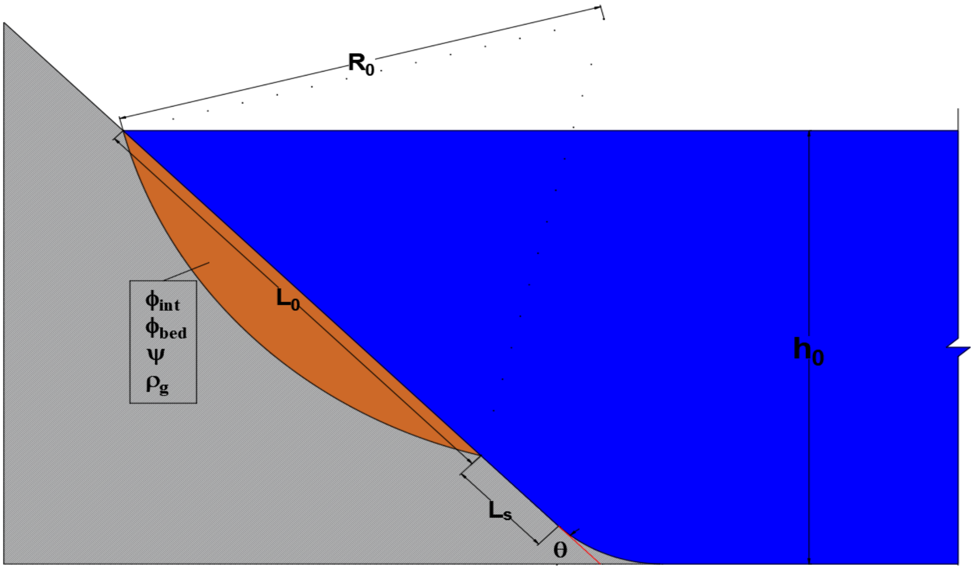

Figure 5.19: Assumed Test Geometry for the Two-Layer Submarine Circular Landslide Model

Besides, the landslide features (the internal friction angle of the soil ($\emptyset_{int}$), the friction angle of the bed ($\emptyset_{bed}$), degree of fluidization (ψ) and the density of the landslide (ρ_g)) are analyzed. Unlike the runaway distance for subaerial conditions, submarine runaway distance (L_s) is used. It is the distance between toe of the slide mass and end of the inclined ramp.

The range of variables tested in this group of numerical experiments for submarine conditions are given in Table 5.16.

Table 5.16: Definition of Variables Range for Submarine Part of Test Cases D

Cases	Volume of Slide (m^3)	Radius of Curvature (m)	Length of Slide (m)	Runaway Distance (m)	Slide Angle (^{o})	Initial Water Depth (m)	Internal Friction Angle of Soil (^{o})	Friction Angle of Bed (^{o})	Degree of Fluidization	Density of Granular Flow (kg/m^3)	Manning Coefficient
D11	125.52-166.83-208.99-252.18	53.34-41.62-34.76-30.37	42.43	7.78	45	40	40	40	0.3	2000	0.03
D12	125.84-166.83-207.88-251.54	41.82-41.62-41.20-41.42	38.89-42.43-45.25-48.08	7.78	45	40	40	40	0.3	2000	0.03
D13	166.83	41.62	42.43	7.78-14.14-21.21-35.36	45	40	40	40	0.3	2000	0.03
D14	165.87-165.91-165.66-166.83-164.68-166.29	122.81-58.61-41.05-41.62-40.55-42.14	62.12-48-42.12-42.43-41.84-42	7.78	15-25-35-45-55-60	40	40	40	0.3	2000	0.03
D15	166.83	41.62	42.43	7.78	45	40-45-50-60	40	40	0.3	2000	0.03
D16	166.83	41.62	42.43	7.78	45	40	25-30-35-40-45	25-30-35-40-45	0.3	2000	0.03
D17	166.83	41.62	42.43	7.78	45	40	45	25-30-35-40-45	0.3	2000	0.03
D18	166.83	41.62	42.43	7.78	45	40	40	40	0.1-0.3-0.5-0.7-0.8	2000	0.03
D19	166.83	41.62	42.43	7.78	45	40	40	40	0.3	1500-1700-1850-2000-2200	0.03
D20	166.83	41.62	42.43	7.78	45	40	40	40	0.3	2000	0.03-0.07-0.11-0.24

Cases-D1 & D2 are performed to study the effects of slide volume on wave generation. Slide volume can be varied by changing slide radius (Case-D1) or slide length (Case-D2). The range of variables for both cases are illustrated in Table 5.15.

Figures 5.20/a & b indicate KETR and PETR of Case-D1 and also, Figures 5.20/c & d demonstrate KETR and PETR of Case-D2. Whereas KETR and PETR increase with the volume of the slide in Case-D1, KETR and PETR of Case-D2 are not affected by the volume of the slide. Despite the similarities between Case-C1 & D1, they contradict in Case-C2 & D2. Besides, rather than a definition of b_0/L_0 as in the Translational Slide Modelling, for subaerial conditions of Circular Slide Modelling, R_0/L_0 can be defined due to its circular geometry. Nevertheless, this parameter is not sufficient to convey the effects of the volume of the slide because it fails in Case-D2.

In fact, Figure 5.20/e may describe why Case-D2 fails with this parameter. As the maximum kinetic energy of the landslide varies exponentially with the velocity of the landslide, a wider range of the volume of the slide and the slide length in Test Cases C causes an increase in the maximum kinetic energy of the landslide. However, the span of the maximum kinetic energy of the landslide is less in Case-D2. Thus, almost equal energy transfer ratios may be observed and therefore, it may be assumed that if the range of the volume of the slide in Case-D2 increases, it would probably validate this relation. Unfortunately, the circular failure line restricts increasing the range of the maximum kinetic energy of the landslide.

Moreover, Figure 5.20/f points out that the maximum wave crest increases when the volume of the slide is increased by either increasing the slide radius (Case-D1) or elongating the slide (Case-D2). There are small differences in the maximum wave rise between Case-D1 and Case-D2. Additionally, based on Table 5.17, wave crests are observed at nearly similar positions and time required for the maximum.

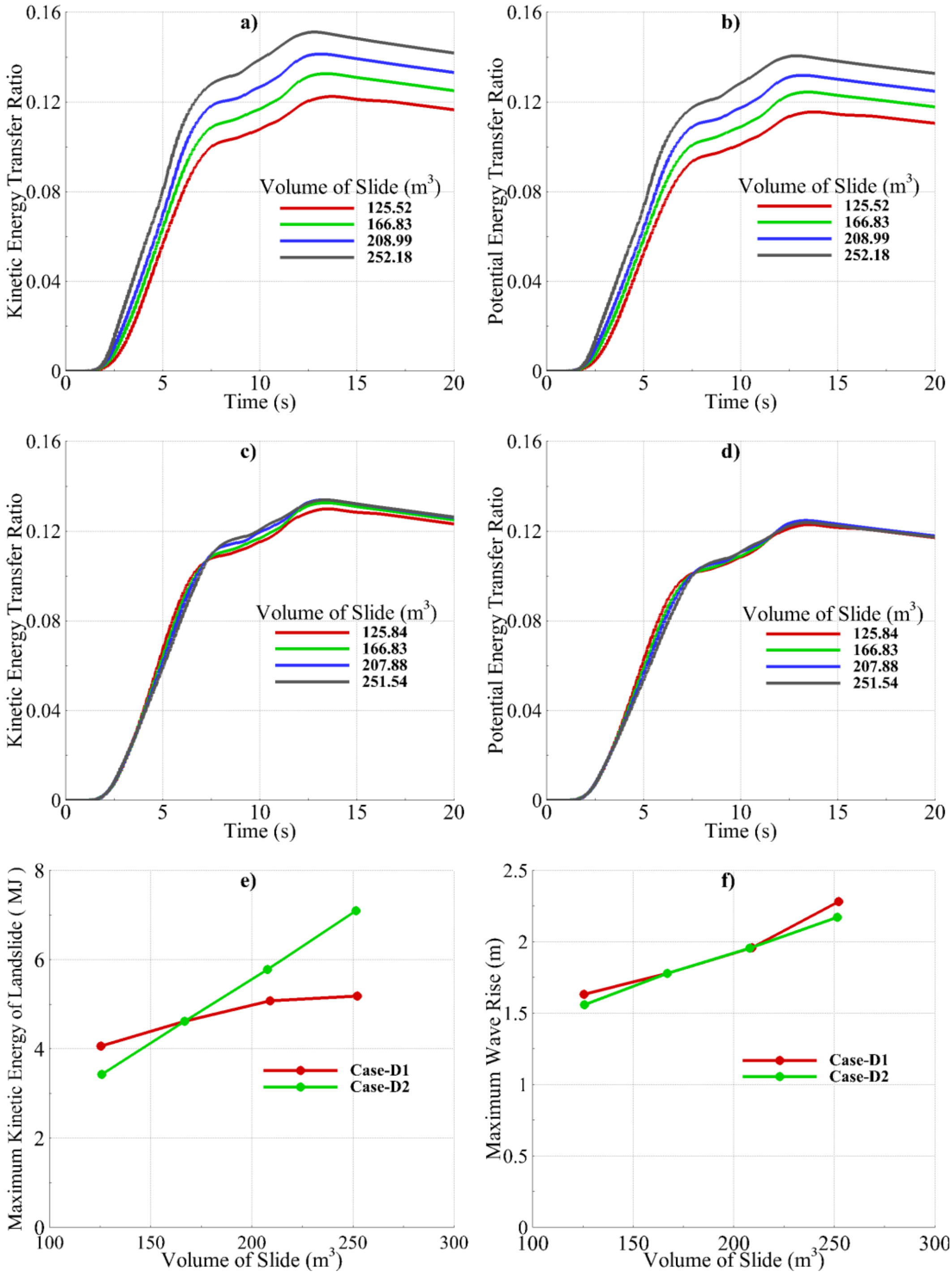

Figure 5.20: a) KETR vs. Time for Case-D1; b) PETR vs. Time for Case-D1; c) KETR vs. Time for Case-D2; d) PETR vs. Time for Case-D2; e) Maximum Kinetic Energy of Landslide vs. Volume of Slide for Cases-D1 & D2 and f) Maximum Wave Rise vs. Volume of Slide for Cases-D1 & D2

Table 5.17: Point and Time of Maximum Wave Rise for Cases- D1 & D2 of Test Cases D

Volume of Slide (m^3)	Point of Maximum Wave Rise for Case-D1 (m)	Time Required for Maximum Wave Rise for Case-D1 (s)	Point of Maximum Wave Rise for Case-D2 (m)	Time Required for Maximum Wave Rise for Case-D2 (s)
125.52	10.5	4.04	10.5	3.89
166.83	10.5	3.68	10.5	3.68
208.99	7	2.71	10	3.36
252.18	7.5	2.53	8.5	2.94

Case-D3 is designed to perform a series of the numerical experiments to test the effects of runaway distance over the dam reservoir. Longer runaway distances allow the landslide to run-out through the dam reservoir which may affect wave formations.

Figure 5.21/a & b demonstrate KETR and PETR, respectively. Firstly, it is noticed that time required for the beginning of the energy transfer between water and landslide are around 2, 3, 6, 8 and 12 seconds, respectively. These values represent the time where the landslide moves over the subaerial part of an inclined bed.

It is observed from the numerical results that the energy transfer ratios decrease by increasing the runaway distance. In fact, a decrease in the energy transfer ratios with the runaway distance can be elucidated with Figure 5.21/c. More specifically, when the runaway distance is extended, the landslide accelerates and hence, the maximum kinetic energy of the landslide increases. Eventually, it leads to a decrease in KETR and PETR.

Besides, Figure 5.21/d indicates that there are no significant changes in the maximum wave rise due to variations of the runaway distance. However, according to Table 5.18, the point and time of the maximum wave are affected by the runaway distance. Longer runaway distance allows the landslide to accelerate more and high-speed slide result in long displacements and therefore, it takes more time for the formation of the maximum wave rise.

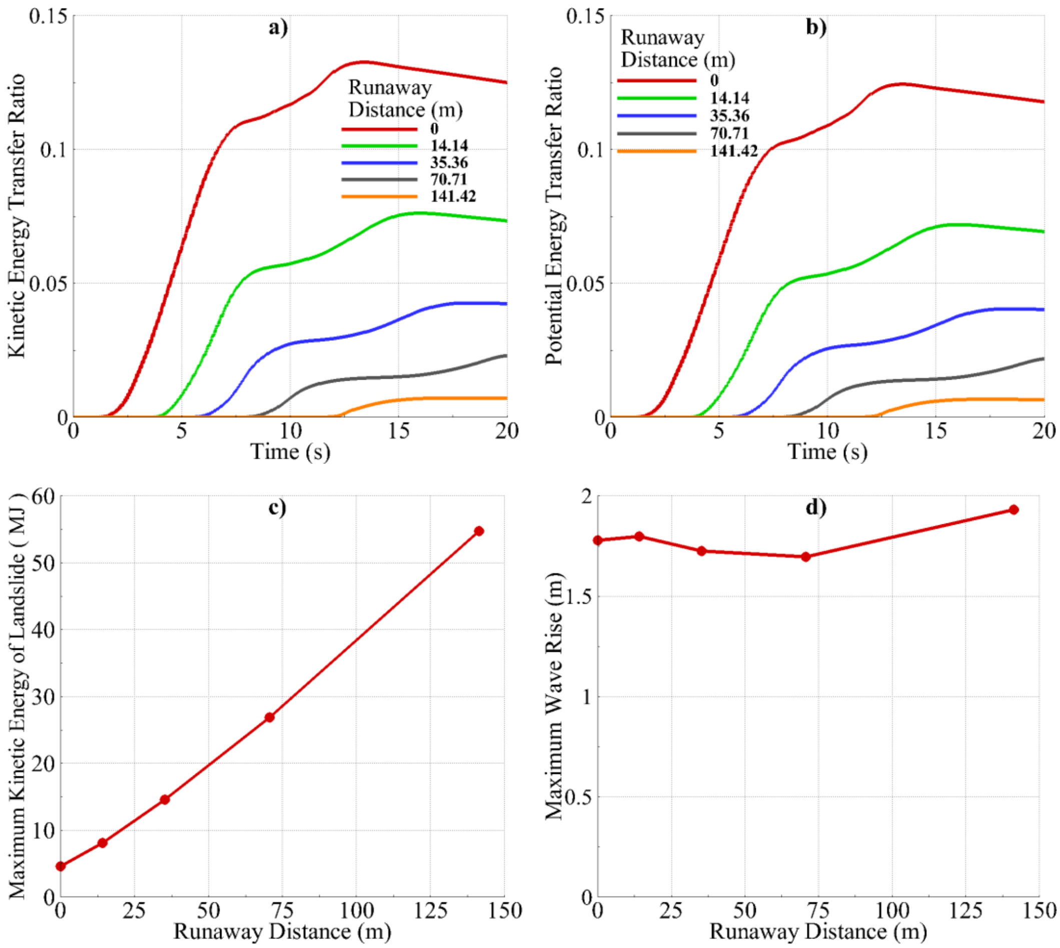

Figure 5.21: For Case-D3; a) KETR vs. Time, b) PETR vs. Time, c) Maximum Kinetic Energy of the Landslide vs. Runaway Distance and d) Maximum Wave Rise vs. Runaway Distance

Table 5.18: Point and Time of Maximum Wave Rise for Case-D3 of Test Cases D

Runaway Distance (m)	Point of Maximum Wave Rise (m)	Time Required for Maximum Wave Rise (s)
0	10.5	3.68
14.14	20.5	6.63
35.36	25.5	7.94
70.71	35.5	9.89
141.42	51	12.63

In **Case-D4**, slide angles are varied from 15° to 60° in the series of the numerical simulations and results are shown in Figure 5.22. The first two figures (a and b) show KETR and PETR with respect to time. It is observed from the numerical simulation with the slide angle of 15° that these landslides are negligibly small movements. In fact, the reason to observe the landslide motion in the numerical simulation with the slide angles of 25° is about the subaerial condition of Circular Landslide Modelling. Because contrary to the partially subaerial condition of Test Cases C, there is no hydrostatic pressure over the landslide in Test Cases D.

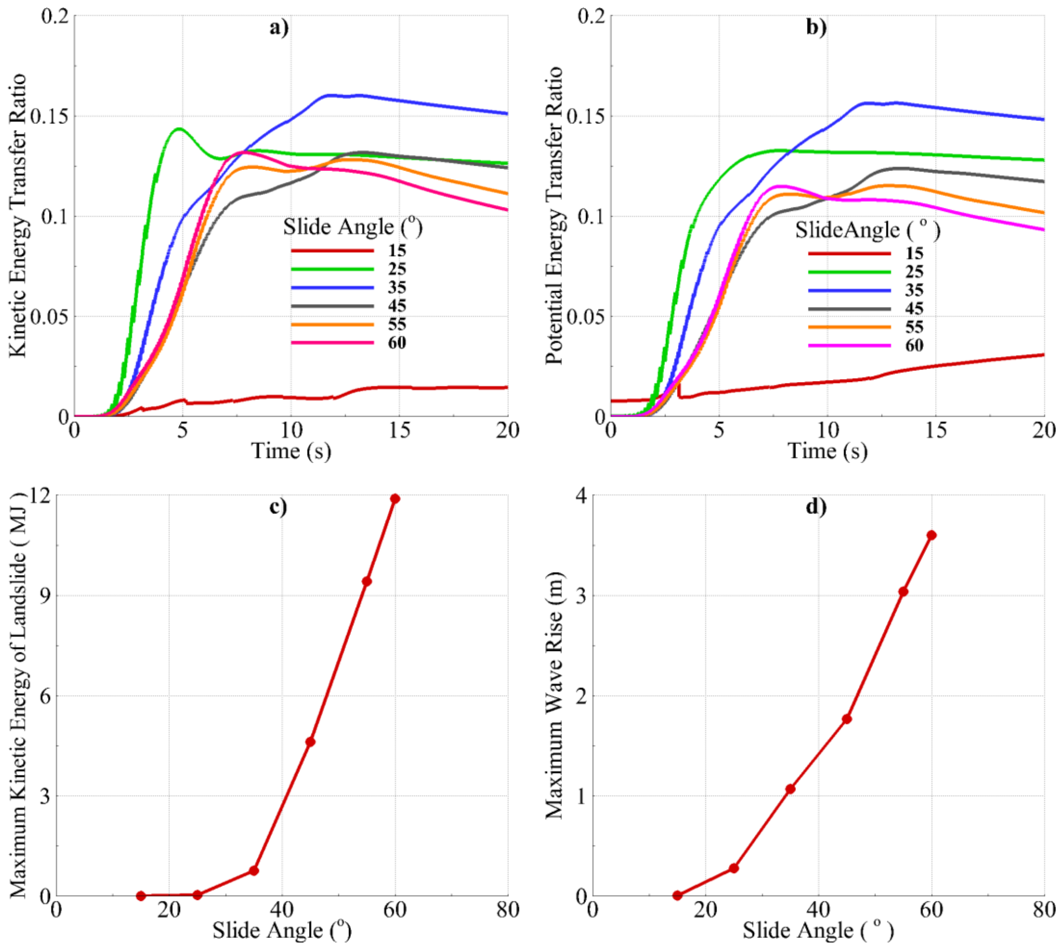

Figure 5.22: For Case-D4; a) KETR vs. Time, b) PETR vs. Time, c) Maximum Kinetic Energy of the Landslide vs. Slide Angle and d) Maximum Wave Rise vs. Slide Angle

Peak KETR and PETR increase when the slide angles are increased up to a certain point and after the slide angle of 35^o, KETR and PETR tend to decrease. Here, the subaerial condition makes the landslide vulnerable to run-out and therefore, maximum energy transfer ratios are formed with less slide angle as compared to Case-C3.

According to Figure 5.22/c, the maximum kinetic energy of the landslide increases with a steeper angle. It validates the idea in Translational Landslide Modelling stating that the wave energies become an important consideration for the energy transfer ratios because the maximum kinetic energy of the landslide and the energy transfer ratios contradict an inverse relationship. Moreover, Figure 5.22/f shows that the higher maximum wave crest occurs when the slide angle gets steeper. Here, it is observed that the maximum wave rise is slightly higher than expected at the numerical simulation with a slide angle of 35^o. Therefore, this simulation has more potential to make higher waves. This situation may remark the effects of the wave energies on the maximum wave rise. In addition, Table 5.19 indicates that due to an increase in the maximum kinetic energy of the landslide, the landslide runout goes further with lesser time.

Table 5.19: Point and Time of Maximum Wave Rise for Case-D4 of Test Cases D

Slide Angle (^{o})	Point of Maximum Wave Rise (m)	Time Required for Maximum Wave Rise (s)
15	5.5	18.64
25	5.5	5.07
35	5.5	3.55
45	10.5	3.66
55	25.5	5.39
60	28.5	5.2

Case-D5 investigates the initial water depth as illustrated in Figure 5.23. KETR and PETR are illustrated in Figure 5.23/a & b. Deep water leads to a rise in the energy transfer ratios but there are relatively minor variations observed in these dimensionless parameters. One fact should be noted that the second peak in the scenario with 10 meters of the initial water depth does not reflect the energy transferred by the first wave.

In fact, inclined ramp elongates with the water depth. This means that the landslide runouts more in the inclined ramp; therefore, the maximum kinetic energy of the landslide increases with the initial water depth as illustrated in Figure 5.23/c. However, there are small variations in the maximum kinetic energy of the landslide. Moreover, Figure 5.23/d shows that the initial water depth does not affect significantly the maximum wave rise and it is almost constant around 1.7 meters.

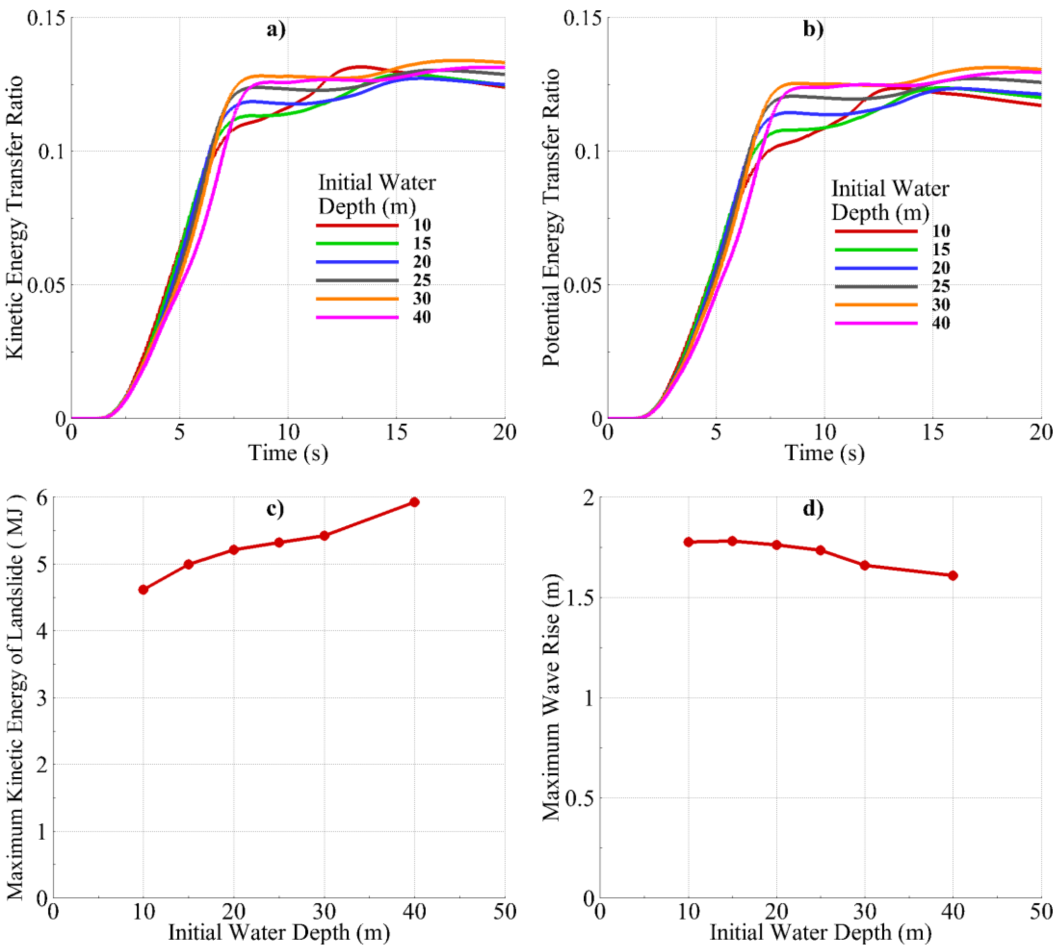

Figure 5.23: For Case-D5; a) KETR vs. Time, b) PETR vs. Time, c) Maximum Kinetic Energy of the Landslide vs. Initial Water Depth and d) Maximum Wave Rise vs. Initial Water Depth

Case-D6 & Case-D7 are designed to study the internal friction angle of soil and friction angle of bed, respectively. Maximum roughness occurs when the internal friction angle of the soil equals to the friction angle of the bed. In Case-D6, the maximum roughness is obtained. On the contrary, Case-D7 uses variable bed friction.

Figure 5.24/a & b show KETR and PETR for Case-D6. Particularly, the energy transfer ratios decrease with an increase in the internal friction angle of the soil. In fact, this situation recalls that fluidic characteristics of the landslide exert great influence on the energy transfer. Figure 5.24/c & d demonstrate KETR and PETR for Case-D7. It is observed that for decreasing bed roughness energy transfer ratios slightly increase.

Moreover, the maximum wave rises for Case-D6 and Case-D7 are considered with Figures 5.24/e and 5.24/f, respectively. Also, Table 5.20 shows the point and required time of maximum wave rise for Case-D6 and Case-D7. Here, Case-D6 proves that increasing the fluidic properties of the landslide allow the landslide to form higher wave crest and spread larger distances. Besides, smoother bed facilitates movement of the landslide over longer distances with higher maximum wave rise. In addition, decreasing these parameters results in the longer distance to runout; therefore, it takes more time.

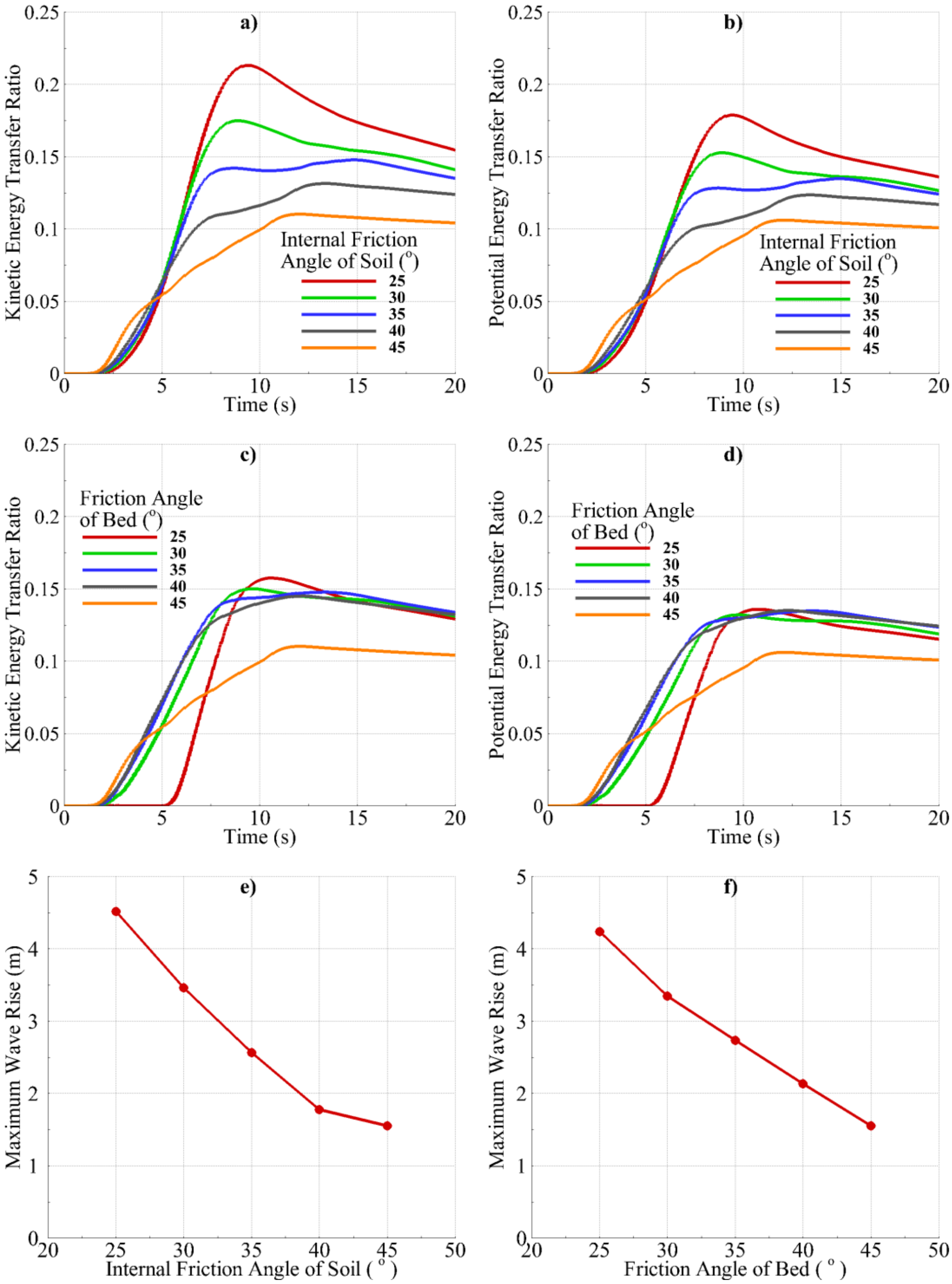

Figure 5.24: a) KETR vs. Time for Case-D6, b) PETR vs. Time for Case-D6, c) KETR vs. Time for Case-D7, d) PETR vs. Time for Case-D7, e) Maximum Wave Rise vs. Internal Friction Angle of Soil for Case-D6 and f) Maximum Wave Rise vs. Friction Angle of Bed for Case-D7

Table 5.20: Point and Time of Maximum Wave Rise for Case-D6 and Case-D7 of Test Cases D

Point of Maximum Wave Rise (m) for Case-D6	Time Required for Maximum Wave Rise (s) for Case-D6	Point of Maximum Wave Rise (m) for Case-D7	Time Required for Maximum Wave Rise (s) for Case-D7
36	6.12	52.5	6.19
28.5	5.9	21	4.01
22	5.61	11.5	3.33
10.5	3.67	12.5	3.87
5.5	2.62	5.5	2.62

Case-D8 studies the degree of fluidization and results are presented in Figure 5.25. So far, it is already stated that if the slide material exhibits more fluidic behavior, it causes higher KETR and PETR and maximum wave crest. In addition, landslide can propagate long distances along the bed. As the fluid characteristics of the landslide are increased with increasing the degree of fluidization, the energy transfer ratios (Figures 5.25/a & b) and the maximum wave rises (Figure 5.25/c) increase also.

Moreover, Table 5.21 defines the place and required time for maximum wave rise. It supports the idea that when the fluidic behavior of the landslide is increased by decreasing the degree of fluidization, it gives an opportunity for the landslide to run more out in the reservoir, but it also takes longer time to run out over long distances.

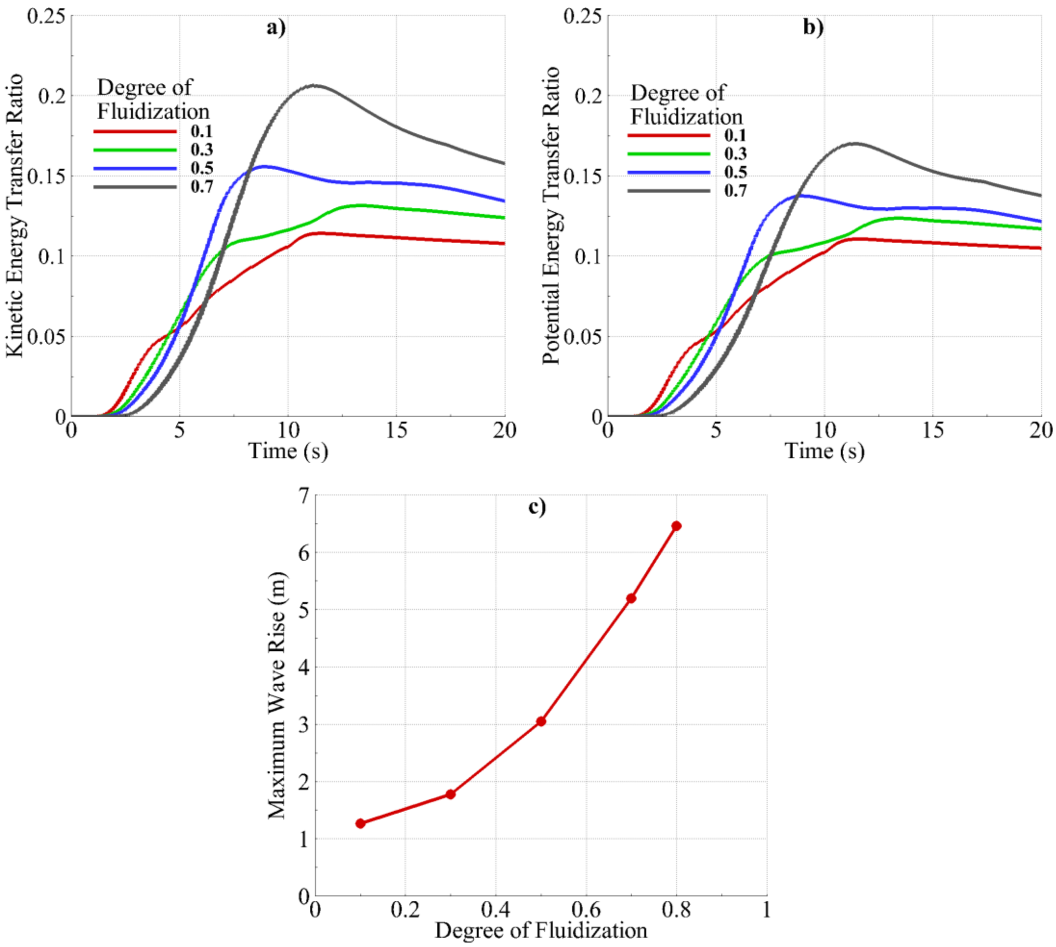

Figure 5.25: For Case-D8; a) KETR vs. Time, b) PETR vs. Time and c) Maximum Wave Rise vs. Degree of Fluidization

Table 5.21: Point and Time of Maximum Wave Rise for Case-D8 of Test Cases D

Degree of Fluidization	Point of Maximum Wave Rise (m)	Time Required for Maximum Wave Rise (s)
0.1	5.5	2.8
0.3	10.5	3.67
0.5	29	5.78
0.7	52.5	6.69
0.8	69.5	7.21

In **Case-D9**, a series of numerical simulations are performed to investigate the effects of the density of the granular flow. In fact, the effects of density of the granular flow on the wave propagations in Test Cases C are still valid, because this observation is independent from failure plane changes. As shown in Figure 5.26/a & b, when the slide material becomes denser, KETR and PETR tend to decrease. The kinetic energy of the landslide increases due to fast landslide speed as illustrated in Figure 5.26/c because the stresses over the denser landslide due to the hydrostatic pressure of the water are relatively small. As the maximum kinetic energy of the landslide increases, KETR and PETR decrease.

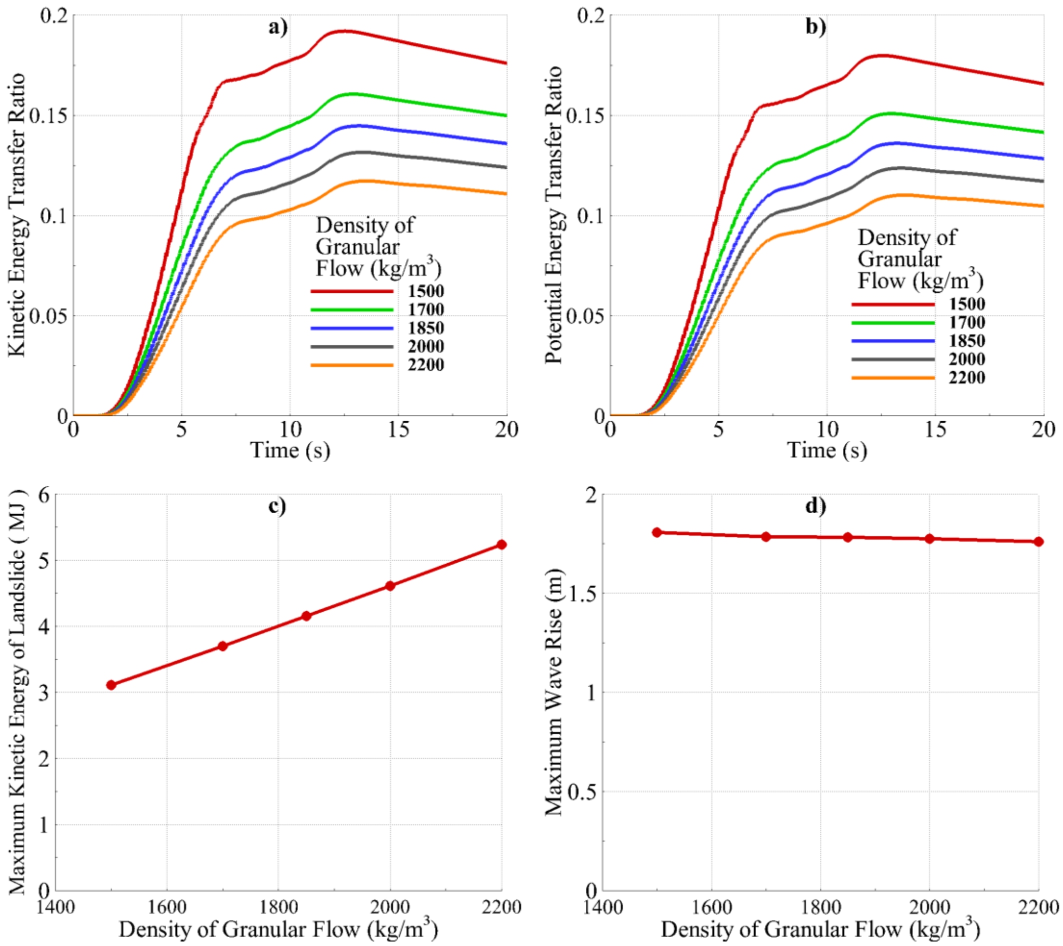

Figure 5.26: For Case-D9; a) KETR vs. Time, b) PETR vs. Time, c) Maximum Kinetic Energy of the Landslide vs. Density of Granular Flow and d) Maximum Wave Rise vs. Density of Granular Flow

The density of the granular flow does not affect the maximum wave rises. Figure 5.26/d demonstrates that the maximum wave rise is almost 1.78 meters for all cases.

Besides, as illustrated in Table 5.22, the point and required time for the maximum wave rise are almost similar for each density of the granular flow.

Table 5.22: Point and Time of Maximum Wave Rise for Case-D9 of Test Cases D

Density of Granular Flow (kg/m^3)	Point of Maximum Wave Rise (m)	Time Required for Maximum Wave Rise (s)
1500	10	3.98
1700	9	3.53
1850	10	3.64
2000	10.5	3.67
2200	11.5	3.75

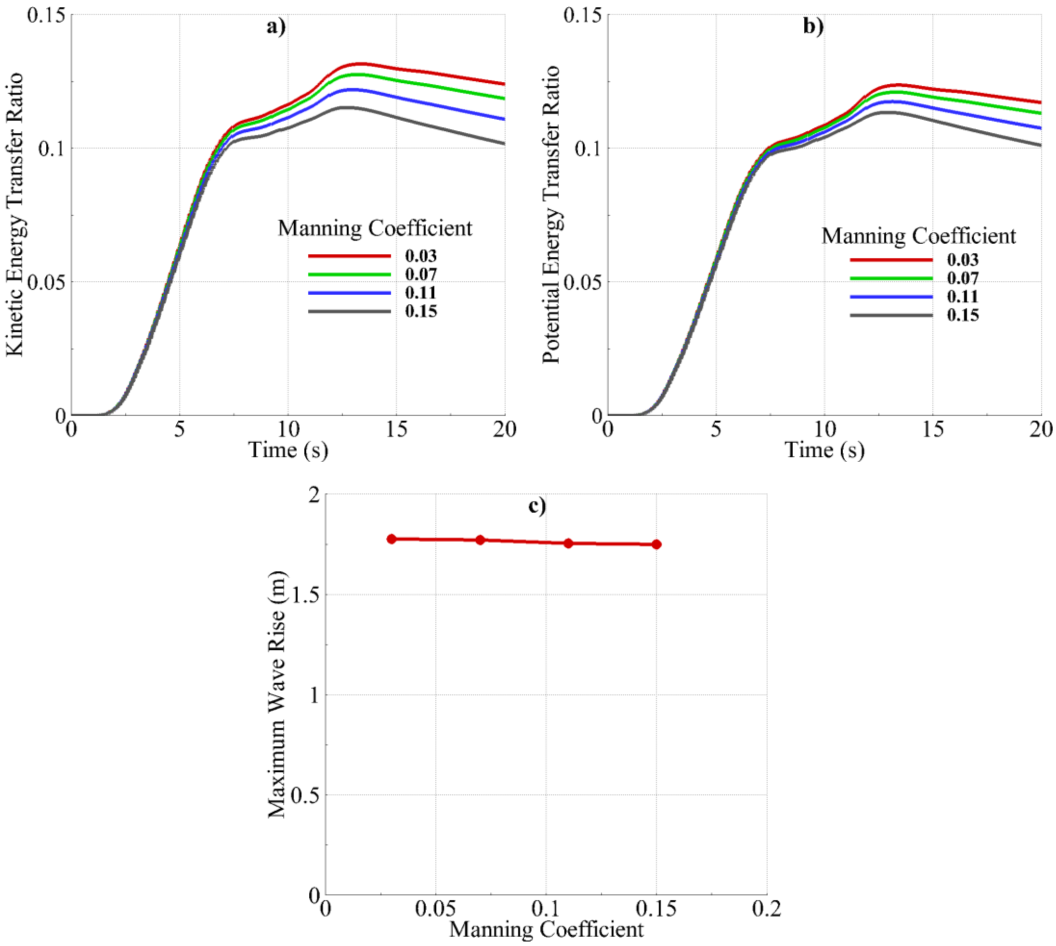

Figure 5.27: For Case-D10; a) KETR vs. Time, b) PETR vs. Time and c) Maximum Wave Rise vs. Manning Coefficient

Case-D10: in this series of numerical experiments, effects of Manning's roughness for the reservoir bed on wave generation is investigated. Results of the energy transfer ratios and maximum wave crest for the Manning's n values of 0.03, 0.07, 0.11 and 0.15 are presented in Figure 5.27. The Manning's roughness parameter may be more effective when waves propagate over long distances. When the Manning's parameter is increased, the energy transfer ratios decrease because waves lose their energy more due to bed friction. This expectation is supported by Figure 5.27/a & b. Significant changes in energy transfer occurred depending on the Manning's parameter when the waves propagate towards the dam face. There is no effect of Manning's n on wave run-up (Figure 5.27/c).

Summary of observations for subaerial landslide:

a) Kinetic energy transfer ratio increases with radius of slide as the slide volume is increased.
b) Kinetic energy transfer ratio is independent of slide length even though the slide volume is increased.
c) Maximum wave rise is independent of increase in slide volume for both cases due to increase in radius or increase in length.
d) Energy transfer ratio decreases with the runaway distance.
e) Maximum wave rise is almost independent of runaway distance.
f) Energy transfer ratio is negligible for slide angles less than 20^0, increases up to slide angle of 35^0 and then decreases again.
g) There is strong increase in maximum wave rise when the slide angle increases.
h) Water depth in the reservoir is insignificant in energy transfer and wave rise.
i) Increase in internal friction angle of the slide causes a decrease in energy transfer ratio.
j) Bed friction has less control on the energy transfer rates.
k) Increase in both internal friction angle and bed friction results in decrease wave rise.

l) Energy transfer ratio increases with degree of fluidization.
m) Maximum wave rise increases with degree of fluidization.
n) Energy transfer ratio decreases with increase slide density.
o) Maximum wave rise is independent of slide density.
p) Energy transfer ratio decrease with increase in Manning's parameter.
q) Maximum wave rise is independent of Manning's parameter.

Cases-D11 & D12 are introduced to analyze the effects of volume of slide to the wave generation by varying the slide radius (Case-D11) or the slide length (Case-D12). In order to investigate the differences between subaerial and submarine conditions for the landslide, same series of the numerical experiments are proposed (Table 5.16). Results are demonstrated in Figure 5.28. First two figures show that the energy transfer ratios are similar to the subaerial conditions of Test Case D. Particularly, KETR and PETR rise when the slide volume is increased by changing the slide radius.

However, as shown in Figures 5.28/c & d, the energy transfer ratios for Case-D12 behave differently when compared to Case-D2. Essentially, when the slide volume is varied by increasing the slide length, the energy transfer ratios are prone to increase. In fact, subaerial and submarine conditions have their own mechanisms, because they differ on the splashing zone. Therefore, similar outcomes should not be expected.

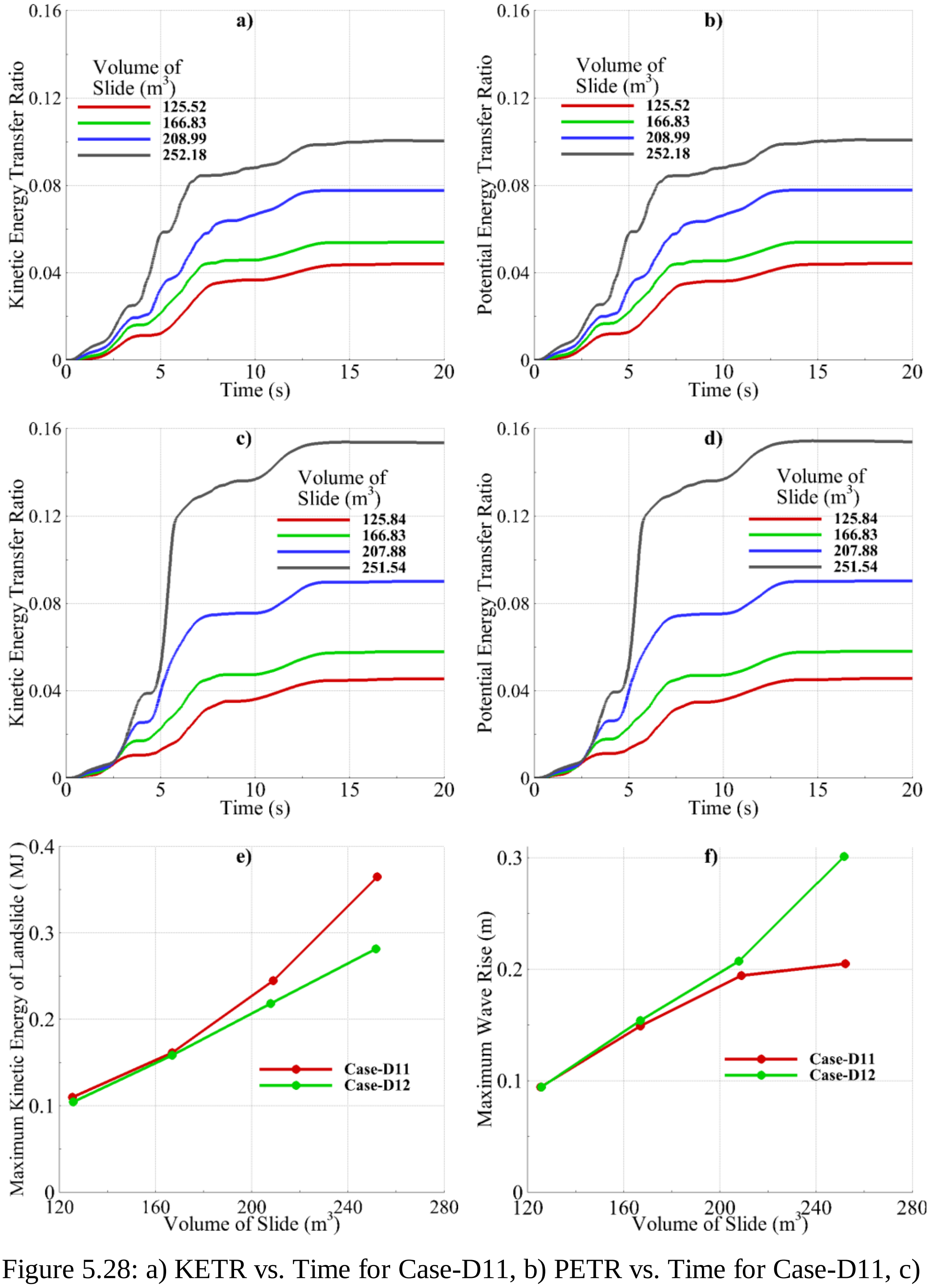

Figure 5.28: a) KETR vs. Time for Case-D11, b) PETR vs. Time for Case-D11, c) KETR vs. Time for Case-D12, d) PETR vs. Time for Case-D12, e) Maximum Kinetic Energy of the Landslide vs. Volume of Slide for Cases-D11 & D12 and f) Maximum Wave Rise vs. Volume of Slide for Cases-D11 & D12

Another consideration is that the slide length has more potential to transfer energy to the dam reservoirs compared to the slide radius. Besides, differences between Cases-D11 & D12 are more visible when the slide volume is increased. For instance, the peak KETR difference of Cases-D11 & D12 with 125 m^3 of the slide volume are almost the same. The differences depend mainly on maximum kinetic energy of the landslide, because the slide volume affects the maximum kinetic energy of the landslide more for Case-D11 as shown in Figure 5.28/e. As the maximum kinetic energy of the landslide increases, the energy transfer ratios decrease.

Figure 5.28/f demonstrates that when the slide volume is increased, the maximum wave rise increases. Unlike the energy transfer ratios, the slide radius affects the maximum wave crest more. However, the maximum wave crests are relatively small.

In **Case-D13** a number of numerical simulations are performed to understand effects of the submarine runaway distance on the wave generation. Figure 5.29/a & b point out that lengthening the submarine runaway distance causes an increase in KETR and PETR. It challenges the observations for the runaway distance in Case-D3; however, these parameters have different roles on the wave generation. The runaway distance changes the splash zone effect, the submarine runaway distance only affects the landslide runout inside the dam reservoir.

In fact, based in Figure 5.29/c, which shows maximum kinetic energy of the landslide vs. submarine runaway distance, the energy transfer ratios are supposed to decrease when runaway distance inside the dam reservoir elongates. The reason not to observe this situation indicates the fact that an increase in the energy exerted into the water is higher than the maximum kinetic energy of the landslide. Therefore, the energy transfer ratios cannot be correlated with the maximum kinetic energy of the landslide alone.

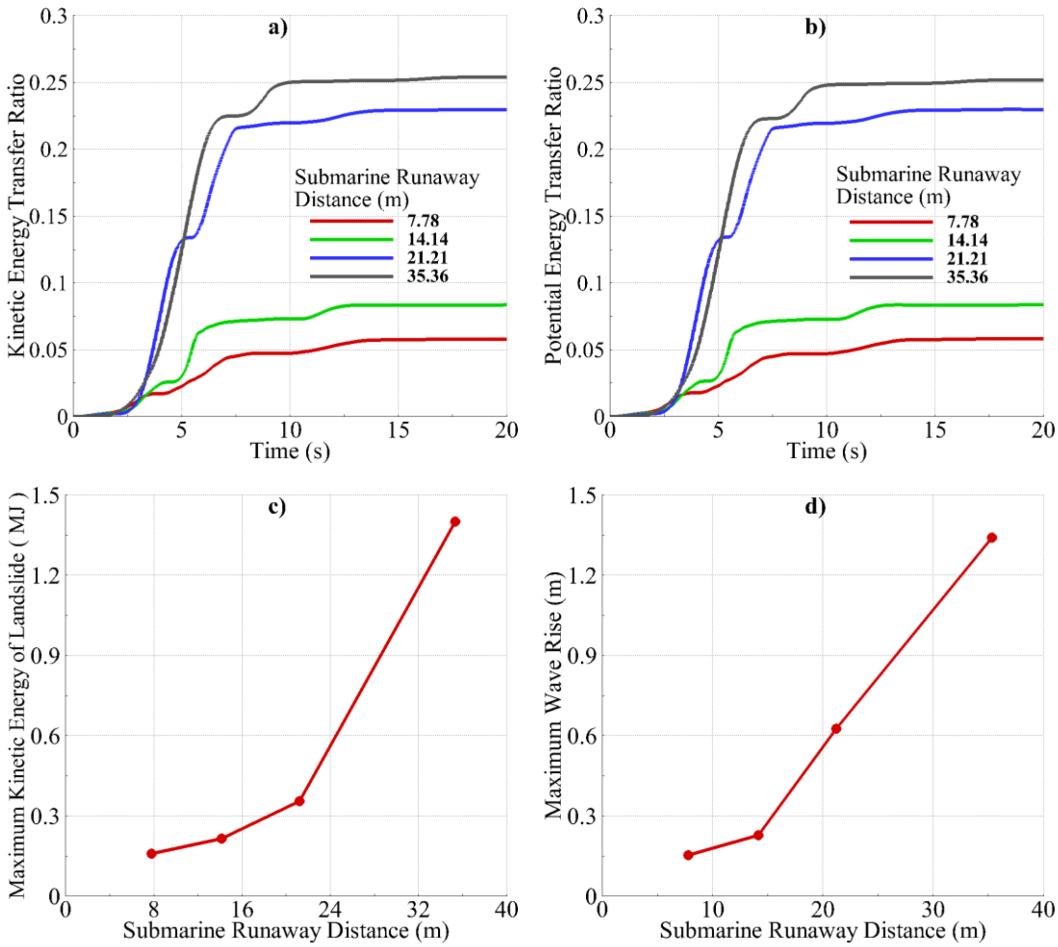

Figure 5.29: For Case-D13; a) KETR vs. Time, b) PETR vs. Time, c) Maximum Kinetic Energy of the Landslide vs. Submarine Runaway Distance and d) Maximum Wave Rise vs. Submarine Runaway Distance

The maximum wave rise increases with an increase of the submarine runaway distance as shown in Figure 5.29/d. As depicted in Table 5.23, the time required for the maximum wave crest increases with submarine runaway distance since the submarine runaway distance increases the distance for accumulation of the slide. However, it cannot have an influence on the location of maximum wave crest.

Table 5.23: Point and Time of Maximum Wave Rise for Case-D13 of Test Cases D

Submarine Runaway Distance (m)	Point of Maximum Wave Rise (m)	Time Required for Maximum Wave Rise (s)
7.78	5.5	3.11
14.14	5.5	3.35
21.21	5.5	4.24
35.36	5.5	5.44

In **Case-D14**, a series of numerical experiments arranged to investigate the effects of slide angle to the wave generation. The results for the energy transfer ratios and maximum kinetic energy of the landslide and maximum wave rise are presented in Figure 5.30. These simulations give an opportunity to understand the effects of the hydrostatic pressure over the landslide for submarine conditions of Test Cases D. Figures 5.30/a & b for KETR and PETR show that the landslides with 15^o, 25^o and 35^o of the slide angle are in a stationary position. However, in Case-D4, only the landslide with the slide angle of 15^o was at rest. Hydrostatic pressure over the landslide is effective in this case. It also differs with the subaerial conditions of Circular Landslide Modelling, because there is an optimum slide angle for observing maximum energy transfer ratios. Particularly, as the bed gets deeper, the maximum energy transfer ratios are prone to increase.

Figure 5.30/c shows an increase in maximum kinetic energy of the landslide with the steeper angle similar with the energy transfer ratios observed.

Figure 5.30/d confirms that the maximum wave crest tends to increase as the slide angle is increased. The slide angle affects the maximum wave rise regardless of the landslide characteristics.

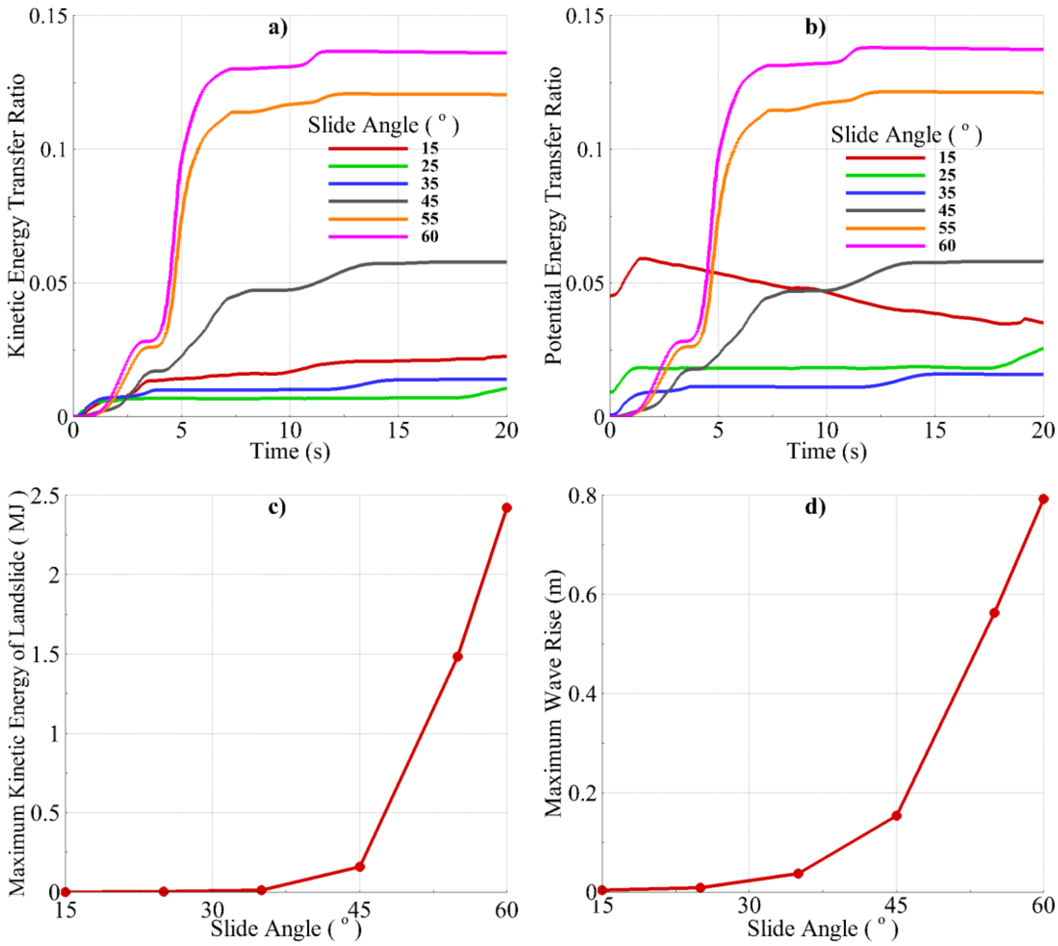

Figure 5.30: For Case-D14; a) KETR vs. Time, b) PETR vs. Time, c) Maximum Kinetic Energy of the Landslide vs. Slide Angle and d) Maximum Wave Rise vs. Slide Angle

Case-D15 is designed to analyze the effects of initial water depth for the wave generation with 40, 45, 50 and 60 meters and the results are illustrated in Figure 5.31. In fact, submarine landslide is more probable at deep water. However, investigating the deeper water depths may be inconvenient by utilizing the SWEs.

Submarine runaway distance changes with the water depth. The reason for the variation of the submarine runaway distance is because the location of the landslide is not changed while increasing the water depth. The bathymetry is only arranged with initial water depth.

As shown in Figures 5.31/a & b, KETR and PETR increase with shallower dam reservoirs, but the increase is relatively small. Insomuch that these variations may be affected partly due to the submarine runaway distance. Figure 5.31/c demonstrates that the initial water depth cannot be a major factor to affect the maximum wave crest as similar wave rises are observed for each simulation.

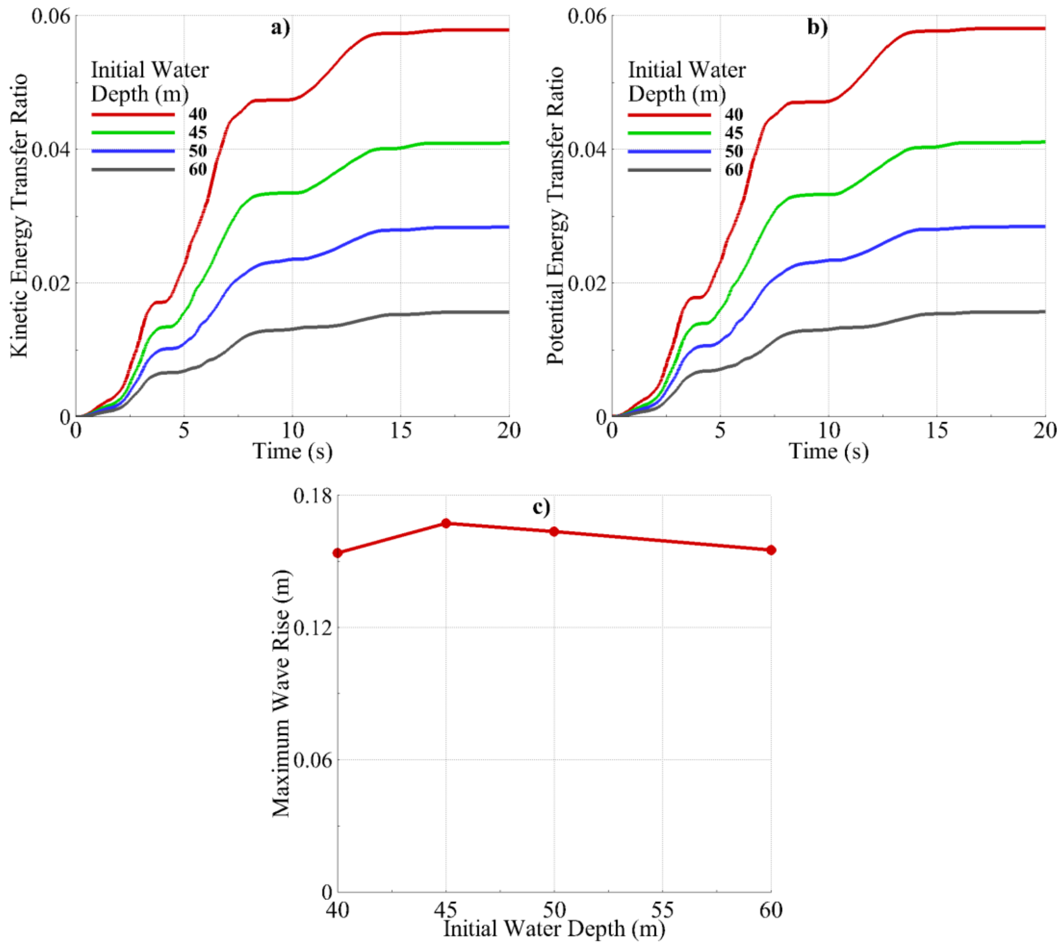

Figure 5.31: For Case-D15; a) KETR vs. Time, b) PETR vs. Time and d) Maximum Wave Rise vs. Initial Water Depth

In **Case-D16 & Case-D17** the internal friction angle of soil and the friction angle of the bed are considered as variables.

Firstly, Figure 5.32/a & b indicate that KETR and PETR increase by decreasing the internal friction angle of the soil. Obviously, as the internal friction angle of soil is decreased, the fluidic characteristics of the landslide increases. Hence, more fluidic landslide has a potential to increase the energy transfer ratios. It validates the ideas mentioned in Case-D6 and Case-C5. Nevertheless, a significant difference for the energy transfer ratios between submarine and subaerial conditions is that peak KETR and PETR tend to converge up to a certain point. Particularly, as the internal friction angle of soil is decreased, less increase for peak KETR and PETR is observed compared to the previous simulation.

KETR and PETR graphs due to the variations of the friction angle of bed are demonstrated in Figures 5.32/c & d. When the internal friction angle of soil equals to friction angle of bed, the bed roughness become maximum. It means that the soil and the bed are made up of the same material. As the friction angle of bed is decreased, the bed becomes smoother and it decreases the friction stress for the slide. Therefore, a decrease in friction angle of bed allows the landslide running-out fast and leads to increasing in the energy transfer ratios. However, these variations change slightly for the energy transfer ratios.

The maximum wave rises are depicted in Figure 5.32/e & f for internal friction angle of soil and friction angle of the bed, respectively. The maximum wave crest decreases when both internal friction angle of soil and friction angle of bed are increased. In fact, decreasing the internal friction angle of soil causes fast landslide because of possessing more fluidic characteristics. Decreasing the friction angle of the bed allow fast slide due to smoother bed. Consequently, fast landslide results in higher maximum wave crest.

Aa shown in Table 5.24, unlike the subaerial conditions of Circular Landslide Modelling, the maximum wave crests for all numerical experiments form at the same location for Case-D16. There are small changes in the maximum wave crests in Case-D17.

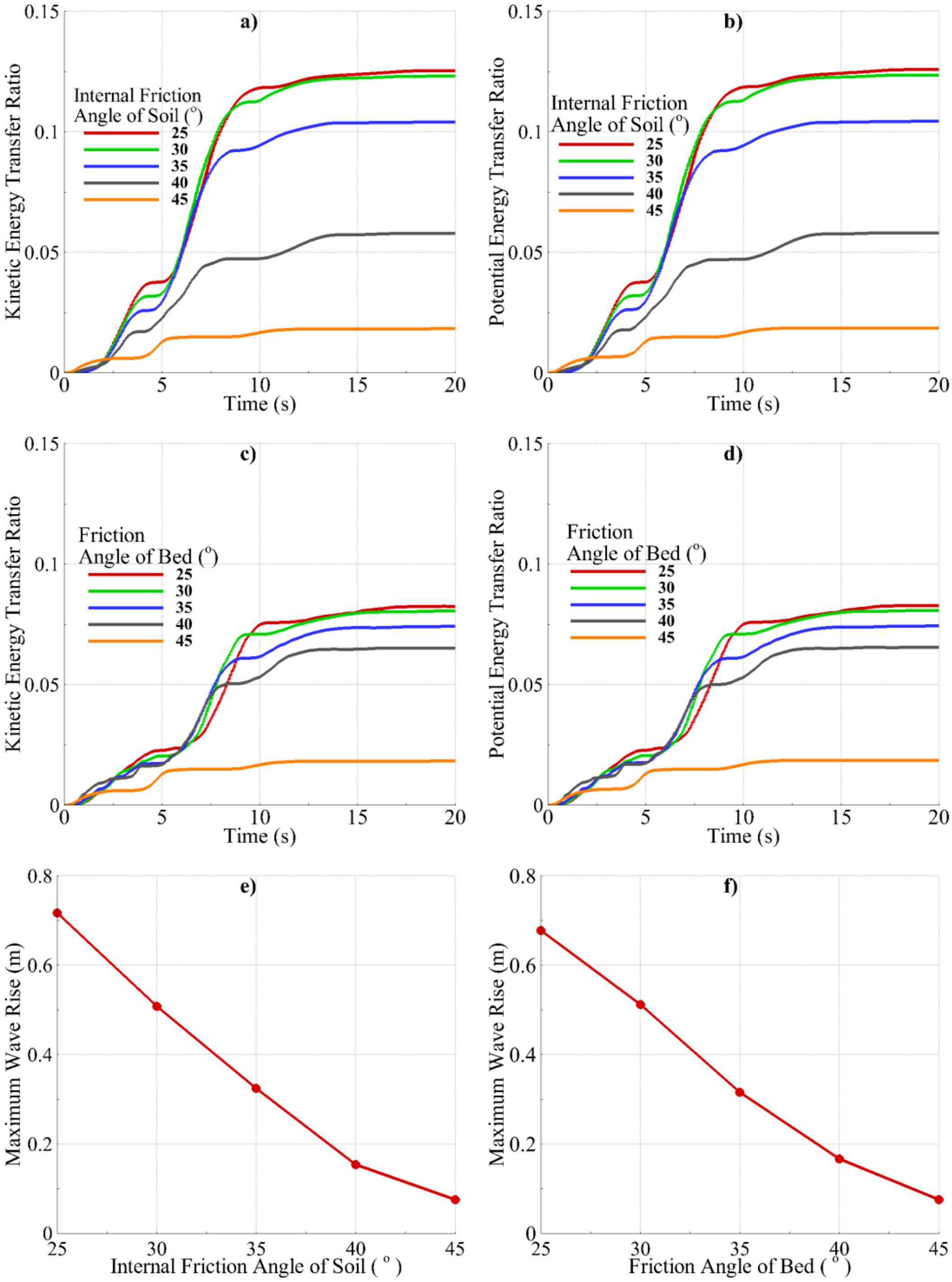

Figure 5.32: a) KETR vs. Time for Case-D16, b) PETR vs. Time for Case-D16, c) KETR vs. Time for Case-D17, d) PETR vs. Time for Case-D17, e) Maximum Wave Rise vs. Internal Friction Angle of Soil for Case-D16 and f) Maximum Wave Rise vs. Friction Angle of Bed for Case-D17

Table 5.24: Point and Time of Maximum Wave Rise for Cases-D16 & D17 of Test Cases D

Point of Maximum Wave Rise for Case-D16 (m)	Time Required for Maximum Wave Rise for Case-D16 (s)	Point of Maximum Wave Rise for Case-D17 (m)	Time Required for Maximum Wave Rise for Case-D17 (s)
7.5	3.27	6	2.3
5.5	2.93	6.5	2.63
5.5	2.99	5.5	2.52
5.5	3.11	7.5	3.84
5.5	1.17	5.5	1.17

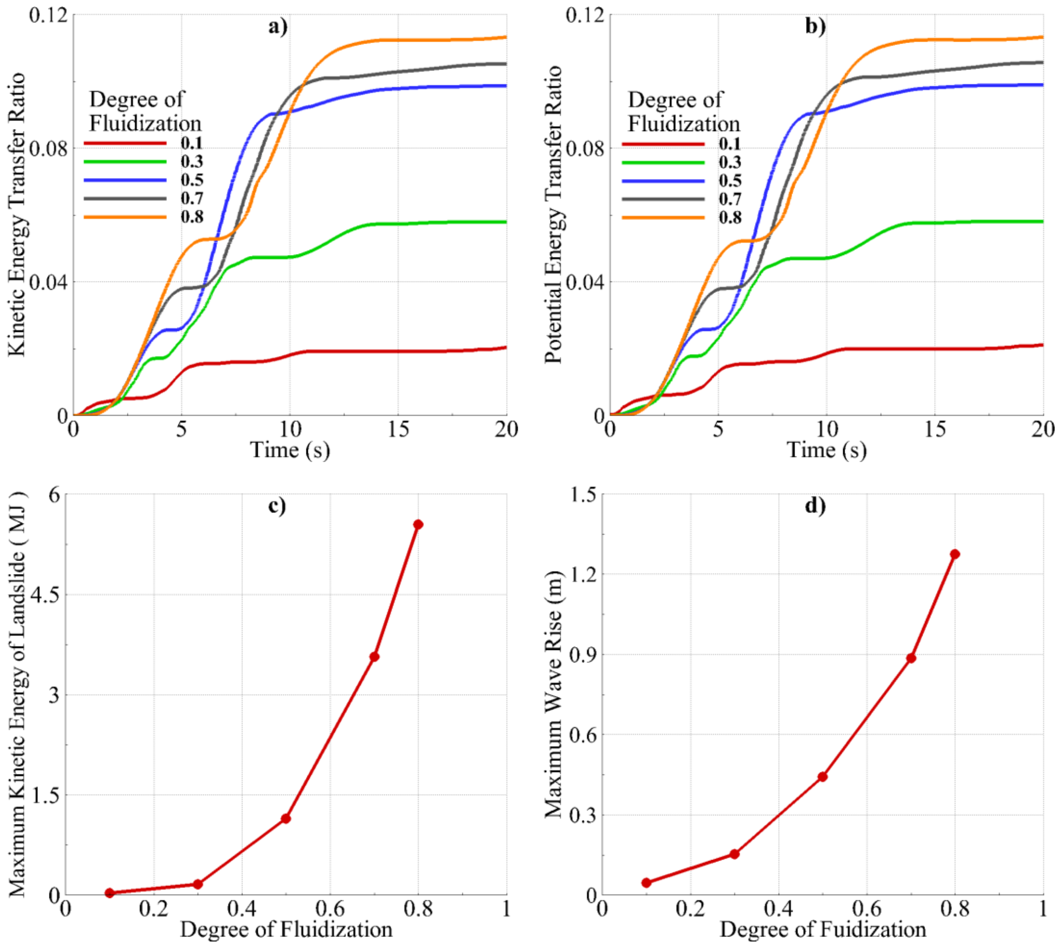

Figure 5.33: For Case-D18; a) KETR vs. Time, b) PETR vs. Time, c) Maximum Kinetic Energy of the Landslide vs. Degree of Fluidization and d) Maximum Wave Rise vs. Degree of Fluidization

Case-D18 studies degree of fluidization and the results are given in Figure 5.33. Figures 5.33/a & b point out that when the degree of fluidization is increased, the energy transfer ratios increase. It is because the degree of fluidization determines the fluidic characteristics of the landslide. As the degree of fluidization approaches to 1 the slide material becomes more fluidic. Increasing fluidity of the landslide lead to increasing energy transfer ratios. Fluid characteristics also increase the maximum kinetic energy of the landslide (Figure 5.33/c). Besides, the fluid characteristics cause an increase in the maximum wave rise as illustrated in Figure 5.33/d. Fluidity of the landslide material results in an increase in both the maximum kinetic energy of the landslide and the energy transfer ratios. In Table 5.25 it is observed that the maximum wave crest occurs at longer distances and taking more time when the degree of fluidization is increased.

Table 5.25: Point and Time of Maximum Wave Rise for Case-D18 of Test Case D

Degree of Fluidization	Point of Maximum Wave Rise for Case-D18 (m)	Time Required for Maximum Wave Rise for Case-D18 (s)
0.1	0.5	1.06
0.3	0.5	3.11
0.5	0.5	2.63
0.7	6	3.2
0.8	19.5	4

In **Case-D19**, density of the granular flow is investigated with a series of numerical experiments. As shown in Figures 5.34/a & b, the energy transfer ratios tend to decrease when the density of the granular flow increases. The coefficient of the pressure force term due to the water, $\frac{\rho}{\rho_g}$, in Equation 3.29, decreases with the denser landslide and then, fast landslide leads to a decrease in the energy transfer ratios. These results are similar for all test cases. Figure 5.34/c shows that the maximum wave rise increases with the density of the granular flow. However, Case-C9 and Case-D9 indicate that there are no variations in the maximum wave crests. Here, the increase in the maximum wave rise can be considered as the effects of submarine conditions.

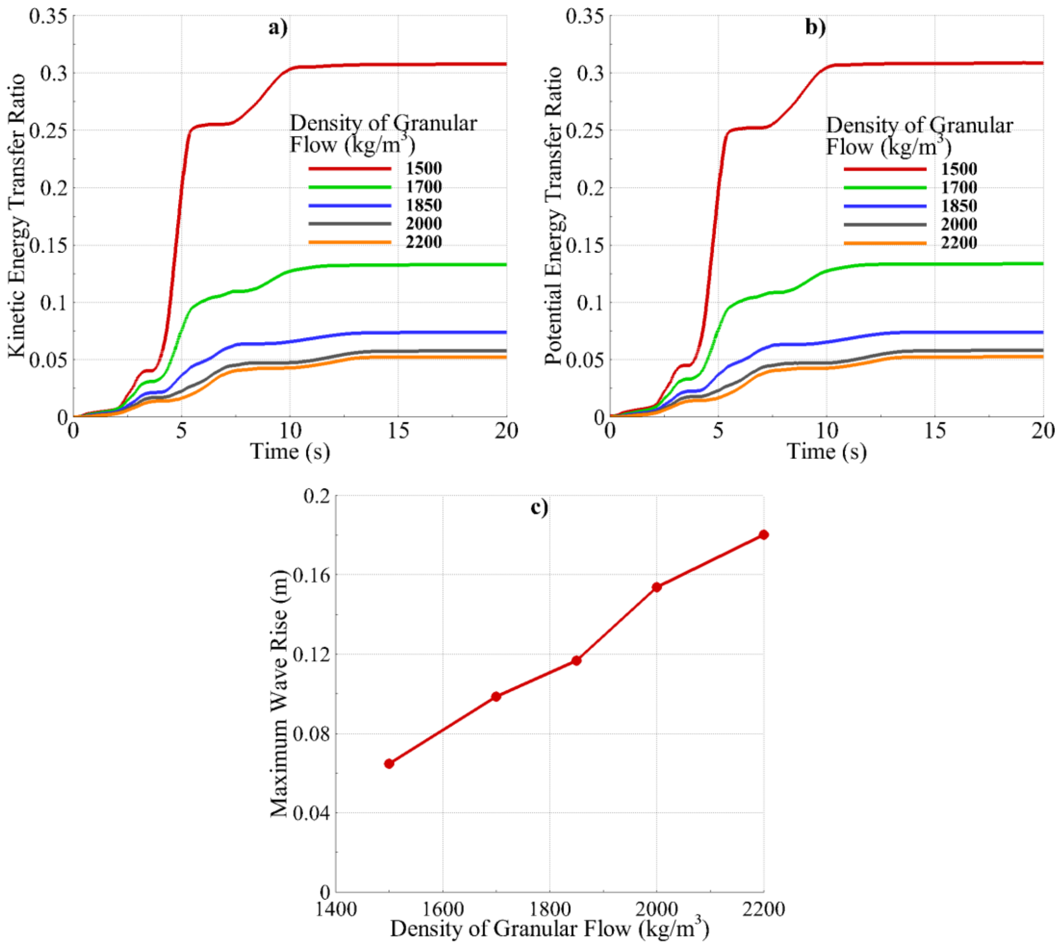

Figure 5.34: For Case-D19; a) KETR vs. Time, b) PETR vs. Time and c) Maximum Wave Rise vs. Density of Granular Flow

Case-D20 is designed to investigate the manning coefficient. The energy transfer ratios look almost similar for every manning coefficient. However, it was observed from the other test cases that the energy transfer ratio tends to decrease along the channel and it directly affects the wave propagations. The reason not to observe a decrease in the energy transfer ratio may be about possessing small amount of the absorbed energy by the water therefore the changes in the energy transfer ratios are negligible small. The other reason may be explained that, within 20 seconds, the landslide still affects the waves; therefore, the waves have not reached the far-field area, yet. Furthermore, it does not change the maximum wave rise significantly (Figure 5.35/c).

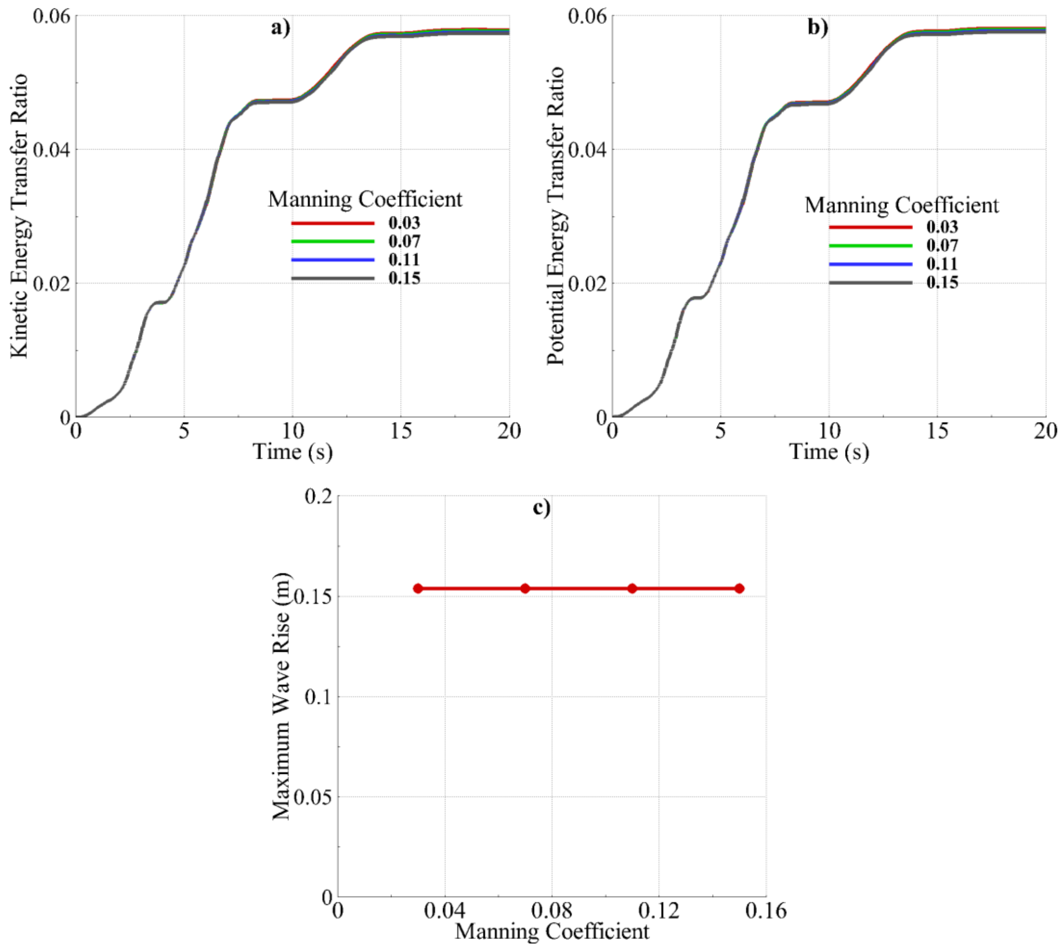

Figure 5.35: For Case-D20; a) KETR vs. Time, b) PETR vs. Time and c) Maximum Wave Rise vs. Manning Coefficient

Summary of observations for submarine landslides:

a) Energy transfer ratio increases with radius of slide as the slide volume is increased.

b) Energy transfer ratio increase with slide length as the slide volume is increased.

c) Maximum wave rise is increases with slide volume for both cases due to increase in radius or increase in length.

d) Energy transfer ratio increases with the runaway distance.

e) Maximum wave rise increases with the runaway distance.

f) Energy transfer ratio is negligible for slide angles less than 40^0, increases for higher slide angles.

g) There is strong increase in maximum wave rise when the slide angle increases.

h) Increase in water depth in the reservoir results in a decrease in energy transfer.

i) Maximum wave rise is independent of water depth.

j) Increase in internal friction angle of the slide causes a decrease in energy transfer ratio.

k) Increase in bed friction reduces energy transfer rates.

l) Increase in both internal friction angle and bed friction results in decrease wave rise.

m) Energy transfer ratio increases with degree of fluidization.

n) Maximum wave rise increases with degree of fluidization.

o) Energy transfer ratio decreases with increase slide density.

p) Maximum wave rise increases with increase in slide density.

q) Energy transfer ratio is independent of Manning's parameter.

r) Maximum wave rise is independent of Manning's parameter.

5.5 Test Cases E

So far, a variety of numerical experiments are performed to understand the wave generation and propagation mechanisms after a landslide into a dam reservoir. An interesting case would be a landslide triggered by earthquake and superposition of waves generated by earthquake and the landslide. This section is devoted to the study of Two-Layer Circular Landslide triggered by an earthquake. Model description of landslide geometry and related parameters to be studied are shown in Figure 5.36.

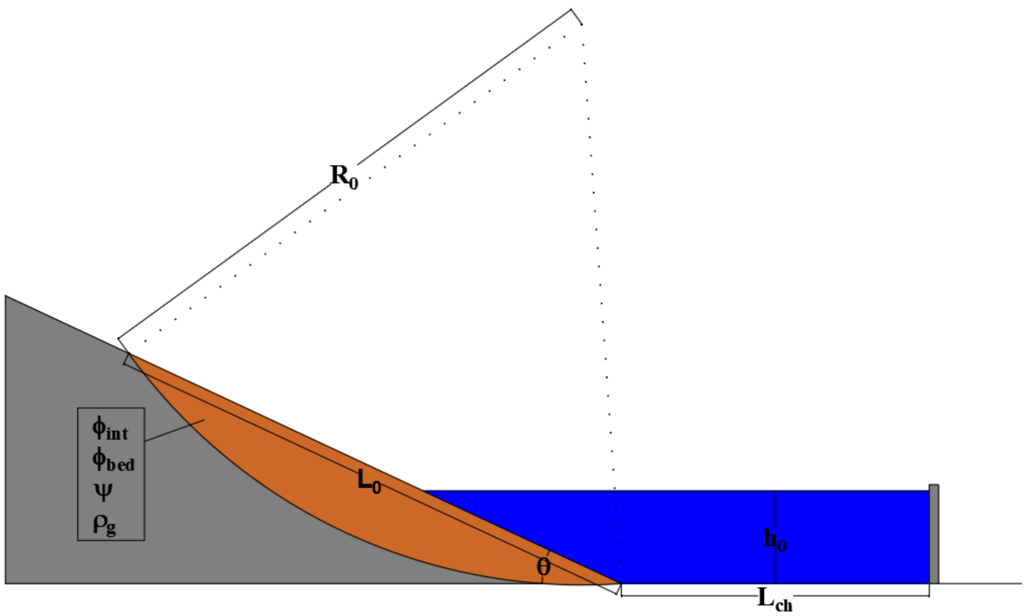

Figure 5.36: Assumed Test Geometry for the Two-Layer Circular Landslide and Earthquake Model

Slide material properties are internal friction angle of the soil ($\emptyset_{int}$), friction angle of the bed ($\emptyset_{bed}$), degree of fluidization (ψ) and density of the landslide (ρ_g). Environmental variables are initial water depth (h_0), channel length of the dam reservoir (L_{ch}), the Manning's roughness (n), the slide angle (θ), the radius of curvature of the failure plane (R_0) and the slide length (L_0). The channel length of the dam reservoir is the distance between the toe of the inclined ramp and the dam body. Unlike other test cases, the far-field boundary condition does not apply because of studying the effects of the earthquake over the dam reservoir.

The range of variables tested in this group of numerical experiments are given in Table 5.26. Investigation of the effects of the earthquake over landslide and wave propagation is accomplished by observing variations in maximum wave rise, maximum overflow depth and spill volume.

Table 5.26: Definition of Variables Range for Subaerial Part of Test Cases E

	Case-E1	**Case-E2**	**Case-E3**	**Case-E4**
Volume of Slide ($\mathbf{m^3}$)	682.01	682.01	682.01	682.01
Radius of Curvature (m)	90.88	90.88	90.88	90.88
Slide Length (m)	88.27	88.27	88.27	88.27
Slide Angle (^{o})	25	25	25	25
Initial Water Depth (m)	15	10-15-20	15	15
Channel Length (m)	50	50	50-100-200	50
Internal Friction angle of Soil (^{o})	40	40	40	40
Friction Angle of Bed (^{o})	40	40	40	40
Degree of Fluidization	0.3	0.3	0.3	0.3
Density of Granular Flow (kg/m^3)	2000	2000	2000	2000
Manning Coefficient	0.03	0.03	0.03	0.03
Freeboard of Dam Body (m)	1	1	1	1
Amplitude of Earthquake in m/s^2 (*g*)	0.8	0.8	0.8	0.1-0.4-0.8-1.0

A sinusoidal earthquake acceleration in horizontal direction was applied. The amplitude of the earthquake is 0.8g and the wave period is 3 seconds. Earthquake starts in the third second lasts in 6 seconds in 9^{th} second of the simulation (Figure 5.37).

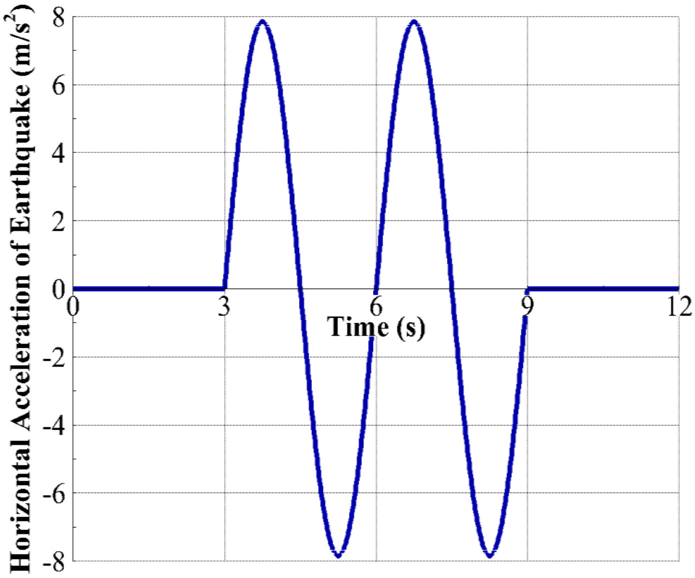

Figure 5.37: Description of Sinusoidal Earthquake Acceleration

Case-E1 is designed to observe a landslide which would not occur unless an earthquake triggers. Three simulations are done:

- Simulation-1) No landslide is expected for the selected parameters (Table 5.26). There is no earthquake acceleration applied. Therefore, no slide motion is expected. The code is run and a minimal slide occurs which produce a water wave of 0.23 m high. This minor slide is due to numerical disturbances created during the numerical solution. The sliding volume finds a new equilibrium position after a small displacement.

- Simulation-2) It is supposed that the earthquake occurs but there is no landslide. Occurrence of landslide is numerically prevented.

-Simulation-3) Earthquake and the earthquake-triggered landslide occurs simultaneously.

The observed parameters are listed in Table 5.27 and the configurations of the slide material and water surface profile at the 19.4th and 43.1th seconds of the simulations are shown in Figure 5.38.

Table 5.27: Results for Series of Numerical Experiment for Case-E1

	Maximum Wave Rise (m)	**Maximum Overflow Depth (m)**	**Spill Volume (m^3)**
Simulation-1	0.23	0	0
Simulation-2	8.62	4.23	141.40
Simulation-3	8.81	4.35	180.36

In Simulation-1, it is observed that small water waves occurred due to small displacement of the slide. As shown in Table 5.27 the earthquake effects over the dam reservoir are highly dominant thus the difference between Simulation-2 and Simulation-3 is small for the case considered here. However, there is a considerable increase in spilled water volume when the earthquake is accompanied by a landslide.

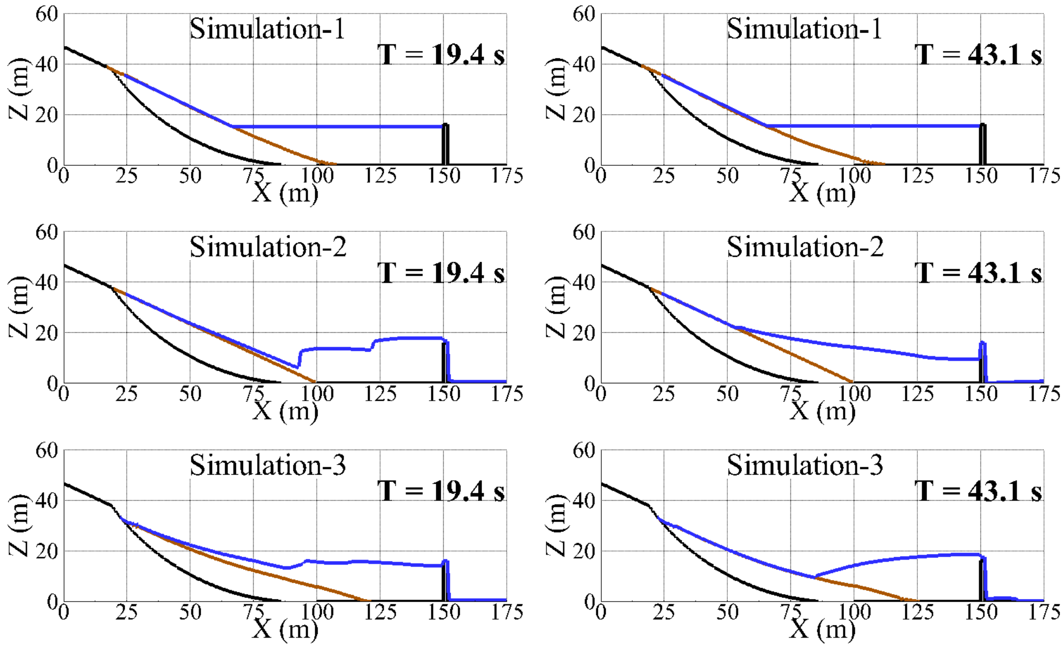

Figure 5.38: Screenshots of simulations-1, -2 and -3

Figure 5.38 demonstrates the bathymetry change and water surface profiles in Simulations-1, 2, and 3 at t=19.4 s and t=43.1 s. Superposition of earthquake and landslide amplifies the wave heights and results in increased spill volumes. The spill discharge is shown as function of time in Figure 5.39. The maximum spill occurs in the first wave and then gradually decreases after every cycle of oscillation.

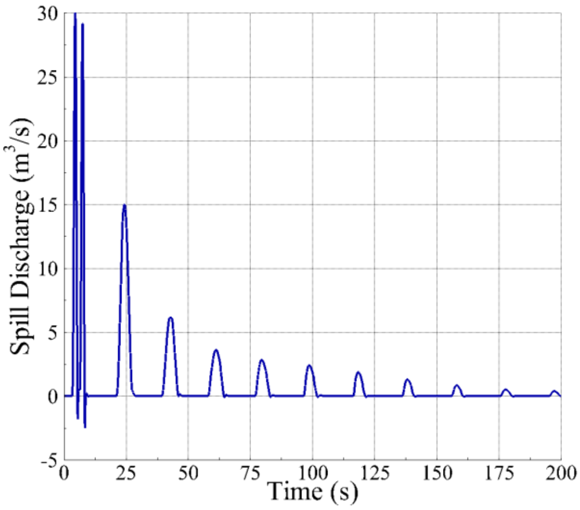

Figure 5.39: Spill discharge for Simulation-3 of Case-E1

Table 5.28: Results for Series of Numerical Experiments for Case-E2

Initial Water Depth (m)	**Maximum Wave Rise (m)**		**Maximum Overflow Depth (m)**		**Spill Volume (m^3)**	
	Simulation-					
	2	**3**	**2**	**3**	**2**	**3**
10	7.18	7.26	3.43	3.45	102.36	137.79
15	8.62	8.81	4.23	4.35	141.40	180.36
20	9.85	9.96	4.92	4.98	150.56	222.68

Effect of water depth is studied in **Case-E2**. Simulation 2 is earthquake alone and Simulation 3 is earthquake and landslide combined. Observations are summarized in Table 5.28. Increasing water depth results in increased waves and spill volumes. Figure 5.40 shows the configurations of the landslide and water surface profile for different initial water depths.

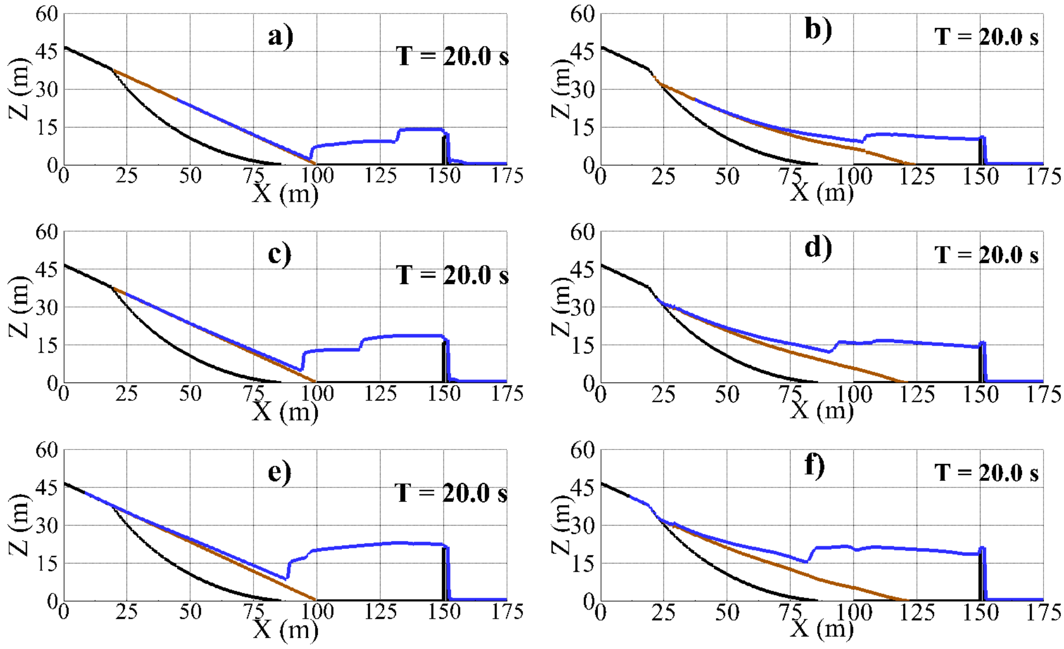

Figure 5.40: Screenshots of Simulation-2 when Initial Water Depth is; a) 10 meters; c) 15 meters and e) 20 meters and of Simulation-3 when Initial Water Depth is; b) 10 meters; d) 15 meters and f) 20 meters at Time = 20.0 Seconds

Table 5.29: Results for Series of Numerical Experiments for Case-E3

Channel Length (m)	**Maximum Wave Rise (m)**		**Maximum Overflow Depth (m)**		**Spill Volume (m^3)**	
	Simulation-					
	2	**3**	**2**	**3**	**2**	**3**
50	8.62	8.81	4.23	4.35	141.40	180.36
100	8.62	8.62	4.23	4.23	234.18	251.60
200	8.62	8.62	4.23	4.23	239.59	246.04

Effect of propagation distance is considered in **Case-E3**, results of which are shown in Table 5.29. Wave rise is independent of travel distance but the spill volumes are increased. Spill volumes are increased more in case of superposition of landslide and earthquake. The configurations of the slide material and water surface profile at the 20^{th} seconds of the simulations are demonstrated in Figure 5.41.

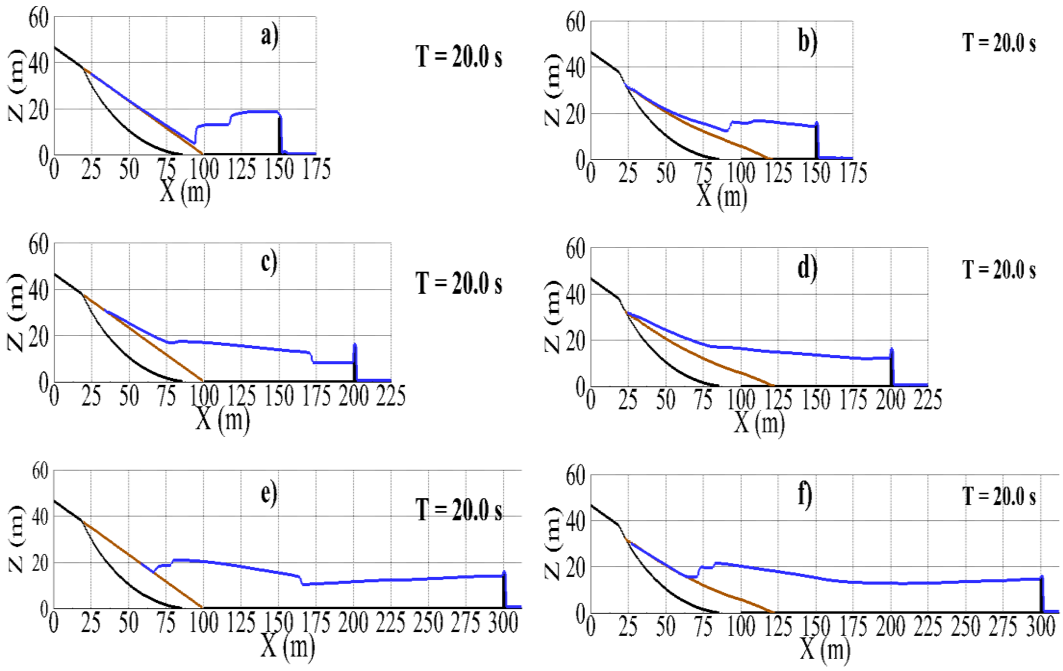

Figure 5.41: Screenshots of Simulation-2 when Channel Length is; a) 50 meters; c) 100 meters and e) 200 meters and of Simulation-3 when Channel Length is; b) 50 meters; d) 100 meters and f) 200 meters at Time = 20.0 Seconds

Effects of the amplitude of earthquake are considered in **Case-E4**, results of which are illustrated in Table 5.30. The amplitude of earthquake increases the wave heights and spill volume. The configurations of the slide material and water surface profile at the 20th seconds of the simulations are illustrated in Figure 5.42.

Table 5.30: Results for Series of Numerical Experiments for Case-E4

Amplitude of Earthquake (*g*) in m/s^2	**Maximum Wave Rise (m)**		**Maximum Overflow Depth (m)**		**Spill Volume (m^3)**	
	Simulation-					
	2	**3**	**2**	**3**	**2**	**3**
0.1	1.22	1.51	0.11	0.27	0.43	10.54
0.4	4.34	4.49	1.69	1.78	67.41	89.95
0.8	8.62	8.81	4.23	4.35	141.40	180.36
1.0	10.85	11.06	5.64	5.76	163.89	229.13

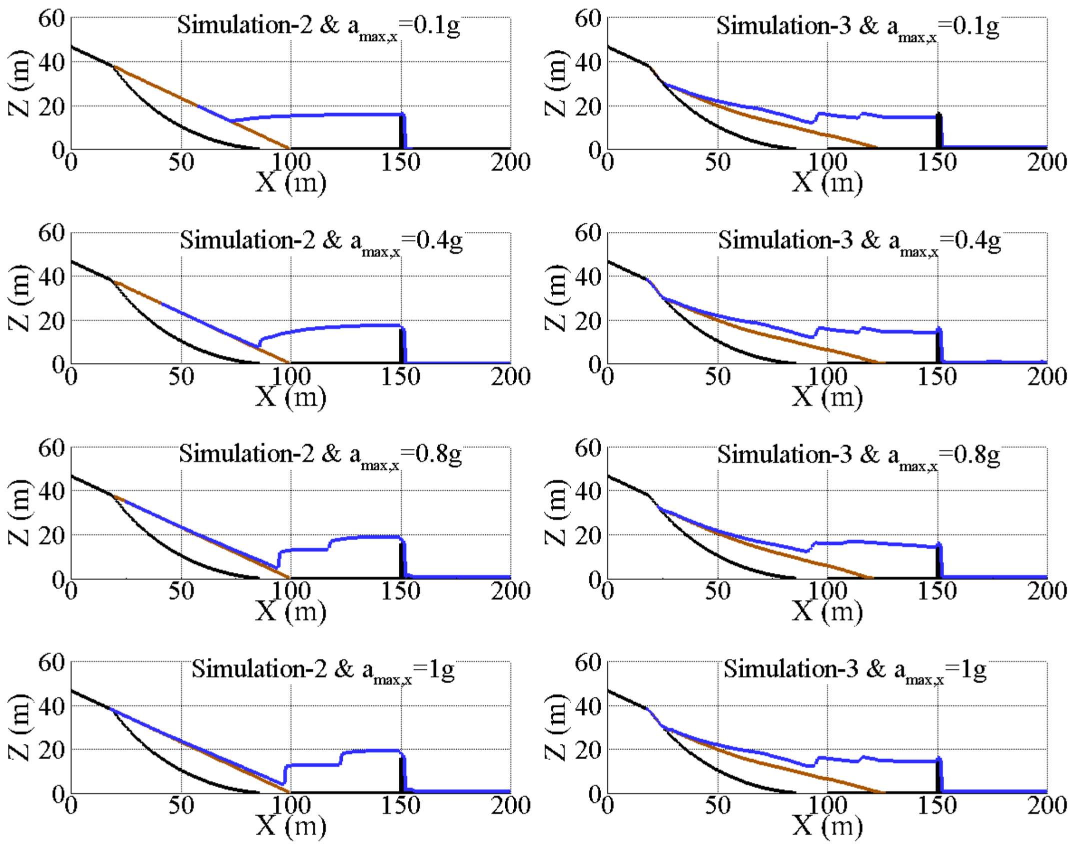

Figure 5.42: For Case-E4, screenshots of Simulation-2 and -3 at Time = 20.0 Seconds

CHAPTER 6

CONCLUSIONS AND RECOMMENDATIONS

The work presented in this thesis study provides evaluations of modeling by depth-integrated equations for a variety of idealized landslide model configurations. Conclusions based on numerical solutions presented in the thesis are summarized as follows:

Numerical simulation of the landslide and water waves generated was achieved using 1D Shallow flow theory. The Coulomb model as a rheological model of the slide motion was adopted. Finite Volume Method (FVM) was applied in order to solve the governing equations. Abrupt changes in the channel bed elevation due to the landslide motion was one of the difficulties in numerical solution. First-order well-balanced discretization was implemented as a cure for numerical fluctuations due to rapid bed elevation changes.

Numerical experiments were carried out under groups of one-layer modelling, rigid block modelling, translational landslide modelling, circular landslide modelling, and, circular landslide and earthquake co-existent modelling. The mathematical model produced successful numerical solutions for all cases studied. The cpu and memory requirements are not significant, quick solutions in a laptop computer can be obtained. The parameters used to describe the slide material and geometry gives an opportunity to consider different scenarios to search for the most critical conditions in terms of wave generation and overtopping from spillway.

The approach in Case-A has been used in the literature to evaluate possible wave heights for practical situations. However, since the slide material is replaced by an equivalent water volume, there are no parameters to input slide material characteristics. Slide volume generates a channel flow on the slide surface when long runaway distances are considered. On the other hand, slide volume mixes with water in the reservoir, losing its kinetic characteristics immediately after the impact on the reservoir. Therefore, although it is easy to apply, Case-A is not recommended as a valid method for estimation of water waves in the reservoirs after a landslide.

A fixed shape rigid block (Case-B) is used in experimental studies performed in laboratories. Numerical models are usually validated based on experimental data. This thesis is a part of such an experimental and numerical research project. Numerical experiments of the present study showed that height of waves produced by the block is affected by block speed, height and the front angle of the block. For a given block velocity, wave height decreases with slide angle and water depth. Findings of the present 1D analysis will be useful in developing the experimental program.

The two-layer modeling in test Cases C and D provides a realistic model for two typical landslides. Interaction of water and the slide material is allowed while the slide material moves into the reservoir. It gives an opportunity to simulate a real case by assigning appropriate values for the slide parameters. However, an extension of the code is necessary for 2D solution in horizontal plane to better describe the slide and the reservoir geometry.

The energy transfer ratio and the maximum wave rise were considered as major quantities to scale the consequences of a landslide in a reservoir as was done in many previous studies.

Energy transfer ratio increases with increasing slide thickness, slide angle up to a certain slope, water depth and degree of fluidization. A decrease in energy transfer ratio is observed for increasing slide length, slide angles larger than a certain slope, friction angle of the slide, slide density and bed roughness. The critical slide slope for the maximum energy transfer rate can be in the range of 35^0~45^0, however, it is dependent on type of slide geometry.

The maximum wave rise increases with slide angle and degree of fluidization, and, decreases with friction angles of both the slide and the bed in general. The relation between the other parameters studied and the wave rise is case dependent and cannot be generalized.

The two-layer numerical model can simulate landslides and earthquake triggered landslides simultaneously with earthquake acceleration. Such a model can provide more accurate information on the increased risk of landslides triggered by earthquakes. Observations in this study indicate that coexistent earthquake and landslide can cause a significant increase in wave heights and water spill over the crest.

Overall, this parametric study shows that a generalized relation between the landslide characteristics and the generated water wave characteristics is not feasible. Thus, a 2D numerical simulation for each specific case would be necessary for precise evaluation of landslide generated risk on dam reservoirs. Thus, a 2D extension of the two-layer modeling would be more appropriate to study the landslide risk in real dam reservoirs as a future work.

REFERENCES

Audusse, E., Bouchut, F., Bristeau, M. O., Klein, R., & Perthame, B. (2004). A fast and stable well-balanced scheme with hydrostatic reconstruction for shallow water flows. *SIAM Journal of Scientific Computing*, *25*(6), 2050–2065. https://doi.org/10.1137/S1064827503431090

Bingham, E. C. (1916). An investigation of the laws of plastic flow. *Bulletin of the Bureau of Standards*, *13*(2), 309. https://doi.org/10.6028/bulletin.304

Burton, I., Kates, R. W., & White, G. F. (1993). *The environement as hazard*.

Coussot, P. (1994). Steady, laminar, flow of concentrated mud suspensions in open channel: Ecoulements à surface libre permanents et laminaires de suspensions boueuses concentrées. *Journal of Hydraulic Research*, *32*(4), 535–559. https://doi.org/10.1080/00221686.1994.9728354

Denlinger, R. P., & Iverson, R. M. (2001). Flow of variably fluidized granular masses across three-dimensional terrain 2. Numerical predictions and experimental tests. *Journal of Geophysical Research: Solid Earth*, *106*(B1), 553–566. https://doi.org/10.1029/2000jb900330

Denlinger, R. P., & Iverson, R. M. (2004). Granular avalanches across irregular three-dimensional terrain: 1. Theory and computation. *Journal of Geophysical Research: Earth Surface*, *109*(F1). https://doi.org/10.1029/2003jf000085

Fritz, H. M., Hager, W. H., & Minor, H.-E. (2004). Near Field Characteristics of Landslide Generated Impulse Waves. *Journal of Waterway, Port, Coastal, and Ocean Engineering*, *130*(6), 287–302. https://doi.org/10.1061/(asce)0733-950x(2004)130:6(287)

George, D. L., & Iverson, R. M. (2014). A depth-averaged debris-flow model that includes the effects of evolving dilatancy. II. Numerical predictions and experimental tests. *Proceedings of the Royal Society A: Mathematical, Physical and Engineering Sciences*, *470*(2170). https://doi.org/10.1098/rspa.2013.0820

Harbitz, C. B., Løvholt, F., & Bungum, H. (2014). Submarine landslide tsunamis: How extreme and how likely? *Natural Hazards*, *72*(3), 1341–1374. https://doi.org/10.1007/s11069-013-0681-3

Heller, V., & Hager, W. H. (2010). Impulse Product Parameter in Landslide Generated Impulse Waves. *Journal of Waterway, Port, Coastal, and Ocean Engineering*, *136*(3), 145–155. https://doi.org/10.1061/(asce)ww.1943-5460.0000037

Iverson, R. M. (1997). of Debris. *Review of Geophysics*, *35*(97), 245–296.

Iverson, R. M., & Denlinger, R. P. (2001). *Coulomb mixture theory Ns = (p •_. 106*, 537–552.

Iverson, R. M., & George, D. L. (2014). A depth-averaged debris-flow model that includes the effects of evolving dilatancy. I. Physical basis. *Proceedings of the Royal Society A: Mathematical, Physical and Engineering Sciences*, *470*(2170). https://doi.org/10.1098/rspa.2013.0819

Iverson, R. M., Logan, M., & Denlinger, R. P. (2004). Granular avalanches across irregular three-dimensional terrain: 2. Experimental tests. *Journal of Geophysical Research: Earth Surface*, *109*(F1), 1–16. https://doi.org/10.1029/2003jf000084

Kilburn, C. R. J., & Petley, D. N. (2003). *Forecasting giant , catastrophic slope collapse : lessons from Vajont , Northern Italy*. *54*, 21–32. https://doi.org/10.1016/S0169-555X(03)00052-7

Ma, G., Kirby, J. T., Hsu, T. J., & Shi, F. (2015). A two-layer granular landslide model for tsunami wave generation: Theory and computation. *Ocean Modelling*, *93*, 40–55. https://doi.org/10.1016/j.ocemod.2015.07.012

Ma, G., Shi, F., & Kirby, J. T. (2012). Shock-capturing non-hydrostatic model for fully dispersive surface wave processes. *Ocean Modelling*, *43–44*, 22–35. https://doi.org/10.1016/j.ocemod.2011.12.002

Midi, G. D. R. (2004). On dense granular flows. *European Physical Journal E*, *14*(4), 341–365. https://doi.org/10.1140/epje/i2003-10153-0

Savage, S. B., & Hutter, K. (1989). The motion of a finite mass of granular material down a rough incline. *Journal of Fluid Mechanics*, *199*(2697), 177–215. https://doi.org/10.1017/S0022112089000340

Savage, S. B., & Ttutter, K. (1991). A C T A M E C H A N I C A The dynamics of avalanches of granular materials from initiation to runout. Part I: Analysis. In *Acta hIechanica* (Vol. 86).

Toro, E. F. (n.d.). *Free Surface Toro.pdf*.

Yavari-Ramshe, S., & Ataie-Ashtiani, B. (2016). Numerical modeling of subaerial and submarine landslide-generated tsunami waves—recent advances and future challenges. *Landslides*, *13*(6), 1325–1368. https://doi.org/10.1007/s10346-016-0734-2

Zhang, C., Kirby, J. T., Shi, F., Ma, G., & Grilli, S. T. (2021a). A two-layer non-hydrostatic landslide model for tsunami generation on irregular bathymetry. 1. Theoretical basis. *Ocean Modelling*, *159*(September 2020), 101749. https://doi.org/10.1016/j.ocemod.2020.101749

Zhang, C., Kirby, J. T., Shi, F., Ma, G., & Grilli, S. T. (2021b). A two-layer non-hydrostatic landslide model for tsunami generation on irregular bathymetry. 2. Numerical discretization and model validation. *Ocean Modelling*, *160*(February), 101769. https://doi.org/10.1016/j.ocemod.2021.101769

APPENDICES

A. Derivation of Shallow Water Equations

Navier-Stokes's equations are a set of equations that describes the Newtonian fluid flow, like water. The water flow is an incompressible flow that refers to constant density. Therefore, incompressible Navier-Stokes's equations are written;

$$\frac{du}{dx} + \frac{dv}{dy} + \frac{dw}{dz} = 0 \qquad (A.1)$$

$$\rho\left(\frac{du}{dt} + u\frac{du}{dx} + v\frac{du}{dy} + w\frac{du}{dz}\right) = -\frac{dP}{dx} + \left(\frac{d\tau_{xx}}{dx} + \frac{d\tau_{yx}}{dy} + \frac{d\tau_{zx}}{dz}\right) + \rho a_x \qquad (A.2)$$

$$\rho\left(\frac{dv}{dt} + u\frac{dv}{dx} + v\frac{dv}{dy} + w\frac{dv}{dz}\right) = -\frac{dP}{dy} + \left(\frac{d\tau_{xy}}{dx} + \frac{d\tau_{yy}}{dy} + \frac{d\tau_{zy}}{dz}\right) + \rho a_y \qquad (A.3)$$

$$\rho\left(\frac{dw}{dt} + u\frac{dw}{dx} + v\frac{dw}{dy} + w\frac{dw}{dz}\right) = -\frac{dP}{dz} + \left(\frac{d\tau_{xz}}{dx} + \frac{d\tau_{yz}}{dy} + \frac{d\tau_{zz}}{dz}\right) + \rho g \qquad (A.4)$$

Where;

ρ is the density of water;

P is the pressure of water;

u, v and w are the velocity components of the water in x, y and z directions respectively and viscous terms applied on j.th plane towards i.th direction are represented by τ_{ij}.

a_x and a_y are the earthquake accelerations respectively in x and y directions.

Kinematic and dynamic boundary conditions are implemented on the Navier-Stokes Equations for the derivation of Shallow Water Equations. Kinematic BC is simply the constraint made by assuming that the acceleration of the free and bottom surfaces for the Navier-Stokes's equations is zero.

The free surface of the water is;

$$z = \eta(x, y, t) = h(x, y, t) + z_{bed}(x, y, t) \qquad (A.5)$$

The bottom surface of the water is;

$$z = z_{bed}(x, y, t) \qquad (A.6)$$

Where, η is the free surface of the water, z_{bed} is the bottom elevation and h is the water depth. In case of landslide-generated waves, the movable bottom surface is required to insert into the kinematic BC, because the granular flow disturbs the bottom surface of the water with time. Therefore, the bottom elevation is defined as function of space and time.

Total derivation of free surface and bottom is 0.

$$\frac{D(z-\eta)}{Dt} = 0 \qquad (A.7)$$

$$\frac{dz}{dt} + u\frac{dz}{dx} + v\frac{dz}{dy} + w\frac{dz}{dz} = \frac{d\eta}{dt} + u\frac{d\eta}{dx} + v\frac{d\eta}{dy} + w\frac{d\eta}{dz} \qquad (A.8)$$

$$\frac{D(z-z_{bed})}{Dt} = 0 \qquad (A.9)$$

$$\frac{dz}{dt} + u\frac{dz}{dx} + v\frac{dz}{dy} + w\frac{dz}{dz} = \frac{dz_{bed}}{dt} + u\frac{dz_{bed}}{dx} + v\frac{dz_{bed}}{dy} + w\frac{dz_{bed}}{dz} \qquad (A.10)$$

z is independent of t, x, y. Also, η and z_{bed} are independent of z. Then,

$$w_\eta = \frac{d\eta}{dt} + u\frac{d\eta}{dx} + v\frac{d\eta}{dy} \qquad (A.11)$$

$$w_{z_{bed}} = \frac{dz_{bed}}{dt} + u\frac{dz_{bed}}{dx} + v\frac{dz_{bed}}{dy} \qquad (A.12)$$

Dynamic boundary condition presents the pressure applied on the free surface. The pressure acting on the free surface of the water is just an atmospheric pressure. Therefore, dynamic boundary condition is defined as follows,

$$P|_{z=\eta} = 0 \qquad (A.13)$$

Continuity equation in form of shallow water equations can be derived by using equation A.1. It is derived by integrating equation A.1 with respect to vertical direction.

$$\int_{z_{bed}}^{\eta} \frac{du}{dx} dz + \int_{z_{bed}}^{\eta} \frac{dv}{dy} dz + \int_{z_{bed}}^{\eta} \frac{dw}{dz} dz = 0 \qquad (A.14)$$

Integration of first two equations in A.14 can be tackled with Leibnitz Integration Rule.

$$\int_{z_{bed}}^{\eta} \frac{du}{dx} dz = \frac{d}{dx} \int_{z_{bed}}^{\eta} \bar{u} dz - u_{\eta} \frac{d\eta}{dx} + u_{z_{bed}} \frac{dz_{bed}}{dx} \qquad (A.15)$$

$$\int_{z_{bed}}^{\eta} \frac{dv}{dy} dz = \frac{d}{dy} \int_{z_{bed}}^{\eta} \bar{v} dz - v_{\eta} \frac{d\eta}{dy} + v_{z_{bed}} \frac{dz_{bed}}{dy} \qquad (A.16)$$

$\bar{u}$ and $\bar{v}$ are the depth averaged velocity components of the water in x and y directions respectively. u_{η} and v_{η} are the velocity components of the free surface of the water in x and y directions respectively. $u_{z_{bed}}$ and $v_{z_{bed}}$ are the velocity components of the bottom surface of the water in x and y directions respectively. Last term in equation A.14 can be easily extracted from the integration.

$$\int_{z_{bed}}^{\eta} \frac{dw}{dz} dz = w_{\eta} - w_{z_{bed}} \qquad (A.17)$$

w_{η} and $w_{z_{bed}}$ are the vertical velocity components of the free and bottom surfaces of the water which are obtained with kinematic BC in equation A.11 and A.12. Equations A.11, A.12, A.15, A.16 and A.17 are inserted into equation A.14.

$$\frac{d}{dx}\int_{z_{bed}}^{\eta}\bar{u}dz - u_{\eta}\frac{d\eta}{dx} + u_{z_{bed}}\frac{dz_{bed}}{dx} + \frac{d}{dy}\int_{z_{bed}}^{\eta}\bar{v}dz - v_{\eta}\frac{d\eta}{dy}$$
$$+v_{z_{bed}}\frac{dz_{bed}}{dy} + \frac{d\eta}{dt} + u\frac{d\eta}{dx} + v\frac{d\eta}{dy} - \frac{dz_{bed}}{dt} + u\frac{dz_{bed}}{dx} + v\frac{dz_{bed}}{dy} = 0 \qquad (A.18)$$

Eventually, continuity equation can be simplified as follows;

$$\frac{dh}{dt} + \frac{d(h\,\bar{u})}{dx} + \frac{d(h\,\bar{v})}{dy} = 0 \qquad (A.19)$$

Continuity equation with non-movable bed is same with the continuity equation with movable bed. Therefore, it is concluded that although the granular flow changes the bottom surface of the water, the continuity equation of the water in the shallow water equations remains unchanged.

After the derivation of the continuity equation, momentum equation in z direction enables to obtain the hydrostatic balance relation. Integration of equation A.4 in vertical direction is tackled.

$$\int_{z}^{\eta}\frac{Dw}{Dt}dz = -\frac{1}{\rho}\int_{z}^{\eta}\frac{dP}{dz}dz + \frac{1}{\rho}\int_{z}^{\eta}\left(\frac{d\tau_{xz}}{dx} + \frac{d\tau_{yz}}{dy} + \frac{d\tau_{zz}}{dz}\right)dz + \int_{z}^{\eta} g\,dz \qquad (A.20)$$

$\frac{Dw}{Dt}$ is total vertical acceleration of the water. Main assumption of the shallow water equations indicates that the vertical acceleration of the water can be ignored. Additionally, τ_{xz}, τ_{yz}, τ_{zz} are negligible small stresses for the water.

$$0 = -\frac{1}{\rho}\int_{z}^{\eta}\frac{dP}{dz}dz - \int_{z}^{\eta} g\,dz \qquad (A.21)$$

$$0 = P_{\eta} - P + \rho g(\eta - z) \qquad (A.22)$$

P_{η} is already defined in equation A.13. Eventually, the hydrostatic balance relation can be written as;

$$P = \rho g(\eta - z) \qquad (A.23)$$

Shallow water form of the momentum equation in x direction is obtained from A.2.

$$\int_{z_{bed}}^{\eta} \left(\frac{du}{dt} + u\frac{du}{dx} + v\frac{du}{dy} + w\frac{du}{dz}\right) dz = -\frac{1}{\rho}\int_{z_{bed}}^{\eta} \frac{dP}{dx} dz$$

$$+\frac{1}{\rho}\int_{z_{bed}}^{\eta} \left(\frac{d\tau_{xx}}{dx} + \frac{d\tau_{yx}}{dy} + \frac{d\tau_{zx}}{dz}\right) dz + \int_{z_{bed}}^{\eta} a_x dz \qquad (A.24)$$

u is not the function of z direction, therefore, $\frac{du}{dz}$ is vanished. Left side of the equation A.24 is tackled with Leibnitz Integration Rule.

The left side of the momentum equation in x direction is;

$$\int_{z_{bed}}^{\eta} \left(\frac{du}{dt}\right) dz = \frac{d}{dt}\int_{z_{bed}}^{\eta} \bar{u} dz - u_\eta \frac{d\eta}{dt} + u_{z_{bed}} \frac{dz_{bed}}{dt} \qquad (A.25)$$

$$\int_{z_{bed}}^{\eta} \left(u\frac{du}{dx}\right) dz = \frac{d}{dx}\int_{z_{bed}}^{\eta} \bar{u}^2 dz - {u_\eta}^2 \frac{d\eta}{dx} + {u_{z_{bed}}}^2 \frac{dz_{bed}}{dx} \qquad (A.26)$$

$$\int_{z_{bed}}^{\eta} \left(v\frac{du}{dy}\right) dz = \frac{d}{dy}\int_{z_{bed}}^{\eta} \bar{u}\,\bar{v}\, dz - u_\eta v_\eta \frac{d\eta}{dy} + u_{z_{bed}} v_{z_{bed}} \frac{dz_{bed}}{dy} \qquad (A.27)$$

$u_\eta \frac{d\eta}{dt}$, $u_{z_{bed}} \frac{dz_{bed}}{dt}$, ${u_\eta}^2 \frac{d\eta}{dx}$, $u_\eta v_\eta \frac{d\eta}{dy}$, $u_{z_{bed}} v_{z_{bed}} \frac{dz_{bed}}{dx}$ and ${u_{z_{bed}}}^2 \frac{dz_{bed}}{dy}$ represent the advection terms of the equations. They are neglected in shallow water equations because convection terms are so dominant compared to the advection terms. Eventually, left side of equation A.24 can be written as follows;

$$\int_{z_{bed}}^{\eta} \left(\frac{du}{dt} + u\frac{du}{dx} + v\frac{du}{dy} + w\frac{du}{dz}\right) dz = \frac{d(h\bar{u})}{dt} + \frac{d(h\bar{u}^2)}{dx} + \frac{d(h\bar{u}\bar{v})}{dy} \qquad (A.28)$$

Viscous forces also can be derived with Leibnitz Integration Rule.

$$\int_{z_{bed}}^{\eta} \frac{d\tau_{xx}}{dx} dz = \frac{d}{dx} \int_{z_{bed}}^{\eta} \overline{\tau_{xx}}\ dz - \tau_{xx,\eta} \frac{d\eta}{dx} + \tau_{xx,z_{bed}} \frac{dz_{bed}}{dx} \qquad (A.29)$$

$$\int_{z_{bed}}^{\eta} \frac{d\tau_{yx}}{dy} dz = \frac{d}{dy} \int_{z_{bed}}^{\eta} \overline{\tau_{yx}}\ dz - \tau_{yx,\eta} \frac{d\eta}{dy} + \tau_{yx,z_{bed}} \frac{dz_{bed}}{dy} \qquad (A.30)$$

$$\int_{z_{bed}}^{\eta} \frac{d\tau_{zx}}{dz} dz = \tau_{zx,\eta} - \tau_{zx,z_{bed}} \qquad (A.31)$$

Finally, equations A.23, A.28, A.29, A.30 and A.31 are inserted into equation A.24.

$$\frac{d(h\bar{u})}{dt} + \frac{d(h\bar{u}^2)}{dx} + \frac{d(h\bar{u}\bar{v}\ )}{dy} = -gh\frac{dz_{bed}}{dx} - gh\frac{dh}{dx} + ha_x$$
$$+\frac{1}{\rho}\left(\frac{d(h\,\overline{\tau_{xx}})}{dx} + \frac{d\left(h\,\overline{\tau_{yx}}\right)}{dy}\right) + \frac{1}{\rho}\left(\tau_{x,\eta} + \tau_{x,z_{bed}}\right) \qquad (A.32)$$

$$\frac{d(h\bar{u})}{dt} + \frac{d\left(h\bar{u}^2 + \frac{1}{2}gh^2\right)}{dx} + \frac{d(h\bar{u}\bar{v}\ )}{dy} = -gh\frac{dz_{bed}}{dx} + ha_x$$
$$+\frac{1}{\rho}\left(\frac{d(h\,\overline{\tau_{xx}})}{dx} + \frac{d\left(h\,\overline{\tau_{yx}}\right)}{dy}\right) + \frac{1}{\rho}\left(\tau_{x,\eta} + \tau_{x,z_{bed}}\right) \qquad (A.33)$$

Where;

$$\tau_{x,\eta} = -\tau_{xx,\eta}\frac{d\eta}{dx} - \tau_{yx,\eta}\frac{d\eta}{dy} + \tau_{zx,\eta} \qquad (A.34)$$

$$\tau_{x,z_{bed}} = \tau_{xx,z_{bed}}\frac{dz_{bed}}{dx} + \tau_{yx,z_{bed}}\frac{dz_{bed}}{dy} - \tau_{zx,z_{bed}} \qquad (A.35)$$

Same process can be repeated to derive the momentum equation in y direction as defined in equation A.3. Therefore, shallow water form of the momentum equation in y direction is directly outlined.

$$\frac{d(h\bar{v})}{dt} + \frac{d(h\bar{u}\bar{v}\ )}{dx} + \frac{d\left(h\bar{v}^2 + \frac{1}{2}gh^2\right)}{dy} = -gh\frac{dz_{bed}}{dy} + ha_y$$
$$+\frac{1}{\rho}\left(\frac{d\left(h\,\overline{\tau_{xy}}\right)}{dx} + \frac{d\left(h\,\overline{\tau_{yy}}\right)}{dy}\right) + \frac{1}{\rho}\left(\tau_{y,\eta} + \tau_{y,z_{bed}}\right) \qquad (A.36)$$

Where;

$$\tau_{y,\eta} = -\tau_{xy,\eta}\frac{d\eta}{dx} - \tau_{yy,\eta}\frac{d\eta}{dy} + \tau_{zy,\eta} \qquad (A.37)$$

$$\tau_{y,z_{bed}} = \tau_{xy,z_{bed}}\frac{dz_{bed}}{dx} + \tau_{yy,z_{bed}}\frac{dz_{bed}}{dy} - \tau_{zy,z_{bed}} \qquad (A.38)$$

B. Derivation of Granular Flow Model

The granular flow is supposed as the grain-fluid mixtures. Motion of mixture of the granular flow can be demonstrated with Navier Stokes equations by adding separate effects of each solid and fluid constituents on the equations. Navier Stokes equations for the granular flow are written as follows:

$$\frac{du_g}{ds} + \frac{dv_g}{dk} + \frac{dw_g}{dn} = 0 \qquad (C.1)$$

$$\rho_g \left(\frac{Du_g}{Dt}\right) = -\frac{dP'}{ds} + \rho_g(g_s + a_s)$$
$$+\left(\frac{d\tau_{ss}^{solid}}{ds} + \frac{d\tau_{ks}^{solid}}{dk} + \frac{d\tau_{ks}^{fluid}}{dk} + \frac{d\tau_{ns}^{solid}}{dn} + \frac{d\tau_{ns}^{fluid}}{dn}\right) \qquad (C.2)$$

$$\rho_g \left(\frac{Dv_g}{Dt}\right) = -\frac{dP'}{dk} + \rho_g(g_k + a_k)$$
$$+\left(\frac{d\tau_{sk}^{solid}}{ds} + \frac{d\tau_{sk}^{fluid}}{ds} + \frac{d\tau_{kk}^{solid}}{dk} + \frac{d\tau_{nk}^{solid}}{dn} + \frac{d\tau_{nk}^{fluid}}{dn}\right) \qquad (C.3)$$

$$\rho_g \left(\frac{Dw_g}{Dt}\right) = -\frac{dP'}{dn} + \rho_g g_n$$
$$+\left(\frac{d\tau_{sn}^{solid}}{ds} + \frac{d\tau_{sn}^{fluid}}{ds} + \frac{d\tau_{kn}^{solid}}{dk} + \frac{d\tau_{kn}^{fluid}}{dk} + \frac{d\tau_{nn}^{solid}}{dn}\right) \qquad (C.4)$$

Where;

ρ_g is the density of the granular flow,

u_g , v_g and w_g are the velocity components of the granular flow in s, k and n directions respectively,

P' is the pressure of the fluid constituents within the granular flow,

g_s, g_k and g_n are the gravity acceleration components in s, k and n directions respectively.

a_s and a_k are the earthquake accelerations in s and k directions respectively.

Here, the density of the granular flow (ρ_g) is not defined as a function of time and space. In other words, density of the granular flow is constant. However, the density of the granular flow may not be constant in time and space due to the dilatancy effect. In detail, the dilatancy is the volume increment in the granular material when shear deformations of the granular materials are subjected. Hence, this volume difference may decrease the density of the granular materials. On the scope of this thesis, the density of the granular flow is not affected by dilatancy. But it should be kept in mind that there are some studies that consider the dilatancy effects on the landslide (George & Iverson, 2014). Moreover, although the effects of fluid and solid constituents of the granular flow on the motion of the landslide are considered separately, the granular flow, substantially, assumes as a mixture. Therefore, the density of the granular flow is computed as the average of these constituents with their densities and volume fractions of fluid and solid constituents.

$$\rho_g = \rho_s\gamma_s + \rho_f\gamma_f \qquad (C.5)$$

Where;

ρ_s is the density of the solid part of the granular flow,

γ_s is the volume fraction of the solid constituents of the granular flow,

ρ_f is the density of the water that is contained within the granular flow,

γ_f is the volume fraction of the fluid constituents that is contained within the granular flow.

Actually, in real phenomena, the granular flow contains also an air constituent. However, the air is neglected in the mathematical equations. Volume of the granular flow only consists of the solid and fluid constituents. Therefore, summation of the volume fraction of the solid and fluid constituents is equal 1.

$$\gamma_s + \gamma_f = 1 \qquad (C.6)$$

In equations C.1, C.2, C.3 and C.4, the granular flow uses the bed-oriented coordinates and the local coordinates (s, k and n) relate to where the bed position is. As a system at Figure 3.1, two local coordinates are valid either one with the inclined bed or one with the flat bed. Additionally, $\tau_{ij}^{constituent}$ indicates the stress of either the fluid constituent or solid constituent within the granular flow, that is applied on j.th plane towards i.th direction. All the stresses are illustrated in Figure C.1.

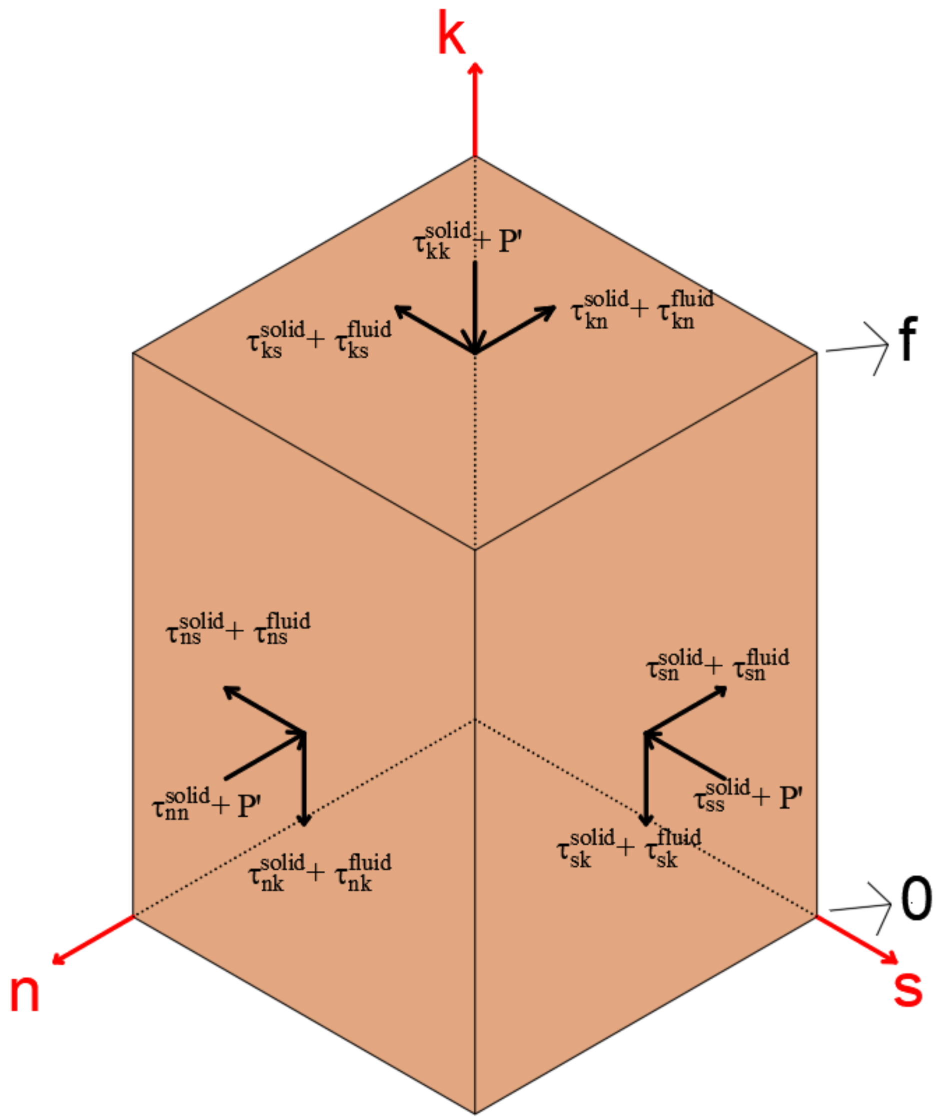

C. 1. Applied Stresses on a Single Mesh of The Granular Flow

The free and bottom surfaces of the granular flow are remarked as f and 0 respectively in Figure C.1. Only driven force in motion of the granular flow is the gravity force. Other stresses due to solid and fluid parts are acting opposite to the gravity force. Therefore, whole stresses except the gravity term are multiplied by negative sign.

$$\rho_g\left(\frac{Du_g}{Dt}\right) = -\frac{dP'}{ds} + \rho_g(g_s + a_s)$$
$$-\left(\frac{d\tau_{ss}^{solid}}{ds} + \frac{d\tau_{ks}^{solid}}{dk} + \frac{d\tau_{ks}^{fluid}}{dk} + \frac{d\tau_{ns}^{solid}}{dn} + \frac{d\tau_{ns}^{fluid}}{dn}\right) \qquad (C.7)$$

$$\rho_g\left(\frac{Dv_g}{Dt}\right) = -\frac{dP'}{dk} + \rho_g(g_k + a_k)$$
$$-\left(\frac{d\tau_{sk}^{solid}}{ds} + \frac{d\tau_{sk}^{fluid}}{ds} + \frac{d\tau_{kk}^{solid}}{dk} + \frac{d\tau_{nk}^{solid}}{dn} + \frac{d\tau_{nk}^{fluid}}{dn}\right) \qquad (C.8)$$

$$\rho_g\left(\frac{Dw_g}{Dt}\right) = -\frac{dP'}{dn} + \rho_g g_n$$
$$-\left(\frac{d\tau_{sn}^{solid}}{ds} + \frac{d\tau_{sn}^{fluid}}{ds} + \frac{d\tau_{kn}^{solid}}{dk} + \frac{d\tau_{kn}^{fluid}}{dk} + \frac{d\tau_{nn}^{solid}}{dn}\right) \qquad (C.9)$$

As defined in SWEs definition in Appendix A, equations C.7, C.8 and C.9 are required to define with the boundary conditions. Therefore, kinematic and dynamic boundary conditions are implemented to the Navier-Stokes Equations for the derivation of the SWEs of the granular flow.

For the kinematic boundary condition, the mathematical representation of free and bottom surfaces of the granular flow is introduced. So, the position of the free surface of the granular flow is

$$n = f(s,k,t) = b(s,k,t) + 0 \qquad (C.10)$$

b is the depth of granular flow and it is a function of space and time in local coordinates. 0 stands for the bottom of the granular flow. The reason to define the bottom as 0 is because using local coordinate disables the potential effects of the elevation of the bottom surface in earth-centered coordinates (x, y and z directions). Therefore, the bottom surface is taken as reference as always. Hence, position of the bottom surface can also be written as;

$$n = 0 \tag{C.11}$$

In the kinematic boundary conditions, by using the equations C.10 and C.11, the total derivation of free and bottom surfaces is 0 and can be written as follows.

$$\frac{D(n-f)}{Dt} = 0 \tag{C.12}$$

$$\frac{dn}{dt} + u_{g,f}\frac{dn}{ds} + v_{g,f}\frac{dn}{dk} + w_{g,f}\frac{dn}{dn} = \frac{df}{dt} + u_{g,f}\frac{df}{ds} + v_{g,f}\frac{df}{dk} + w_{g,f}\frac{df}{dn} \tag{C.13}$$

$$\frac{D(n)}{Dt} = 0 \tag{C.14}$$

$$\frac{dn}{dt} + u_{g,0}\frac{dn}{ds} + v_{g,0}\frac{dn}{dk} + w_{g,0}\frac{dn}{dn} = 0 \tag{C.15}$$

n is independent of t, s and k. Also, f is independent of n. Then, equations C.13 and C.15 are indicated as;

$$w_{g,f} = \frac{df}{dt} + u_{g,f}\frac{df}{ds} + v_{g,f}\frac{df}{dk} \tag{C.16}$$

$$w_{g,0} = 0 \tag{C.17}$$

In Dynamic BC, it can be proposed based on two situations of the landslide's initial position. One is by supposing that the free surface of the granular flow is exposed to atmosphere. The dynamic BC for this situation is;

$$P' = 0 \tag{C.18}$$

Another one is by supposing that the free surface of the granular flow is under the pressure of the water body. Due to water above the granular flow, the free surface is subjected to the hydrostatic pressure of the water. Therefore, the hydrostatic pressure due to water body requires to be applied on the granular material in dynamic boundary condition.

$$P' = \rho g h \qquad (C.19)$$

Where;

ρ is the density of the water,

h is the water depth.

In fact, for the numerical solver in this thesis, there is no place where only atmospheric pressure is applied on to the granular flow. Because in order to preserve stability, even dry bed for water and granular flow is defined with epsilon constant instead of 0 (Toro, 2001). That's why, there is numerically no subaerial granular flow. However, it is not considered because epsilon is relatively small. So, equation C.18 is valid due to very small epsilon.

The continuity equation for the granular flow model can be derived by using equation C.1. It is derived by integration of the equation C.1 with respect to the normal direction to the bed (n direction).

$$\int_0^f \frac{du_g}{ds} dn + \int_0^f \frac{dv_g}{dk} dn + \int_0^f \frac{dw_g}{dn} dn = 0 \qquad (C.20)$$

Integration of first two terms in C.20 can be tackled by Leibnitz Integration Rule.

$$\int_0^f \frac{du_g}{ds} dn = \frac{d}{ds}\int_0^f \overline{u_g}\, dn - u_{g,f}\frac{df}{ds} + u_{g,0}\frac{d0}{ds} \qquad (C.21)$$

$$\int_0^f \frac{dv_g}{dk} dn = \frac{d}{dk}\int_0^f \overline{v_g}\, dn - v_{g,f}\frac{df}{dk} + v_{g,0}\frac{d0}{dk} \qquad (C.22)$$

$\overline{u_g}$ and $\overline{v_g}$ are the depth averaged velocity components of the granular flow in s and k directions respectively. $u_{g,f}$ and $v_{g,f}$ are the velocity components of the free surface of the granular flow in s and k directions respectively. $u_{g,0}$ and $v_{g,0}$ are the velocity components of the bottom surface of the granular flow in s and k directions respectively. Last term can easily be simplified by solving the integration in equation C.20.

$$\int_{0}^{f} \frac{dw_g}{dn} dn = w_{g,f} - w_{g,0} \qquad (C.23)$$

$w_{g,f}$ and $w_{g,0}$ are the velocity components of the free and bottom surfaces of the granular flow in n direction. In fact, they are obtained by the kinematic BC in equations C.16 and C.17.

Then, the equations C.16, C.17, $C.21$, $C.22$ and $C.23$ are inserted into equation $C.20$.

$$\frac{d}{ds}\int_{0}^{f} \overline{u_g}\, dn - u_{g,f}\frac{df}{ds} + u_{g,0}\frac{d0}{ds} + \frac{d}{dk}\int_{0}^{f} \overline{v_g}\, dn - v_{g,f}\frac{df}{dk} + v_{g,0}\frac{d0}{dk} + \frac{df}{dt} + u_{g,f}\frac{df}{ds} + v_{g,f}\frac{df}{dk} = 0 \qquad (C.24)$$

Eventually, continuity equation can be simplified as follows;

$$\frac{db}{dt} + \frac{d\left(b\, \overline{u_g}\right)}{ds} + \frac{d\left(b\, \overline{v_g}\right)}{dk} = 0 \qquad (C.25)$$

After derivation of the continuity equation, the momentum equation in n direction can enable to obtain the balance relation of the stresses which are applied in n direction. Detailly, the integration of the equation C.9 in normal direction with respect to the bed is tackled.

$$\int_n^f \frac{Dw_g}{Dt} dn = -\frac{1}{\rho_g}\int_n^f \frac{dP'}{dn} dn$$

$$-\frac{1}{\rho_g}\int_n^f \left(\frac{d\tau_{sn}^{solid}}{ds} + \frac{d\tau_{sn}^{fluid}}{ds} + \frac{d\tau_{kn}^{solid}}{dk} + \frac{d\tau_{kn}^{fluid}}{dk} + \frac{d\tau_{nn}^{solid}}{dn}\right) dn + \int_n^f g_n \, dn \quad (C.26)$$

Main assumption of the granular flow model indicates that the bed-normal acceleration of the granular flow model can be ignored. Furthermore, τ_{sn}^{solid}, τ_{sn}^{fluid}, τ_{kn}^{solid} and τ_{kn}^{fluid} are the negligibly small stresses, so they can be neglected.

$$0 = -\frac{1}{\rho_g}\int_n^f \frac{dP'}{dn} dn - \frac{1}{\rho_g}\int_n^f \left(\frac{d\tau_{nn}^{solid}}{dn}\right) dn - \int_n^f g_n \, dn \qquad (C.27)$$

$$0 = P_f' - P' + \tau_{nn,f}^{solid} - \tau_{nn}^{solid} + \rho_g g_n (f - n) \qquad (C.28)$$

There are no effects of solid normal stress on the free surface. Therefore, $\tau_{nn,f}^{solid}$ is neglected. Moreover, the two possible situations of the pressure of the fluid within the granular flow are defined by dynamic boundary condition in the equations C.18 and C.19. Hence, the balance relation of the stresses applied in n direction can be written for the case in which the free surface of the granular flow is exposed to atmosphere as follows,

$$P' + \tau_{nn}^{solid} = \rho_g g_n (f - n) \qquad (C.29)$$

The balance relation of the stresses which are applied in n direction can also be written for the case in which the free surface of the granular flow is exposed to water body,

$$P' + \tau_{nn}^{solid} = \rho g h + \rho_g g_n (f - n) \qquad (C.30)$$

To use in the derivation of the momentum equation s and k directions, average form of the balance relation is formulated for both cases in equations C.29 and C.30.

$$\overline{P'} + \overline{\tau_{nn}^{solid}} = \frac{1}{b}\int_{0}^{f} \left(\rho_g g_n (f-n)\right) dn \tag{C.31}$$

$$\overline{P'} + \overline{\tau_{nn}^{solid}} = \frac{1}{2}\rho_g g_n b \tag{C.32}$$

Equation C.32 is the average form of equation C.29. It refers to the average form of the balance relation when the free surface of the granular flow is exposed to the atmosphere.

$$\overline{P'} + \overline{\tau_{nn}^{solid}} = \frac{1}{b}\int_{0}^{f} \left(\rho g h + \rho_g g_n (f-n)\right) dn \tag{C.33}$$

$$\overline{P'} + \overline{\tau_{nn}^{solid}} = \frac{1}{2}\rho_g g_n b + \rho g h \tag{C.34}$$

Equation C.34 is the average form of equation C.30. It indicates the free surface of the granular flow which is exposed to the water body.

The momentum equation in the s direction for the granular flow model can be simplified by the integration of the equation C.7 over the bed-normal elevations of the granular flow.

$$\rho_g \int_{0}^{f} \left(\frac{Du_g}{Dt}\right) dn = \int_{0}^{f} \left(\rho_g g_s\right) dn + \int_{0}^{f} \left(\rho_g a_s\right) dn - \int_{0}^{f} \frac{dP'}{ds}\, dn$$
$$- \int_{0}^{f} \left(\frac{d\tau_{ss}^{solid}}{ds} + \frac{d\tau_{ks}^{solid}}{dk} + \frac{d\tau_{ks}^{fluid}}{dk} + \frac{d\tau_{ns}^{solid}}{dn} + \frac{d\tau_{ns}^{fluid}}{dn}\right) dn \tag{C.35}$$

The stresses applied by each constituent can be aggregated into two distinct groups to simplify the problem. Also, by ignoring the advection terms of the granular flow, left side of the equation can be defined.

$$\left(\frac{d\left(b\overline{u_g}\right)}{dt} + \frac{d\left(b\overline{u_g}^2\right)}{ds} + \frac{d\left(b\overline{u_g v_g}\right)}{dk}\right) = (g_s + a_s)b + \frac{1}{\rho_g} T_{solid,s} + \frac{1}{\rho_g} T_{fluid,s} \tag{C.36}$$

Where;

$T_{solid,s}$ refers the stresses that are applied by the solid constituents in s directions,

$$T_{solid,s} = -\int_0^f \left(\frac{d\tau_{ss}^{solid}}{ds} + \frac{d\tau_{ks}^{solid}}{dk} + \frac{d\tau_{ns}^{solid}}{dn} \right) dn \qquad (C.37)$$

$T_{fluid,s}$ refers the stresses that are applied by the fluid constituents inside the granular flow in s directions.

$$T_{fluid,s} = -\int_0^f \left(\frac{dP'}{ds} + \frac{d\tau_{ks}^{fluid}}{dk} + \frac{d\tau_{ns}^{fluid}}{dn} \right) dn \qquad (C.38)$$

Same process is followed by the momentum equation in k direction for equation C.8.

$$\rho_g \int_0^f \left(\frac{Dv_g}{Dt} \right) dn = \int_0^f (\rho_g g_k)\, dn + \int_0^f (\rho_g a_k)\, dn - \int_0^f \frac{dP'}{dk}\, dn$$
$$- \int_0^f \left(\frac{d\tau_{sk}^{solid}}{ds} + \frac{d\tau_{sk}^{fluid}}{ds} + \frac{d\tau_{kk}^{solid}}{dk} + \frac{d\tau_{nk}^{solid}}{dn} + \frac{d\tau_{nk}^{fluid}}{dn} \right) dn \qquad (C.39)$$

The stresses applied by each constitute can be aggregated into two distinct groups to simplify the problem.

$$\left(\frac{d\left(b\overline{v_g}\right)}{dt} + \frac{d\left(b\overline{u_g v_g}\right)}{ds} + \frac{d\left(b\overline{v_g}^2\right)}{dk} \right) = (g_k + a_k)b + \frac{1}{\rho_g} T_{solid,k} + \frac{1}{\rho_g} T_{fluid,k} \qquad (C.40)$$

$T_{solid,k}$ refers to the stresses that are applied by the solid constituent in k direction.

$$T_{solid,k} = -\int_0^f \left(\frac{d\tau_{sk}^{solid}}{ds} + \frac{d\tau_{kk}^{solid}}{dk} + \frac{d\tau_{nk}^{solid}}{dn} \right) dn \qquad (C.41)$$

$T_{fluid,k}$ refers to the stresses that are applied by the fluid constituent within the granular flow in k direction.

$$T_{fluid,k} = -\int_0^f \left(\frac{d\tau_{sk}^{fluid}}{ds} + \frac{dP'}{dk} + \frac{d\tau_{nk}^{fluid}}{dn}\right) dn \qquad (C.42)$$

Equations C.37 and C.41 for the solid stresses in both s and k directions are solved by separating each term in the equations. Then, τ_{ns}^{solid} in C.37 and τ_{nk}^{solid} in C.41 are;

$$-\int_0^f \left(\frac{d\tau_{ns}^{solid}}{dn}\right) dn = -\left(\tau_{ns,f}^{solid} - \tau_{ns,0}^{solid}\right) \qquad (C.43)$$

$$-\int_0^f \left(\frac{d\tau_{nk}^{solid}}{dn}\right) dn = -\left(\tau_{nk,f}^{solid} - \tau_{nk,0}^{solid}\right) \qquad (C.44)$$

$\tau_{ns,f}^{solid}$ and $\tau_{nk,f}^{solid}$ are the shear stresses at the free surface of the granular flow in s and k directions respectively. $\tau_{ns,0}^{solid}$ and $\tau_{nk,0}^{solid}$ are the basal shear stresses in s and k directions respectively. The basal shear stresses are significant terms. With this purpose, several rheological models are proposed to define the basal shear stress. Voellmy, Herschel-Bulkley, Bingham etc. are some examples of these rheological models. Coulomb term is used for the basal shear stresses.

τ_{ks}^{solid} and τ_{sk}^{solid} in equations C. 37 and C.41 are solved by Leibnitz Integration Rule.

$$-\int_0^f \frac{d\tau_{ks}^{solid}}{dk} dn = -\left(\frac{d}{dk}\int_0^f \overline{\tau_{ks}^{solid}}\, dn - \tau_{ks,f}^{solid}\frac{df}{dk} + \tau_{ks,0}^{solid}\frac{d0}{dk}\right) \qquad (C.45)$$

$$-\int_0^f \frac{d\tau_{ks}^{solid}}{dk} dn = -\left(\frac{d}{dk}\left(b\,\overline{\tau_{ks}^{solid}}\right) - \tau_{ks,f}^{solid}\frac{df}{dk} + \tau_{ks,0}^{solid}\frac{d0}{dk}\right) \qquad (C.46)$$

$\frac{df}{ds}$ and $\frac{d0}{ds}$ are negligible small in equation C.46.

$$-\int_0^f \frac{d\tau_{sk}^{solid}}{ds} dn = -\left(\frac{d}{ds}\int_0^f \overline{\tau_{sk}^{solid}}\, dn - \tau_{sk,f}^{solid}\frac{df}{ds} + \tau_{sk,0}^{solid}\frac{d0}{ds}\right) \qquad (C.47)$$

$$-\int_0^f \frac{d\tau_{sk}^{solid}}{ds} dn = -\left(\frac{d}{ds}\left(b\,\overline{\tau_{sk}^{solid}}\right) - \tau_{sk,f}^{solid}\frac{df}{ds} + \tau_{sk,0}^{solid}\frac{d0}{ds}\right) \qquad (C.48)$$

$\frac{df}{ds}$ and $\frac{d0}{ds}$ are negligible small in equation C.48.

So far, the shear stresses in equations C.37 and C.41 are defined. Here, τ_{ss}^{solid} and τ_{kk}^{solid} are the bed-lateral stresses in s and k directions respectively. By Leibnitz Integration Rule, the integration of τ_{ss}^{solid} and τ_{kk}^{solid} is tackled.

$$-\int_0^f \frac{d\tau_{ss}^{solid}}{ds} dn = -\left(\frac{d}{ds}\int_0^f \overline{\tau_{ss}^{solid}}\, dn - \tau_{ss,f}^{solid}\frac{df}{ds} + \tau_{ss,0}^{solid}\frac{d0}{ds}\right) \qquad (C.49)$$

Where, $\tau_{ss,f}^{solid}$ and $\tau_{ss,0}^{solid}$ are the bed-lateral stresses in s direction of free and bottom surfaces respectively. $\frac{df}{ds}$ and $\frac{d0}{ds}$ are negligible small in equation C.49.

$$-\int_0^f \frac{d\tau_{ss}^{solid}}{ds} dn = -\frac{d\left(b\,\overline{\tau_{ss}^{solid}}\right)}{ds} \qquad (C.50)$$

Same process is applied to find τ_{kk}^{solid}.

$$-\int_0^f \frac{d\tau_{kk}^{solid}}{dk} dn = -\frac{d\left(b\,\overline{\tau_{kk}^{solid}}\right)}{dk} \qquad (C.51)$$

$\overline{\tau_{ss}^{solid}}$ and $\overline{\tau_{kk}^{solid}}$ are the averaged bed-lateral solid stresses in s and k directions respectively. Due to Coulomb materials, averaged bed-lateral solid stresses have proportional to the averaged bed-normal solid stresses. This proportion is same for the average bed-lateral solid stresses in s and k directions. This means that these stresses are symmetric.

$$\overline{\tau_{kk}^{solid}} = \overline{\tau_{ss}^{solid}} = k_{act/pass}\,\overline{\tau_{nn}^{solid}} \qquad (C.52)$$

$k_{act/pass}$ is the coefficient of the lateral earth pressure. Generally, they are widely used in geotechnical purposes such as stabilization of retaining walls. For these purposes, generally Rankine earth pressure is taken into consideration.

$$k_{act/pass} = 2\frac{1 \pm \sqrt{[1 - \cos^2\phi]}}{\cos^2\phi} - 1 \qquad (C.53)$$

Where, ϕ is the internal friction angle of soil. However, in case of the granular flow, equation C.53 requires to be modified. Because, the bottom surface has its own friction angle when the granular flow slips above the bed. Hence, the effects of the friction angle of the bottom surface are also essential for calculation of lateral coefficient.

$$k_{act/pass} = 2\frac{1 \pm \sqrt{[1 - \cos^2\phi\,(1 + \tan^2\phi_{bed})]}}{\cos^2\phi} - 1 \qquad (C.54)$$

Where, ϕ_{bed} is the friction angle of the bed of the granular flow. The plus-minus sign "$\pm$" can be determined by the motion state of the granular flow. Negative sign "-" indicates that the motion state of the granular flow is in the active state. If divergence in velocities difference $\left(\frac{du_g}{ds} + \frac{dv_g}{dk} > 0\right)$ is formed for the individual cell, the granular flow behaves locally in active state. On the contrary, positive sign "+" indicates that the motion state of the granular flow is in the passive state. Passive state of the granular flow occurs when the velocity difference is converged for individual mesh $\left(\frac{du_g}{ds} + \frac{dv_g}{dk} < 0\right)$.

If $\frac{du_g}{ds} + \frac{dv_g}{dk} > 0$ (velocity diverges),

$$k_{act/pass} = 2\frac{1 - \sqrt{[1 - \cos^2\phi\,(1 + \tan^2\phi_{bed})]}}{\cos^2\phi} - 1 \qquad (C.55)$$

If $\frac{du_g}{ds} + \frac{dv_g}{dk} < 0$ (velocity converges),

$$k_{act/pass} = 2\frac{1 + \sqrt{[1 - \cos^2\phi\,(1 + \tan^2\phi_{bed})]}}{\cos^2\phi} - 1 \qquad (C.56)$$

When the friction angle of the bed is equal or greater than the internal friction angle of the granular material, the coefficient of the lateral earth pressure can be written as follows;

$$k_{act/pass} = \frac{1 + \sin^2\phi}{1 - \sin^2\phi} \qquad (C.57)$$

After finding the coefficient of the lateral earth pressure, the averaged bed-normal solid stress is also required to derive the bed-lateral solid stresses based on the equation C.52. Therefore, equations C.32 and C.34 are used for both cases of the situation of the granular flow. When the free surface of the granular flow is exposed to the atmosphere, the averaged bed-normal solid stress is;

$$\overline{\tau_{nn}^{solid}} = \frac{1}{2}\rho_g g_n b - \bar{P}' \qquad (C.58)$$

When the free surface of the granular flow is exposed to the hydrostatic pressure due to the water, the averaged bed-normal solid stress is;

$$\overline{\tau_{nn}^{solid}} = \frac{1}{2}\rho_g g_n b + \rho g h - \bar{P}' \qquad (C.59)$$

Averaged fluid pressure inside the granular flow is also an important consideration. It can be considered as summation of the fully hydrostatic pressure of the fluid and the pressure at the free surface by supposing that the granular flow is fully fluid as assumed in the article (Savage & Hutter, 1989). However, due to possessing solid and fluid constituents in the granular flow, fully hydrostatic pressure may cause inadequate outcomes. Because the solid constituent may change the averaged fluid pressure inside the granular flow. Therefore, the fluidity term, ψ, is introduced to implement the effects of the solid constituent on the averaged fluid pressure inside the granular flow.

$$\overline{P'} = \frac{1}{b}\int_{0}^{f} P'\,dn = \frac{1}{2}P_0' + \rho g h \qquad (C.60)$$

Where, P_0' indicates the fluid pressure at the bed of the granular flow.

$$P_0' = \psi \rho_g g_n b \qquad (C.61)$$

Here, P_0' refers to the pore pressure measured at the bed of the granular flow. It depicts the fluidic behavior of the granular flow. For example, when the pore pressure is fully hydrostatic pressure like the water with the sediments and there are no effects of the solid constituents from the granular materials inside the granular flow, it means that the fluidity coefficient, ψ, is 1 and pore pressure becomes $\rho_g g_n b$. However, when there are not fluidic behavior of the granular flow and it only contains the solid part, ψ becomes 0 and it indicates that P_0' is zero. In real cases, when the failure surface is known, pore pressure can be measured and with that knowledge, ψ can be determined.

Equation C.60 is valid for the case where the free surface of the granular flow is exposed to the hydrostatic pressure of the water. Only distinction between these cases is the addition of the hydrostatic pressure of the water body above the landslide. Therefore, for the case where the free surface of the granular flow is exposed to the atmosphere, the hydrostatic pressure term is going to be vanished at the end of the derivation.

Eventually, equations C.61 and C.60 are inserted into equation C.59.

$$\overline{\tau_{nn}^{solid}} = \frac{1}{2}\rho_g g_n b(1-\psi) \qquad (C.62)$$

As it can be seen in equation C.62, averaged bed-normal solid stress does not depend on what the free surface of the granular flow is exposed, because the hydrostatic pressure term is vanished. Equation C.62 is inserted into equation C.52.

$$\overline{\tau_{kk}^{solid}} = \overline{\tau_{ss}^{solid}} = \frac{1}{2}k_{act/pass}\rho_g g_n b(1-\psi) \qquad (C.63)$$

Inserting equations C.50, C.63, C.46 and C.43 into C.37 give the integration of the solid stresses in s direction.

$$T_{solid,s} = -\frac{d\left(\frac{1}{2}k_{act/pass}\rho_g g_n b^2(1-\psi)\right)}{ds} - \frac{d}{dk}\left(b\,\overline{\tau_{ks}^{solid}}\right) - \left(\tau_{ns,f}^{solid} - \tau_{ns,0}^{solid}\right) \qquad (C.64)$$

Inserting equations C.51, C.62, C.48 and C.44 into C.41 give the integration of the solid stresses in k direction.

$$T_{solid,k} = -\frac{d}{ds}\left(b\,\overline{\tau_{sk}^{solid}}\right) - \frac{d\left(\frac{1}{2}k_{act/pass}\rho_g g_n b^2(1-\psi)\right)}{dk} - \left(\tau_{nk,f}^{solid} - \tau_{nk,0}^{solid}\right) \qquad (C.65)$$

After finding the solid stresses in both s and k directions, the fluid stresses in both s and k directions are going to be derived. Integration form of the fluid stresses are written in equations C.38 and C.42.

$$T_{fluid,s} = -\int_0^f \left(\frac{dP'}{ds} + \frac{d\tau_{ks}^{fluid}}{dk} + \frac{d\tau_{ns}^{fluid}}{dn}\right) dn$$

$$T_{fluid,k} = -\int_0^f \left(\frac{dP'}{dk} + \frac{d\tau_{sk}^{fluid}}{ds} + \frac{d\tau_{nk}^{fluid}}{dn}\right) dn$$

$\frac{d\tau_{ns}^{fluid}}{dn}$ and $\frac{d\tau_{nk}^{fluid}}{dn}$ terms can be succeeded by using viscous force formulation. However, it assumed that the effects of them can be neglected on landslide-generated waves. $\frac{d\tau_{ks}^{fluid}}{dk}$ and $\frac{d\tau_{sk}^{fluid}}{ds}$ are vanished because the shear stresses of the fluid constituents are negligibly small. $\frac{dP'}{ds}$ and $\frac{dP'}{dk}$ can be solved by Leibnitz Integration Rule.

$$T_{fluid,s} = -\left(\frac{d}{ds}\int_0^f \overline{P}'\,dn - P_f'\frac{df}{ds} + P_0'\frac{d0}{ds}\right) \qquad (C.66)$$

$$T_{fluid,k} = -\left(\frac{d}{dk}\int_0^f \overline{P}'\,dn - P_f'\frac{df}{dk} + P_0'\frac{d0}{dk}\right) \qquad (C.67)$$

Derivation is handled by assuming that the free surface of the granular flow is exposed to the water, as defined by the dynamic boundary condition in equation C.19. Eventually, the case where the free surface of the granular flow is exposed to atmosphere, can be succeeded by removing hydrostatic pressure source term from the equation. The averaged fluid pressure is already defined in equation C.60 and C.61.

$$T_{fluid,s} = -\left(\frac{d}{ds}\int_0^f \left(\frac{1}{2}\psi\rho_g g_n b + \rho g h\right) dn - \rho g h\frac{df}{ds} + P_0'\frac{d0}{ds}\right) \qquad (C.65)$$

$$T_{fluid,s} = -\left(\frac{d\left(\frac{1}{2}\psi\rho_g g_n b^2\right)}{ds} + \frac{d(\rho g h b)}{ds} - \rho g h\frac{df}{ds}\right) \qquad (C.66)$$

$$T_{fluid,s} = -\frac{d\left(\frac{1}{2}\psi\rho_g g_n b^2\right)}{ds} - \rho g b\frac{d(h)}{ds} \qquad (C.67)$$

When the free surface of the granular flow is exposed to atmosphere, $T_{fluid,s}$ becomes;

$$T_{fluid,s} = -\frac{d\left(\frac{1}{2}\psi\rho_g g_n b^2\right)}{ds} \qquad (C.68)$$

Same process can be derived for the fluid stresses in k direction.

$$T_{fluid,k} = -\frac{d\left(\frac{1}{2}\psi\rho_g g_n b^2\right)}{dk} - \rho g b\frac{d(h)}{dk} \qquad (C.69)$$

When the free surface of the granular flow is exposed to atmosphere, $T_{fluid,k}$ becomes;

$$T_{fluid,k} = -\frac{d\left(\frac{1}{2}\psi\rho_g g_n b^2\right)}{dk} \qquad (C.70)$$